VIBRATION PARAMETER ESTIMATION TECHNIQUE FOR ULTRASONIC MEASUREMENT SYSTEMS

Ph.D. THESIS

by

KSH MILAN SINGH

DEPARTMENT OF ELECTRICAL ENGINEERING
INDIAN INSTITUTE OF TECHNOLOGY ROORKEE
ROORKEE – 247 667 (INDIA)

MARCH, 2016

VIBRATION PARAMETER ESTIMATION TECHNIQUE FOR ULTRASONIC MEASUREMENT SYSTEMS

A THESIS

Submitted in partial fulfilment of the
requirements for the award of the degree

of

DOCTOR OF PHILOSOPHY

in

ELECTRICAL ENGINEERING

by

KSH MILAN SINGH

DEPARTMENT OF ELECTRICAL ENGINEERING
INDIAN INSTITUTE OF TECHNOLOGY ROORKEE
ROORKEE – 247 667 (INDIA)

MARCH, 2016

INDIAN INSTITUTE OF TECHNOLOGY ROORKEE
ROORKEE

CANDIDATE'S DECLARATION

I hereby certify that the work which is being presented in this thesis entitled **"VIBRATION PARAMETER ESTIMATION TECHNIQUE FOR ULTRASONIC MEASUREMENT SYSTEM"** in partial fulfilment of the requirements for the award of the degree of Doctor of Philosophy and submitted in the Department of Electrical Engineering of the Indian Institute of Technology Roorkee, Roorkee is an authentic record of my own work carried out during a period from January, 2013 to March, 2016, under the supervision of Dr. P Sumathi, Department of Electrical Engineering, Indian Institute of Technology Roorkee, Roorkee.

The matter presented in this thesis report has not been submitted by me for the award of any other degree of this institute or any other institutes.

(Ksh Milan Singh)

This is to certify that the above statement made by the candidate is true to the best of our knowledge.

Date: ____________

(P. Sumathi)
Supervisor

ABSTRACT

A moving window discrete Fourier transform based synchronization technique is proposed in this research work for a non-contact ultrasonic vibration measurement system. When an ultrasonic wave is transmitted towards an moving object, it experiences a Doppler shift at the receiving end depending on the vibrating frequency and distance of the moving object. Hence, the received ultrasonic signal is phase modulated. The Doppler shift contains all the information of moving object such as vibration amplitude, frequency, and phase.

Firstly, vibration signal estimation techniques employed in ultrasonic measurement systems are reviewed. The literature review is focused on the Doppler signal extraction methods including the theory and analysis pertaining to the background of ultrasonic vibration measurement techniques. The phase modulated ultrasonic received signal in the vibration measurement system involves constant phase shift due to ultrasonic path length, phase shift introduced by Doppler effect due to vibrating object, and the parametric phase shift caused by interaction of high frequency ultrasonic wave and low pressure developed by vibrating object. Among the three phase shifts, the Doppler phase shift contains the vibrating signal information and the extraction of Doppler signal helps in knowing the velocity of the vibrating object, amplitude and phase of the vibration. Various techniques of Doppler phase shift retrieval are categorized based on the modulation index estimation procedures from the received ultrasonic signal. An analysis is made based on the information retrieval methods for estimation of vibration signal parameters, range of the vibration amplitude, frequency, and the preferable carrier frequency for transmission. Further, the analysis also presents various types of ultrasonic vibration measurement applications. Apart from the Doppler effect, the theoretical background of parametric effect in vibration measurement has been analyzed.

Secondly, a synchronization technique is presented for extracting the Doppler signal for extracting the Doppler signal in ultrasonic vibration measurement system using moving-window discrete Fourier transform (MWDFT) as a filter. A pair of ultrasonic transducers is used in which one transducer emits the continuous ultrasonic wave of 40 kHz toward

the vibrating disc and another transducer receives the phase modulated ultrasonic signal. In this technique, the received ultrasonic signal is tracked for variation in carrier. The quadrature detection is performed with the help of MWDFT. The FM-to-AM conversion is done by tuned MWDFT filter. A simple multiplier followed by another MWDFT suppresses the carrier from the received signal and hence the Doppler signal is retrieved. The retrieved signal is further processed to extract the phase modulating signal by sampling period adjustment of the MWDFT. This signal contains the vibration amplitude and frequency information. These parameters had been obtained for an electrodynamic vibration system by implementing the synchronization technique in field programmable gate array (FPGA).

Thirdly, when the ultrasonic carrier deviation is large because of the vibration frequency, the received signal appears as AM-FM signal instead of phase or frequency modulated signal. However, the vibration information is present only in frequency modulating signal. To separate the AM signal from FM signal, the MWDFT-PLL is modified in such a way that the sampling pulse generator produces pulses suitable for MWDFT bin-1 and MWDFT bin-0 for the retrieval of frequency and amplitude modulation signals, respectively. Hence, this method presents how the frequency and amplitude variation of mono-component AM-FM could be retrieved simultaneously. The proposed technique involves the feed-forward and feedback demodulation techniques. In case of feed-forward demodulation, the FM signal is converted into AM using a filter and the feedback demodulation involves phase locking schemes. The proposed scheme is capable of extracting Instantaneous Frequency (IF) and Instantaneous Amplitude (IA) for the signals comprising of large variation in frequency and amplitude. The wide operating range of the PLL scheme facilitates in achieving the large variation in AM-FM signal demodulation. In addition, the MWDFT incorporated in the PLL would extract the message signals in presence of noise. The proposed scheme is implemented in FPGA to validate the performance of MWDFT-PLL in decomposition of the mono-component AM-FM signal.

Fourthly, to improve the performance of the proposed scheme for (i) wider range and (ii) good SNR of demodulated frequency, a closed-loop MWDFT based frequency locked-loop (FLL) is proposed. With this scheme, message signal is retrieved from sinusoidal frequency

modulated signals. A MWDFT acts as a tuned filter, when the sampling frequency is integral multiple of the center frequency. The spectra of MWDFT exhibits almost flat amplitude and phase responses when it is placed in a closed-loop with fixed sampling frequency. These flat characteristics for variation in input frequency is utilized for tracking frequency modulated carrier. The small leakage observed in terms of magnitude and phase errors of MWDFT is further corrected by adaptive sampling frequency control. The proposed MWDFT-FLL offers frequency demodulation/estimation under following conditions (i) biased input, (ii) large frequency deviation, (iii) frequency modulation (FM) of decaying sinusoid, and (iv) noise and harmonics.

Finally, the velocity measurement of moving object is carried out by applying the MWDFT-PLL and FLL algorithms. In PLL algorithm, a constant velocity of the moving object is measured in d.c. shift at the out signal. But for FLL algorithm, when a sinusoidal signal of carrier frequency 40 kHz is transmitted toward the moving object having constant velocity, the linear change in carrier phase shift is experienced because of Doppler effect in the reflected wave. The linear change in phase shift is reflected as step change in estimated frequency. Thus, the constant velocity of the moving object is measured in terms of step change in carrier frequency.

Acknowledgements

I would like to express my deep sense of gratitude and sincere thanks to my guide **Dr. P. Sumathi**, Associate Professor, Department of Electrical Engineering, Indian Institute of Technology Roorkee, for her valuable guidance and support. I am highly indebted to her for her encouragement and constructive criticism throughout the course of this project work. Inspite of her hectic schedule, she was always there for clarifying my doubts and reviewed my dissertation progress in a constructive manner. Without her help, this thesis would not have been possible. I learned a lot from my guide not only in the academic area but in other spheres of life also. I wholeheartedly acknowledge her full cooperation that I received from the very beginning of this work up to the completion of this thesis.

I would like to make a special note of thank to my Student Rerearch Committee (SRC) chairman Prof. Vinod Kumar, Department of Electrical Engineering, Indian Institute of Technology Roorkee, members of SRC Prof. R. S. Anand, Department of Electrical Engineering, Indian Institute of Technology Roorkee, Prof. Debashis Ghosh, Department of Electronics and Communication Engineering, Indian Institute of Technology Roorkee, and all faculty members of the Department of Electrical Engineering for their co-operation. I am highly obliged to express my sincere thanks to all technical staffs of the Department of Electrical Engineering, who have helped me in all possible ways during this thesis work.

I am also thankful to my lovely family members, especially my father, mother and brothers, who were distant to me but were always support by my side and accompany for me to work peacefully during my thesis work. I also express my abounding feelings of gratitude to all those who helped me in this course but have not been listed here.

Author wishes special thank to his lovely research scholar friends, who helped to lighten the burden, especially to Mr. Jitendra Kumar Singh, Mr. Arun Balodi and Mr. Om Hari Gupta.

At last thanks to the Almighty God who has given the author spiritual support and courage to carry out this work.

Ksh Milan Singh

Contents

List of Figures

List of Tables

Abbreviations

ADC	**A**nalog-to-**D**igital **C**onverter
ALUT	**A**daptive **L**ook-**U**p-**T**able
AM	**A**mplitude **M**odulation
CNR	**C**arrier-to-**N**oise **R**atio
CNTL	**C**ontrol
CPPM	**C**haotic **P**ulse **P**osition **M**odulation
ENF	**E**lectric **N**etwork **Frequency**
DAC	**D**igital-to-**A**nalog **C**onverter
DACM	**D**ifferential **A**nd **C**ross **M**ultiply
DFT	**D**iscrete **F**ourier **T**ransform
DSP	**D**igital **S**ignal **P**rocessing
EMD	**E**mperical **M**ode **D**ecomposition
FLL	**F**requency **L**ocked **L**oop
FG	**F**actor **G**raph
FM	**F**requency **M**odulation
FPGA	**F**ield **P**rogrammable **G**ate **A**rray
GI	**G**eneralized **I**ntegrator
HSMC	**H**igh **S**peed **M**ezzanine **C**onnector
IA	**I**nstantaneous **A**mplitude
IF	**I**nstantaneous **F**requency
JTAG	**J**oint **T**est **A**ction **G**roup
KZK	**K**hokhlov **Z**abolotskaya **K**uznetsov
LED	**L**ight **E**mitting **d**iode
LVDT	**L**inear **V**ariable **D**ifferential **T**ransfomer
MA	**M**oving **A**verager
MEV	**M**icron **E**lectrodynamic **v**ibration

MPA	**M**icron **P**ower **A**mplifier
MWDFT	**M**oving **W**indow **D**iscrete **F**ourier **T**ransform
NCO	**N**umerical **C**ontrol **O**scillator
OPAMP	**O**perational **A**mplifier
PI	**P**roportional and **I**ntegral
PLL	**P**hase **L**ocked **L**oop
PPG	**P**hotoplethysmograph
QEA	**Q**uasi **E**igenfunction **A**pproximation
RF	**R**adio **F**requency
Rx	**R**eceiver
SAW	**S**urface **A**coustic **W**ave
SDFT	**S**liding **D**iscrete **F**ourier **T**ransform
SMA	**S**ub**M**iniature
SNR	**S**ignal-to-**N**oise **R**atio
SPG	**S**ampling **P**ulse **G**enerator
Tx	**T**ransmitter
VHDL	**V**ery high speed integrated circuit **H**ardware **D**escriptive **L**anguage

Chapter 1

Introduction

1.1 Background

Vibration measurement is very important in the field of industrial, medical and scientific applications. The vibration measurement techniques can be classified into two categories, (i) contact measurement and (ii) non-contact measurement. Contact type measurements are carried out by connecting the sensors such as accelerometer, strain gauge, and probes on the object of vibration. Contact type measurements yield excellent results, but in some applications contact to the measuring device is not possible because of the speed and lightweight of measuring devices. Further, the strain gauge do not have long reliable life, and requires high gain amplifiers for processing the measured data, thus making them susceptible to noise amplification problems [1]. Furthermore, measuring surface may not be smooth for fixing the sensing devices. Some transducers, such as capacitive, LVDT, magnetic or inductive-type vibration sensors, can measure the vibration of an object with good resolution but have a limited measuring range less than several centimeters [2]. Magnetic vibration sensors based on electromagnetic principle convert the vibration parameters into the induced emf. These sensors are relatively complex and large in structure. An inductive vibration sensors are normally electronic proximity sensors and their sensitivity, linearity and range are restricted. Thus, they are not suitable for measurement of higher frequency range. Capacitive vibration sensors measure the vibration parameters using conductive elements or dielectric properties. These sensors offer high resolution, high precision, and short dynamic response time but their measuring range is small. They are also affected by parasitic capacitances, slight electrical medium and electromagnetic fields. The capacitive sensors were used for sensing human proximity to measure position and space occupant [3]. The pulse oximeter employs the red and infrared light emitting diodes (LEDs) to obtain photoplethysmographic (PPG) waveforms that relates to the fundamental frequency of heart rate [4], [5]. Thus, these measurement techniques require contact surface and range of measurement is limited.

To overcome these problems non-contact type sensors are preferred in vibration measurement. In non-contact type of measurement optical methods based on laser interferometric technique can be used for advanced applications including measurements of lightweight structures. These optical systems are capable of measuring very small vibration velocities and displacements with large measurable range. Optical vibrometry has high resolution, resistance to electromagnetic interference, high accuracy, high precision and fast response. However, higher velocities, rough surfaces, opaque gases and a dusty environment may cause problems. Moreover, optical techniques are very expensive [6] and unfamiliarity to the end user. The optical approaches such as fiber bragg grating sensors and plastic optical fibers were employed for fiber vibration sensor [7]. These optical methods are more sensitive to noise when vibrations are converted into variations of the light intensity. Thus, the overall drawbacks can be overcome by non-contact type of vibration measurements using acoustic method.

The acoustic sensors and measurement methods are based on the characteristic of sound waves in a medium. It has a variety of applications in the field of engineering, medical diagnosis, industrial applications, and communication technologies. The physical parameters such as amplitude, frequency, phase, velocity and distance of the moving object can be sensed by airborne ultrasonic transducers. Some of these transducers include Piezoelectric, Lead Zirconate Titantate (PZT), Polyvinylidene fluoride (PVDF) and capacitive types [8]. The ultrasonic transducer such as PVDF has low mechanical impedance but less intensity [9], capacitive ultrasonic transducer has better impedance matching but the performance is difficult to predict and control [10], piezoelectric transducers provide large displacement but highly nonlinear [11], [12]. However, piezoelectric transducers are mainly used for measuring the dynamic force and acceleration. It has high sensitivity, high signal-to-noise ratio, large measuring range, simple structure, more reliable, very high frequency response, non-contact and light weight. It has weak output signal and not suitable for measurement in static condition. PZT and electrostatic transducers at 40 kHz are commercially available [9]. The acoustic outputs of these transducers are higher as compare to PVDF transducer if the same area and applied voltage are considered. Block diagram representation of non-contact type vibration measurement is shown in Fig. 1.1. These transducers sense the physical behavior of the vibrating signal and

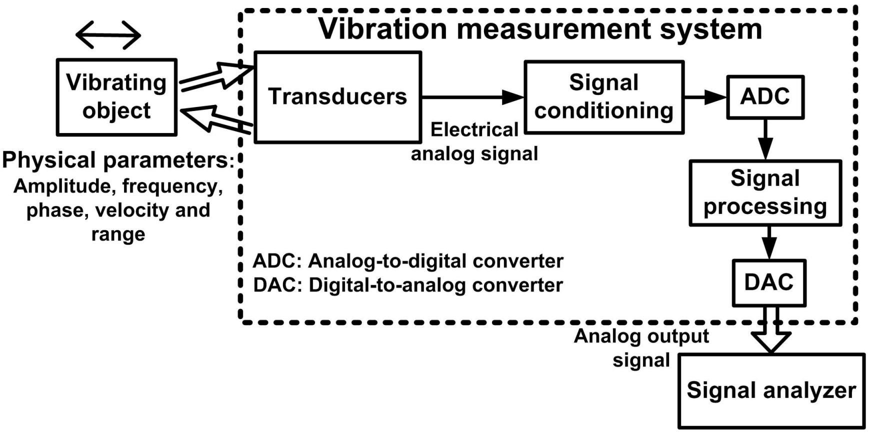

Fig. 1.1: Block diagram representation of non-contact type vibration measurement

convert them into analog electrical signal. This signal is applied to signal conditioning. Then, the analog signal is digitized through analog-to-digital (ADC) unit and applied for processing including amplification as well as filtering. Finally, the processed signal is passed through digital-to-analog (DAC) and the analog signal corresponds to the physical parameters are estimated in output signal analyzers or display units.

In vibration measurement systems, ultrasonic signal can be transmitted in pulse mode [13] or continuous mode [14]. In pulse mode, the transmitted pulse may not reflect properly at the receiver end, pulses can be missed, low resolution and attenuation of received pulse are the common problems. The measurement can employ single transducer or two transducers. A single piezoelectric ultrasound transducer is utilized as a transceiver in the application of range finding [15]. The time-of-flight is used for measuring the range. In single transducer measurement, calibration is required to resolve echoes during the ring down of the transducer. But, unlike capacitive transducers, no high-voltage bias is required. Further, the pulse mode is commonly employed in heart wall vibration [16]. The technique is more suitable for a single transducer pulse mode but it has lower dynamic range compare to continuous wave mode. For Doppler phase shift extraction, the technique [17] confirmed that it required a dual transducer. Some of ultrasonic vibration applications can be found from the literature review [18] that focuses on the industrial application and measurement methods such as cleaning, welding, cutting, food processing, water processing, sonochemistry etc. Surface acoustic wave (SAW) delay line is used to optimize SAW structures [19]. When sensing film is used to cover the delay line, the changes in the properties and dimensions of the sensing material alter the velocity, amplitude and phase of the SAW. It considerably reduced the computation complexity and memory usage of the machine. In another acoustic based application, pulse ultrasound is employed to measure the velocity component of single phase fluid flow [20], [21]. The technique is based on the variations in time of flight of two ultrasonic pulses transmitted simultaneously in perpendicular to the flow axis. The cross-correlation function had applied using the turbulence signals from two locations to obtain the flow velocity. In medical diagnosis application, a real-time 3-D ultrasound scanning had been used in an advance medical imaging [22]-[24]. In these techniques, the quadrature demodulation and decimation algorithms were applied to remove the high-frequency carrier term. Since the hardwired approach requires high computational complexity, the programmable technique had been employed for ultrasound colour-flow imaging [24]. Further, in the field of vibration measurement application, a piezoceramic disc had been used for vibration characterization of cymbal transducers in power ultrasonic application [25]. It had solved the drawbacks in the power limitation imposed by debonding of the epoxy layer. An ultrasonic technique had employed as a powerful rock drilling device using longitudinal-torsional compound vibration [26], [27]. For the application of multiple targets finding, an array processing algorithms (beamforming) were used to collect the acoustic data [28], [29] and the beamforming parameters were determined by various physical constraints such as target frequency range and speed. When the moving targets were closed to each other, a factor graph (FG) technique had been employed to track the targets [30]. Furthermore, a combined effect of acousto-optic and laser interferometry [31] were employed to reconstruct the 3D pressure field within the vessel and to evaluate the nonlinear distortion of propagating ultrasonic waves. These are some of the applications where acoustic methods have been applied successfully.

1.2 Motivation

When it comes to the field of vibration measurement applications, the acoustic method of vibration measurement provides cost effective solution with much less error [2]. It can employ in the rough and opaque surfaces, and it requires less circuitry for implementation. In non-contact type vibration or velocity measurement, Doppler effect is considered as one of the most common technique [32]. When the ultrasonic wave is transmitted towards an moving object, it experiences a Doppler shift at the receiving end depending on the vibrating frequency and distance of the moving object. Hence, the received ultrasonic signal is phase modulated. The Doppler shift contains all the information of moving object such as vibration amplitude, frequency, and phase. However, the extraction of Doppler shift from the received signal is a challenging research problem. Having the aforementioned advantages of acoustic techniques, many of the existing non-contact type vibration measurement techniques have certain drawbacks while estimating parameters from the received ultrasonic signal. From the literature review, the existing techniques of non-contact vibration measurement are classified into (i) Conventional method [2], [33]: Conventional estimator performs well even at high sampling frequency for discrete implementation. When received signal is not pure sinusoidal or truncated in nature, large bias is encountered in amplitude estimation. Further, performance depends on how well the time derivative or integration can be achieved. (ii) Phase operation method [33]- [36]: In this method, estimators are sensitive to sampling frequency. Thus, it requires fixed number of samples. Noise performance can be improved by averaging the estimated parameters but noise is amplified in the process of trigonometrical computation. Vibration frequency must be known first to estimate amplitude. (iii) Ratio method [37], [38]: This method is suitable for small vibration amplitude. It also requires intensive computation or large look-up tables of theoretical Bessel functions for comparison with measured data. Since all Doppler spectra suffer from poor SNR, signal is highly degraded. It cannot tolerate even slight nonlinearity. (iv) Correlation method [33], [39]: Correlation method removes the white noise added to quadrature signals. However, the noise is reduced by averaging over raw data. This method is applicable only for small vibration amplitudes. Longer the sequence is used in calculating the correlation functions, better is the estimation. Doppler phase shift based on correlation technique and frequency shift based on cross correlation were compared in a target velocity measurement [32]. However, both techniques were exhibited range ambiguity proportional to velocity. This is due to the strong coupling between velocity and range information in the received signals. (v) Standard deviation method [40]-[43]: Standard deviation method is performed in two ways; frequency domain and time domain. Frequency domain technique suffers in finding mean of the signal near Nyquist frequency with broad spectral spread in low signal-to-noise environment. The standard deviation methods are better estimators when vibration is large compared to interference with high SNR and enough samples. It possesses good linearity compare to ratio method. Time-domain processing is easier and low cost [43], thus superior to frequency domain processing. Frequency domain processing is slow, therefore these are slow estimators. Differentiation in the process of estimation increases the high frequency noise [41]. (vi) Kalman filter method [44]-[46]: Kalman method is stable and robust. It offers good estimation when vibration is very weak, noisy and distorted with the limited number of samples. The Kalman filter iteratively estimates the best amplitude and phase that matches the harmonic motion with a given frequency from noisy data based on the LMS criteria. (vii) Phase locking method [47], [48]: The received ultrasonic signal is frequency or phase modulated by the vibrating signal. Different types of phase locked loops (PLL) and digital phase locked loop techniques had been presented in [49], [50] with detailed discussion on various PLL components. PLL techniques perform well but easily affected by additive noise and difficult to remain locked to the desired input. (viii) Least squares method [51], [52]: In standard least-square method, normalized mean square difference is defined between the successive demodulated complex signals. The correlation term, which provides the corresponding minimum least-square value gives the vibration amplitude information [52]. Spatial resolution depends on sampling periods of the demodulated received signal. (ix) Zero-crossing method [53]-[55]: A discrete PLL is capable of counting the zero-crossing points [56]. In this method the modulation frequency variation should be much slower than carrier frequency variation. Frequency offset of the carrier and offset of the sampling frequency have an impact on demodulation [57]. Thus, these categorized non-contact vibration measurement techniques have certain limitation when estimating the Doppler signal and extracting the vibration parameters. Apart from the Doppler phase shift, parametric phase shift can be introduced in ultrasonic vibration measurement techniques. The parametric phase shift is resulted due to the interaction of two or more sound waves. The occurrence of this phase shift depends on the properties of sound waves and their interaction length [58], [59]. Parametric phase shift introduces as phase error in Doppler phase shift measurement from received ultrasound wave.

1.3 Objective

This research work aims to propose a vibration parameter estimation technique based on phase-locked loop [60], [61] with digital signal processing algorithm for the ultrasonic vibration measurement systems. The PLL scheme mainly composed of four components: Quadrature filter, phase detector, loop filter and sampling pulse generator (SPG). The quadrature filter/MWDFT is an IIR filter consisting of a comb filter followed by a complex resonator. The MWDFT is applied as a filtering process for extracting the quadrature components of the received ultrasonic signal. The MWDFT algorithm performs an N-point DFT on time samples where N is the number of samples in defined window. Initially, MWDFT computes the DFT of the N time samples then, the time window is moved one sample ahead. Next, new N-point DFT is computed. In this process, the current N-point DFT is efficiently computed from the results of the previous DFT. The moving of the time window for each output computation is what leads to the name moving DFT. Then, phase detector and loop filter are applied to remove the higher frequency components and noise contained in the received signal. Finally, to avoid the phase and magnitude errors, the sampling frequency is adaptively adjusted using feedback loop through the SPG unit.

In this context, a synchronization technique is proposed to retrieve the vibration parameters of a moving object when the received ultrasonic signal contains (i) noise, not purely sinusoidal and (ii) large carrier deviation because of path length, Doppler effect, and parametric effects. Further, it should possess the following qualities: (i) insensitive to sampling frequency variation, (ii) able to measure large vibration amplitude and frequency, (iii) reduced computational complexity, (iv) faster estimation, and (v) ease of digital implementation.

To this end, the research work proposes a synchronization technique based on MWDFT to retrieve the Doppler signal from the received ultrasonic signal. Further, it is observed that amplitude modulation along with phase modulation is introduced for certain carrier deviation in the received signal. Therefore, the synchronization technique is modified for AM extraction so that vibration parameter estimation is not affected by amplitude modulation of received signal. To improve the performance further, a frequency-locked loop (FLL) based on MWDFT as a FM demodulator is proposed. Furthermore, the velocity of the moving object is estimated by the proposed FLL as step change in carrier frequency. The experimental investigation is carried out by implementing the MWDFT based PLL, modified MWDFT based PLL, and MWDFT based FLL in FPGA.

1.4 Thesis organization

In chapter 1, The introduction begins with the background of vibration measurement techniques in section 1.1. Then, the important of acoustic method in non-contact vibration measurement is highlighted in the following preamble section 1.2. Motivation behind the science of acoustic vibration measurement and its application with merits and demerits are described. Next, the main objective of the research work is presented and then, followed by thesis organization.

In chapter 2, a review of vibration signal estimation techniques employed in ultrasonic vibration measurement systems is presented. The literature review focuses on the various techniques of Doppler phase shift retrieval and they are categorized based on the modulation index estimation procedures from the received ultrasonic signal. Section 2.1 introduces with vibration measurement techniques based on Doppler phase shift. Section 2.2 discusses the theoretical background of Doppler ultrasound vibration measurement, Doppler signal extraction, different mathematical formulation of modulation index estimation methods along with advantages and disadvantages. Further, parametric phase shift computation is introduced in ultrasonic vibration measurement. Effects of scattering pressure field on parametric phase shift are also included. Section 2.3 presents an analysis of various vibration measurement methods. The analysis section also describes the major issues arise during ultrasonic vibration measurement, parameter comparison of various methods, and applications. Section 2.4 summarizes with some remarks.

In chapter 3, a synchronization technique is presented for extracting the Doppler signal in ultrasonic vibration measurement system using MWDFT as a filter in PLL algorithm. In section 3.1, vibration measurement methods based on Doppler effect and it's applications are introduced. Section 3.2 describes the proposed synchronization technique and its components along with mathematical analysis for estimation of vibration parameters. Further, it presents the velocity estimation using the proposed scheme. Simulation studies conducted on the proposed method are presented in section 3.3. Implementation aspects of the synchronization technique for testing the electrodynamic vibration system and experimental results are discussed in section 3.4. Conclusion with some remarks is presented in summary section 3.5.

In chapter 4, the MWDFT-PLL is modified in such a way that the SPG produces sampling pulses suitable for MWDFT bin-1 and MWDFT bin-0 for the retrieval of frequency and amplitude modulation signals, respectively. Motivation behind the AM-FM demodulation technique is introduced in section 4.1. Section 4.2 describes the MWDFT PLL for an AM-FM signal decomposition using adaptive sampling frequency control. Section 4.3 presents an analysis based on Bessel function for AM-FM signal extraction using the MWDFT-PLL. Section 4.4 discusses the simulation results comprise of tracking range of the MWDFT PLL, effects of dynamic change in carrier, AM, and FM on demodulated signals, test cases proving the efficacy of the PLL in faithful retrieval of AM and FM message signals. Section 4.5 provides the experimental investigations carried out on the proposed extended PLL scheme. Section 4.6 summarizes this chapter.

In chapter 5, a MWDFT-based FLL algorithm is proposed for retrieving the message signal from sinusoidal frequency modulated signals. The technique has improved the range and noise immunity compared to the MWDFT-PLL algorithm. Section 5.1 introduces some of the merits employing closed-loop MWDFT-FLL algorithm in frequency estimation. Section 5.2 describes the proposed closed-loop MWDFT-FLL for modulation signal retrieval. Section 5.3 discusses the simulation studies performed on closed-loop MWDFT-FLL. The experimental performance validation and comparison with existing techniques are presented in section 5.4. Section 5.5 presents the measurement of moving object velocity based on MWDFT-FLL filter algorithm. It also describes the theoretical background of Doppler velocity measurement using ultrasonic technique. Section 5.6 summarizes with some remarks.

In chapter 6, conclusion is drawn including scope and future work.

Chapter 2

Non-contact type of vibration measurement based on Doppler shift

2.1 Introduction

Doppler effect has been widely applied since Austrian physicist Christian Doppler proposed the Doppler effect based on the colors of stars. At first, a non-contact type of vibration measurement apparatus based on Doppler effect for measuring amplitude and velocity of a vibrating body had been invented by Howard C. Hardy [62]. Since then, the Doppler effect has been employed in advanced medical diagnosis such as blood flow measurements [42], [63]-[66], arterial-heart wall vibration measurements [47], [67], [68], tissue motion detection [38], [69], also in monitoring the particle size in fluids [70], production of volvo cars [71], slow moving structure [34], surface velocity in a liquid [72], and sonar imaging techniques for monitoring dolphin calf and water quality [73], [74]. The combined effect of phase shift of the returned RF pulse due to the instantaneous change of the object position and the Doppler-shift had been employed in vibration measurement [39], [68]. This method accurately measures small vibrations of ventricle wall. Further, the analysis based on parametric effects [58] and combined Doppler and the parametric effects had been proposed in [14], [59], and applied in vibration measurement [72], [75], [76]. The transmitted ultrasonic wave can be contemplated as two different waves as follows [59]: (i) ultrasonic beam is a plane wave [14] (ii) ultrasonic beam is parabolic [58] at the source and diffraction effect develops Gaussian expansion [77]. In the second case, scattering effect [78]-[83] caused by the interaction of high pressure due to ultrasonic beam and low pressure developed by vibrating object has been an issue in parametric phase shift measurement. The research works on secondary pressure field generation are available since M. J. Lighthill began his first theoretical analysis on sound waves interaction [84], [85]. The scattered pressure field involved in vibration measurement can be derived mostly from the following two generating equations: Westervelt equation [79] and KZK

(Khokhlov-Zabolotskaya-Kuznetsov) equation [86], [87]. The KZK equation with Gaussian beam expansion have been used to calculate the scattering filed in vibration measurement [88]. Apart from the Doppler phase shift technique, a theory of time-domain correlation techniques for tissue motion detection had been reviewed by A. Hein [89]. Time-domain techniques are generally more computationally demanding than Doppler. However, with the tremendous advances in computing power, time-domain methods have become a practical alternative to Doppler.

When ultrasonic sensor is employed for detecting the moving object, it transmits the ultrasonic signal in pulse mode or continuous mode. The ultrasonic sensors can transmit and receive the pulses with two sensors; one sensor for transmission and another for receiving the transmitted pulse. secondly, only one sensor can be used for transmission and reception, this is the well-known triangulation method. Thirdly, the pulses at the transmitter side can be sent on and off mode repeatedly. In these methods, the transmitted pulse undergoes phase shift according to the distance and vibration of the object. When the transmitted pulse could not be reflected properly, pulses can be missed, resolution and attenuation are the common problems. Furthermore, continuous ultrasonic wave transmission is also employed for distance and vibration measurements of an object. Similar to pulse echo method, the continuous wave method can either employ one transducer or two transducers. But this method offers good accuracy in detecting the object vibration. However it suffers from ranging limitation due to wavelength [2]. When the ultrasonic wave is transmitted towards a moving object, it experiences a Doppler shift at the receiving end depending on the vibrating frequency of the object, distant of the moving object. Hence, the received ultrasonic signal is phase modulated. The Doppler shift contains all the information of moving object such as vibration amplitude, frequency, and phase.

Two types of measurements are important for a moving object. Those are : (i) the distance detection of moving targets i.e. range finding and, (ii) the estimation of physical parameters such as amplitude, velocity, frequency and/or phase from original location. This literature review chapter focused on the classification of modulation index estimation methods in Doppler ultrasonic vibration measurement system. Since the received ultrasonic signal from the moving targets experience a Doppler phase shift which contains the modulation index information proportional to the vibration amplitude. Further, the Doppler phase shift also consists of vibration frequency and vibration phase. The chapter also focuses on the different approaches which had been applied over the years for various applications.

2.2 Phase shift computation in ultrasound vibration measurement

The principle of an ultrasonic vibration measurement system is illustrated in Fig. 2.1. A continuous ultrasonic wave transmitted by a transducer (TX) is expressed as

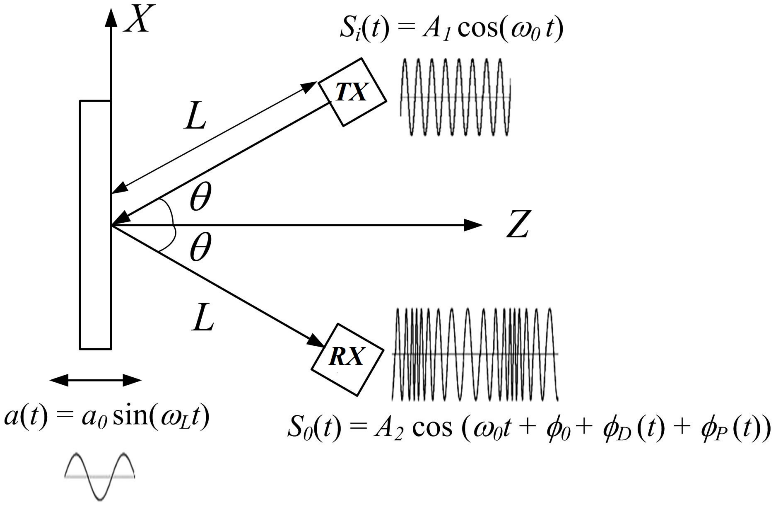

Fig. 2.1: An ultrasonic vibration measurement system

$$S_i(t) = A_1 \cos(\omega_0 t) \tag{2.1}$$

where A_1 is the amplitude of the transmitting wave and ω_0 is the frequency of the transmitting wave. $S_i(t)$ is transmitted by a transducer at certain angle θ towards a vibrating object, whose vibration is

$$a(t) = a_0 \sin(\omega_L t) \tag{2.2}$$

where a_0 is the amplitude of the vibrating signal and ω_L is the frequency of the vibrating signal. From Fig. 2.1, L is the path length from transmitter to the vibrating object or from vibrating object to the receiver (RX). The compression (C) and rarefaction (R) pressures developed on the right side of the test object due to the vibration are shown in the Fig. 2.2 [90]. The pressure fields cause the air particle to compress together in some regions and spread out in others. These particles produce high and low pressures that move away from the test object at the speed defined by velocity of the vibration object. The movement of high and low pressures is shown in Fig. 2.2 (a). Whenever the vibration object moves left, one new rarefaction is introduced in the pressure field and slightly moves the previous pressure fields towards left, which is shown in Fig. 2.2 (b). Similarly, the movement vibration object in the right direction causes the pressure field to move right, and one new compression is introduced, which could be observed from Fig. 2.2 (c) [90]. The ultrasonic receiver (RX) placed at a targeted distance receives the signal

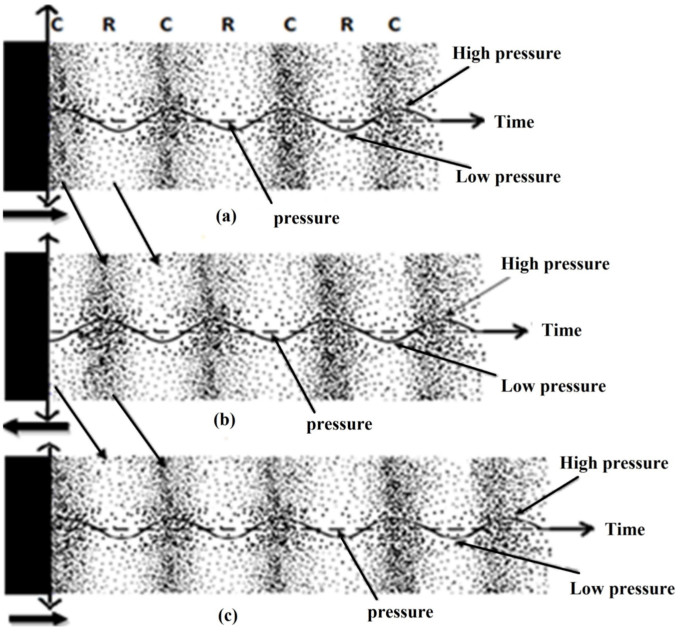

Fig. 2.2: (a) Development of compression and rarefaction pressure (b) Introduction of rarefaction when the vibration object is moving in left direction (c) Introduction of compression when the vibration object is moving in right direction [90]

$$S_0(t) = A_2 \cos\left(\omega_0 t + \phi_0 + \phi_D(t) + \phi_P(t)\right) \tag{2.3}$$

at certain angle θ; where A_2 is the amplitude of the received signal, ϕ_0 is the phase shift observed in the received ultrasonic beam due to path length, $\phi_D(t)$ is the phase shift introduced by Doppler effect, and $\phi_P(t)$ is the phase shift introduced by parametric effect. Therefore, the factors contributing phase shift in the ultrasonic received signal are:

(i) Total path length ($2L$) covered by the ultrasonic beam (ϕ_0)

(ii) Doppler effect ($\phi_D(t)$)

(iii) Parametric effect ($\phi_P(t)$).

2.2.1 Phase shift due to path length

The phase shift introduced in the received signal due to total path covered by the ultrasonic beam is

$$\phi_0 = k_0(2L) = \frac{\omega_0}{c_0}(2L) \tag{2.4}$$

where k_0 is wave number, ω_0 is angular frequency of ultrasonic beam and c_0 is the velocity of sound.

2.2.2 Phase shift due to Doppler effect

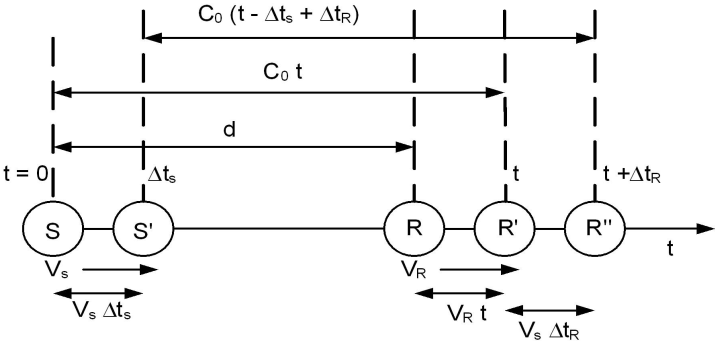

Fig. 2.3: Illustration of Doppler effect

Assuming the source (S) and receiver (R) are moving along the same line with the speed of V_s and V_r respectively, as shown in Fig. 2.3. At time $t = 0$, let the source S and receiver R be separated by a distance d. At time $t = 0$, S emits a wave that reaches R at time t later. In this time t the receiver will be moved a distance $V_R t$ and the wave, propagating with velocity c_0 would have travelled a distance $c_0 t$. The distance travelled by sound can be expressed as

$$c_0 t \quad = \quad d + v_R t \tag{2.5}$$

From (2.5)

$$t = \frac{d}{c_0 - V_R} \tag{2.6}$$

Now at time Δt_S, the source will be moved a distance $V_S \Delta t_S$. Let the wave emitted at that instant be received at time $t + \Delta t_R$ by R. In this time R would have traveled a total distance of $V_R(t + \Delta t_R)$, the total distance travelled by the sound is expressed as

$$c_0(t - \Delta t_S + \Delta t_R) = (d - V_S \Delta t_S) + V_R(t + \Delta t_R) \tag{2.7}$$

From (2.7), the receiver interval time between the waves is represented as

$$\Delta t_R = \frac{c_0 - V_S}{c_0 - V_R} \Delta t_S \tag{2.8}$$

The number of waves emitted in Δt_R by the source must be equal to the number of waves received by the receiver in Δt_S,

$$\begin{aligned} f_R \Delta t_R &= f_S \Delta t_S \\ f_R &= f_S \Delta t_S / \Delta t_R \\ &= \frac{1 - V_R/c_0}{1 - V_S/c_0} f_S \\ &= (1 - V_R/c_0)(1 - V_S/c_0)^{-1} f_S \end{aligned} \tag{2.9}$$

Where f_R is frequency received by the observer, f_S is the frequency of the source. Considering the speed of sound c_0 is much greater than the velocities of moving objects i.e. $c_0 \gg V_S$ and V_R, the binomial expansion yields

$$f_R \approx (1 - V_R/c_0)(1 + V_S/c_0) f_S = (1 - V_{RS}/c_0) f_S \tag{2.10}$$

Where $V_{RS} = V_R - V_S$ is the velocity of receiver relative to the velocity of emitter. Hence the Doppler frequency is represented as

$$\begin{aligned} f_D &= f_R - f_0 \\ &= -\frac{V_{RS} f_0}{c_0} \end{aligned} \tag{2.11}$$

Negative sign indicates the receiver moving away from the source that will be less than the frequency measured at the source, whereas the frequency measured by the receiver moving towards the source will be greater than the frequency measured at the source. From Fig. 2.1, the velocity of vibrating object normal to the surface towards right can be written as

$$V(t) = \frac{da(t)}{dt} = \omega_L a_0 \cos(\omega_L t) \tag{2.12}$$

The velocity component of vibrating object along the incoming and reflected beams would be $V \cos\theta$, where $V = \omega_L a_0 \cos(\omega_L t)$. Thus the velocity of receiver with respect to emitter is given as,

$$V_{RS} = 2V \cos\theta \tag{2.13}$$

From (2.11), (2.12) and (2.13), the Doppler frequency if derived as

$$f_D = f_R - f_0 = \frac{2V \cos\theta}{c_0} f_0 \tag{2.14}$$

where $f_R = (1 - (V_{RT}/c_0))f_0$ is the frequency observed by the receiver; f_0 is the emitter frequency. A few Doppler frequency estimators using pulse ultrasonic received signal are presented in [63]. The Doppler phase shift introduced in the received signal (2.3) can be written as

$$\begin{aligned} \phi_D(t) = \int_0^t 2\pi f_D dt &= \frac{2a_0(2\pi f_0)\cos\theta}{c_0} \sin(\omega_L t + \phi_L) \\ &= \beta \sin\left(\omega_L \left(t + \frac{L}{c_0}\right)\right) \end{aligned} \tag{2.15}$$

where $\beta = 2a_0\omega_0 \cos\theta/c_0$ is the phase modulation index introduced by the surface displacement of vibration object in the received signal $S_0(t)$; a_0 is the vibration amplitude which is part of β; $\omega_0 = 2\pi f_0$; wave number of carrier beam $k_0 = \omega_0/c_0$; phase of the vibration signal $\phi_L = \omega_L L/c_0$. The Doppler phase shift (2.15) introduced in the received signal (2.3) contains phase of the vibration signal ϕ_L. Hence, the Doppler phase shift (2.15) contains amplitude, frequency and phase of the vibration signal. While measuring the vibration parameters by Doppler effect, the returned signal is more complicated and the mathematical formulation of the Doppler shift are still subjects of controversy [91], [92]. The controversies can be listed as (i) Quasi-stationary approximation in Doppler effect, which means scattering field by a moving surface is to be considered as stationary field as if the surface was frozen at that time. (ii) Quasi-stationary method also does not display fundamental properties of velocity dependent reflection. (iii) A wave propagating in the same medium does not satisfy the same dispersion equation. (iv) Question of determining co-ordinate boundary conditions for non-uniformly moving object is yet unanswered. But for the simplified case of a sinusoidally vibrating target, the returned signal can be represented by a frequency modulation process.

2.2.3 Doppler signal extraction methods for β estimation

Generally, it is important to extract Doppler signal from the received ultrasonic signal in order to estimate the vibration signal parameters. From (2.3), by ignoring the parametric phase shift $\phi_P(t)$, the received ultrasonic signal can be expressed as

$$S_0(t) = A_2 \cos(\omega_0 t + \omega_D t + \phi_0) \tag{2.16}$$

where A_2 is the amplitude of received signal, $\omega_D t = \beta \sin(\omega_L t + \phi_L)$ is the Doppler phase shift, and ϕ_0 is constant phase shift due to path length. Correlating transmitted (2.1) and received (2.16) signals yield a signal:

$$\begin{aligned} S_{0c}(t) &= [A_2 \cos(\omega_0 t + \omega_D t + \phi_0)][A_1 \cos(\omega_0 t)] \\ &= \frac{A_1 A_2}{2} [\cos(\omega_D t + \phi_0) + \cos([2\omega_0 + \omega_D]t + \phi_0)] \end{aligned} \tag{2.17}$$

Low-pass filtering to remove carrier frequency $2f_0$, leaves the Doppler signal as

$$S_D(t) = \frac{A_1 A_2}{2} \cos(\omega_D t + \phi_0) \tag{2.18}$$

Directional information cannot be known from the extracted Doppler signal of (2.18). A number of discrimination techniques [93] can be applied to preserve the Doppler directional information; those are sideband filtering, offset carrier demodulation, and In-phase and Quadrature-phase demodulation. In the most commonly employed In-phase and

Quadrature-phase demodulation technique, the received signal (2.16) is correlated with in-phase reference $X_{ip}(t) = A_t \cos(\omega_0 t)$ and phase shifted reference $X_{ps}(t) = A_t \cos(\omega_0 t + \frac{\pi}{2})$. The resultant In-phase and Quadrature phase signals are

$$\begin{aligned}
i(t) &= S_0(t)X_{ip}(t) \\
&= \frac{A_2 A_t}{2}[\cos(\omega_D t + \phi_0) + \cos([2\omega_0 + \omega_D]t + \phi_0)] \\
q(t) &= S_0(t)X_{ps}(t) \\
&= \frac{A_2 A_t}{2}[\sin(\omega_D t + \phi_0) - \sin([2\omega_0 + \omega_D]t + \phi_0)] \qquad (2.19)
\end{aligned}$$

Both $i(t)$ and $q(t)$ are passed through the low-pass filter and amplified,

$$i_f(t) = \cos(\omega_D t + \phi_0); \quad q_f(t) = \sin(\omega_D t + \phi_0) \qquad (2.20)$$

The direction of flow is determined by noting the phase relationship between $i_f(t)$ and $q_f(t)$. If $\omega_D > 0$, then $q_f(t)$ is lagging $i_f(t)$ by 90°. If $\omega_D < 0$, then $q_f(t)$ is leading $i_f(t)$ by 90°. Different methods of Doppler signal extraction are employed in [94]-[96]. A normalized magnitude difference (NMD) method had been compared with quadrature method for a vibration amplitude measurement using (2.20) in [13]. Amplitude and phase information can be extracted from (2.20) by quadrature demodulation. Since the Doppler phase shift modulation index (β) is directly related to the vibration amplitude of the displacement field, estimating β is equivalent to estimating the vibration amplitude of the displacement and/or velocity fields. Different methods of estimation of β are described in the following section.

2.2.3.1 Conventional method

A simple method of estimation of β can be done using conventional Doppler estimators [33]. From the received ultrasonic signal (2.16), the vibrating signal can be extracted by quadrature demodulation. The in-phase and quadrature phase signals of received ultrasonic signal [46] are

$$\begin{aligned} S_{0i}(t) &= A_2 \cos(\omega_0 t + \phi_0 + \beta \text{sin}(\omega_L t + \phi_L)) \\ S_{0q}(t) &= -A_2 \sin(\omega_0 t + \phi_0 + \beta \text{sin}(\omega_L t + \phi_L)) \end{aligned} \tag{2.21}$$

By taking ratio of these two signals yields

$$S(t) = -\tan^{-1}\left(\frac{S_{0q}}{S_{0i}}\right) = \beta \sin\left(\omega_L t + \phi_L\right) + \phi_0 + \omega_0 t \tag{2.22}$$

The extracted vibrating signal is

$$y(t) = S(t) - \bar{S}(t) = \beta\ \sin(\omega_L t + \phi_L) \tag{2.23}$$

where $\bar{S}(t)$ is the mean of $S(t)$. Thus, β can be estimated using differentiating [97] or integrating (2.23).

$$\beta = \left[y^2(t) + \frac{1}{{\omega_L}^2}\left(\frac{dy(t)}{dt}\right)^2\right]^{\frac{1}{2}} \quad or \quad \beta = \left[y^2(t) + {\omega_L}^2\left(\int y(t)dt\right)^2\right]^{\frac{1}{2}} \tag{2.24}$$

Conventional estimators perform well even at high sampling frequency for discrete implementation. These estimators yield good result even if the carrier frequency and modulated frequency are related comparably like 0.1 $\omega_0 = \omega_L$. When received signal is not pure sinusoidal or truncated in nature, large bias is encountered in β estimation. Further, performance depends on how well the time derivative or integration can be achieved.

2.2.3.2 Phase operation method

From Fig. 2.1, the phase modulated signal at the receiver (2.3), ignoring $\phi_P(t)$ can be expressed as

$$S_0(t) = A_2 \cos(\omega_0 t + \phi_0 + \beta \sin(\omega_L t + \phi_L)) \tag{2.25}$$

In this method, phase operation is performed on the phase shift introduced by Doppler effect. The in-phase and quadrature signals [40] obtained from synchronous detection [33] to separate the Doppler signal are

$$\begin{aligned} I_k &= \cos(\beta \sin(k\omega_L T_s + \phi_L) + \phi_0) \\ Q_k &= \sin(\beta \sin(k\omega_L T_s + \phi_L) + \phi_0) \end{aligned} \tag{2.26}$$

where T_s is the sampling period and k is the sampling number. The wide-band discrete Hilbert transform [98] produces 90° phase shift of the local oscillator signal $S_{osc}(k)$. The received signal $S_0(k)$ and $S_{osc}(k)$ are correlated and passed through a low-pass filter to generate a signal I_k. Similarly, the $S_0(k)$ and 90° shifted $S_{osc}(k)$ are correlated and fed to the low-pass filter to obtain a signal Q_k. Using I_k and Q_k, the phase signal ϕ_k and co-phase signal ϕ'_k are generated by passing through the delays.

$$\begin{aligned} \phi_k &= \tan^{-1}\left(\frac{I_k Q_{k-1} - I_{k-1} Q_k}{I_k I_{k-1} + Q_k Q_{k-1}}\right) \\ \phi'_k &= \tan^{-1}\left(\frac{I_k Q_{k-1} + I_{k-1} Q_k}{I_k I_{k-1} - Q_k Q_{k-1}}\right) \end{aligned} \tag{2.27}$$

The modulation index β can be estimated using successive phase estimator, bi-phase estimator, and cross-phase estimator. From the phase signal ϕ_k and its successive samples, the difference and sum signals can be calculated as

$$\phi_k^- = \phi_k - \phi_{k-1}; \quad \phi_k^+ = \phi_k + \phi_{k-1} \tag{2.28}$$

Multiplying ϕ_k^- by $\cos(\omega_L T_s/2)$ and ϕ_k^+ by $\sin(\omega_L T_s/2)$, squaring and adding, the resultant equation becomes

$$[\phi_k^- \cos(\omega_L T_s/2)]^2 + [\phi_k^+ \sin(\omega_L T_s/2)]^2 = [4\beta^2 \sin^2(\omega_L T_s) \sin^2(\omega_L T_s/2)] \tag{2.29}$$

The modulation index β estimated from the successive phase estimator is

$$\beta = \left[\frac{[\phi_k^- \cos(\omega_L T_s/2)]^2 + [\phi_k^+ \sin(\omega_L T_s/2)]^2}{[4\sin^2(\omega_L T_s)^2 \sin^2(\omega_L T_s/2)^2]}\right]^{1/2} \tag{2.30}$$

Similarly from co-phase signal, the β can be estimated as

$$\beta = \left[\frac{[\phi_k'^{-} \cos(\omega_L T_s/2)]^2 + [\phi_k'^{+} \sin(\omega_L T_s/2)]^2}{[4 \sin^2(\omega_L T_s)^2 \cos^2(\omega_L T_s/2)^2]} \right]^{1/2} \tag{2.31}$$

A bi-phase and one shift cross-phase estimators can be formed by combining the phase and co-phase terms. In the bi-phase estimator

$$\beta = \left[\frac{[\phi_k / \sin(\omega_L T_s/2)]^2 + [\phi_k' / \cos(\omega_L T_s/2)]^2}{4} \right]^{1/2} \tag{2.32}$$

The noise suppressed β from the cross-phase estimator is

$$\beta = \left[\frac{\phi_k \phi_{k-1}' - \phi_{k-1} \phi_k'}{2 \sin^2(\omega_L T_s)} \right]^{1/2} \tag{2.33}$$

In phase operation of β estimation, ω_L is assumed to be known. For estimating the vibration frequency from phase and co-phase signals, the term ϕ_0 can be removed by filtering, and the phase ratio is

$$\frac{\phi_k - \phi_{k-1}}{\phi_k' + \phi_{k-1}'} = \tan^2(\omega_L T_s/2) \tag{2.34}$$

Thus, the vibration frequency is estimated as

$$f_L = \frac{1}{\pi T_s} \left[\tan^{-1} \left(\frac{\phi_k - \phi_{k-1}}{\phi_k' + \phi_{k-1}'} \right)^{1/2} \right] \tag{2.35}$$

The β estimation using successive phase estimator can be performed with the help of phase signal ϕ_k or the co-phase signal ϕ_k'. The carrier phase term ϕ_0 present in (2.26) is removed in the process of β estimation through successive phase estimation whereas the successive co-phase estimator could not remove the carrier phase term. The successive phase estimator offers wide operating range for β and vibration velocity. In addition, accurate estimation could be achieved when β is quite large. Bi-phase estimation, combining both phase and co-phase signals, needs one more arctangent operation compared to successive-phase estimator. But it is less sensitive to variation of sampling rate. Bi-phase estimator has also fairly performs well over wide range. In the process of β estimation through cross phase estimator, the uncorrelated noise is reduced by cross multiplications of in-phase and quadrature-phase signals. Cross-phase estimator is good for small vibration amplitude. Performance of all these estimators are independent of the phase of vibration ϕ_L.

All phase operation estimators are sensitive to sampling frequency variation and therefore the fixed number of samples are utilized. Averaging the estimated parameters can improve the noise performance. However, noise may be amplified while computing trigonometric function and hence the performance improvement is limited. In all phase operation estimators vibration frequency must be known before amplitude is estimated. As long as the vibration frequency estimation is maintained in a certain range of accuracy, the vibration amplitude can then be accurately estimated using one of the algorithms.

2.2.3.3 Ratio method

A Bessel function based estimation procedure is adopted in [38] for β estimation. Ultrasonic transmission is assumed as linear wave propagation and parametric effects are not taken into consideration. The received signal $S_0(t)$ is multiplied with the reference signals $r_1(t) = r_0 \cos(\omega_0 t)$, $r_2(t) = r_0 \sin(\omega_0 t)$ from the local oscillator. After eliminating the higher order harmonics by a low-pass filter, the resultant Doppler signals can be expressed in terms of Bessel function as,

$$\begin{aligned} d_1(t) = K\cos(\phi_0)&\left(J_0(\beta) + 2\sum_{n=1}^{\infty} J_{2n}(\beta)\cos(2n(\omega_L t + \phi_L))\right) \\ - K\sin(\phi_0)&\left(2\sum_{n=0}^{\infty} J_{2n+1}(\beta)\sin((2n+1)(\omega_L t + \phi_L))\right) \\ d_2(t) = K\sin(\phi_0)&\left(J_0(\beta) + 2\sum_{n=1}^{\infty} J_{2n}(\beta)\cos(2n(\omega_L t + \phi_L))\right) \\ - K\cos(\phi_0)&\left(2\sum_{n=0}^{\infty} J_{2n+1}(\beta)\sin((2n+1)(\omega_L t + \phi_L))\right) \end{aligned} \tag{2.36}$$

where, $K = A_2 r_0/2$, $J_n(x)$ is the n^{th} order Bessel function of first kind. In order to estimate the vibration amplitude, the spectrum of complex Doppler signal $d_1(t) + jd_2(t)$ is calculated. From the amplitude spectrum, $A_0 = K|J_0(\beta)|$ and $A_n = 2K|J_n(\beta)|$, n

= 1,2,3... and their consecutive ratios are $A_1/A_0 = 2|J_1(\beta)/J_0(\beta)|$ and $A_{n+1}/A_n = 2|J_{n+1}(\beta)/J_n(\beta)|$, $n = 1,2,3...$ are determined. From these ratios, the modulation index can be estimated [37]. Phase of the vibration signal is estimated from the fundamental components of the spectrum of either $d_1(t)$ or $d_2(t)$.

The ratio method is suitable when argument of Bessel function is small. Ratio method requires intensive computation or large look-up tables of theoretical Bessel functions for comparison with measured data. Since all Doppler spectra suffer from poor SNR, the signal is highly degraded. It cannot tolerate even slight nonlinearity. Since all Doppler spectra suffer from poor SNR, signal is highly degraded.

2.2.3.4 Correlation method

The received signal containing the small modulation indices are seriously affected by noisy environment. To remove the noise, an alternative method known as correlation method is proposed in [33]. This method performs well by averaging over the raw data. The Doppler complex quadrature signal is represented as

$$\begin{aligned} x(t) &= \cos(\beta\sin(\omega_L t + \phi_L) + \phi_0) + j\sin(\beta\sin(\omega_L t + \phi_L) + \phi_0) \\ &= e^{j\phi_0} e^{j\beta\sin(\omega_L t + \phi_L)} \\ &= e^{j\phi_0} \sum_{n=-\infty}^{\infty} J_n(\beta) e^{jn(\omega_L t + \phi_L)} \end{aligned} \tag{2.37}$$

To convert the time-domain procedure in frequency domain, the Fourier transform of $x(t)$ is determined, and represented in terms of n^{th} order Bessel function of first kind as

$$\begin{aligned} X(\omega) &= e^{j\phi_0} \sum_{n=-\infty}^{\infty} J_n(\beta) e^{jn\phi_L} \int_{-\infty}^{\infty} e^{-j(\omega - n\omega_L)t}\, dt \\ &= 2\pi e^{j\phi_0} \sum_{n=-\infty}^{\infty} J_n(\beta) e^{jn\phi_L} \delta(\omega - n\omega_L) \end{aligned} \tag{2.38}$$

Performing the autocorrelation function of $x(t)$ cancels the unknown phase ϕ_0 and the vibration phase ϕ_L. The autocorrelation of $x(t)$ is

$$\begin{aligned} R_{xx}(\tau) &= \frac{1}{T}\int_T x(t+\tau)x^*(t)dt = F^{-1}[X(\omega)X^*(\omega)] \\ &= \frac{1}{2\pi}\int_{-\pi}^{\pi}[e^{j\phi_0}\sum_{n=-\infty}^{\infty} J_n(\beta)e^{jn(\omega_L(t+\tau)+\phi_L)}e^{-j\phi_0}\sum_{n=-\infty}^{\infty} J_n(\beta)e^{jn(\omega_L t+\phi_L)}] \\ &= \sum_{n=-\infty}^{\infty} J_n^2(\beta)e^{jn\omega_L\tau} \end{aligned} \tag{2.39}$$

From the autocorrelation function, the power spectrum can be generated and expressed as

$$S(\omega) = F[R_{xx}(\tau)] = 2\pi\sum_{n=-\infty}^{\infty}J_n^2(\beta)\delta(\omega - n\omega_L) \tag{2.40}$$

Thus the resulting power spectrum is independent of both ϕ_0 and ϕ_L. Replacing the term $e^{j\omega_L\tau}$ by z^{-1} in (2.37), it can be expressed into a z-transform of a discrete sequence of Bessel function. The multiplication in the index domain of Bessel function for two discrete sequences is equivalent to the complex convolution in the z-domain.

$$R_{xx}(\tau)= \frac{1}{2\pi i}\int Z(\beta, z)Z\left(\beta, \frac{z}{v}\right)v^{-1}dv|_{z=e^{-\omega_L\tau}} \tag{2.41}$$

The z-transform of a discrete Bessel sequence produces its generating function,

$$Z(\beta, z) \equiv \sum_{n=-\infty}^{\infty} z^{-n}J_n(\beta) = e^{-(\frac{\beta}{2})(z-\frac{1}{z})} \tag{2.42}$$

Substituting (2.42) in (2.41) and setting $v = e^{j\theta}$ on the unit circle, results in

$$\begin{aligned} R_{xx}(\tau) &= \frac{1}{2\pi}\int_{-\pi}^{\pi}\left(e^{j\beta\ 2\cos(\theta+\frac{\omega_L\tau}{2})\sin(\frac{\omega_L\tau}{2})}\right)d\theta \\ &= J_0\left(2\beta\sin\left(\frac{\omega_L\tau}{2}\right)\right) \\ &\approx \left(1 - \frac{4\beta^2\sin^2(\frac{\omega_L\tau}{2})}{4}\right) \end{aligned} \tag{2.43}$$

From (2.43)

$$\beta \equiv \left(\frac{1-|R_{xx}(T_s)|}{\sin^2\left(\frac{\omega_L T_s}{2}\right)}\right)^{1/2} \tag{2.44}$$

The vibration frequency ω_L is assumed to be known in the β estimation process. Further, the quasi-autocorrelation function,

$$R'_{xx}(\tau)=\frac{1}{T}\int_T x(t+\tau)x(t)dt = e^{j2\phi_0}\sum_{n=-\infty}^{\infty} J_n^2(\beta)(-e^{j\omega_L\tau}) \tag{2.45}$$

$$|R'_{xx}(\tau)| \quad = \quad |e^{j2\phi_0}|J_0\left(2\beta\cos\left(\frac{\omega_L\tau}{2}\right)\right) \approx \left(1-\frac{4\beta^2\cos^2(\frac{\omega_L\tau}{2})}{4}\right) \tag{2.46}$$

From (2.46)

$$\beta \equiv \left(\frac{1-|R'_{xx}(T_s)|}{\cos^2\left(\frac{\omega_L T_s}{2}\right)}\right)^{1/2} \tag{2.47}$$

The ω_L can be removed by carefully combining autocorrelation and quasi-autocorrelation functions. From (2.43) and (2.46), modulation index is derived as

$$\beta \equiv (2-|R_{xx}(\tau)|-|R'_{xx}(\tau)|)^2 \tag{2.48}$$

This method is called as dual-autocorrelation estimator that cancels the unknown vibrating frequency ω_L.

Autocorrelation and cross-correlation methods remove the white noise added to quadrature signals. However, the noise is reduced by averaging over raw data. This method is applicable only for small vibration amplitudes. Longer the sequence is used in calculating the correlation functions, better is the estimation.

2.2.3.5 Standard deviation method

The estimation of β can be performed using the standard deviation method in both frequency-domain and time-domain as discussed in [42], [43], [99]. In frequency-domain processing, quadrature demodulation technique is applied and the received signal represents the complex quadrature signal as in (2.37). The probability density function is approximated as a function of power spectrum $S(\omega)$ given in (2.40) as

$$P(\omega) = \frac{S(\omega)}{\int_{-\infty}^{\infty} S(\omega) d\omega} \tag{2.49}$$

With this assumption, the mean Doppler frequency shift due to object movement can be expressed as

$$\bar{\omega} = \frac{\int_{-\infty}^{\infty} \omega S(\omega) d\omega}{\int_{-\infty}^{\infty} S(\omega) d\omega} \tag{2.50}$$

The variance corresponds to modulation index can be expressed as

$$\sigma_{\omega}^{2} = \frac{\int_{-\infty}^{\infty} (\omega - \bar{\omega})^{2} S(\omega) d\omega}{\int_{-\infty}^{\infty} S(\omega) d\omega} = \int_{-\infty}^{\infty} \omega^{2} P(\omega) d\omega - \bar{\omega}^{2} \tag{2.51}$$

Where σ_{ω} is the Doppler spectral spread (second moment m_2), $\bar{\omega}$ is the mean frequency shift of the Doppler spectrum (first moment m_1) and it is not necessarily zero since the Doppler signal is generally a complex signal. The power spectrum of the vibrating object is given in (2.40) $S(\omega)$, which does not need to be symmetric. This Bessel spectrum consists of baseband i.e. shifted to zero frequency by quadrature detection. So the mean frequency $\bar{\omega}$ becomes zero ($m_1 = 0$). From the symmetric down shifted spectrum about zero frequency is $J_{-n}(\beta) = (-1)^{2} J_{n}(\beta)$. Thus, spectral spread can be calculated from the moments of the spectrum.

$$m_0 = \sum_{n=-\infty}^{\infty} J_{n}^{2}(\beta) = 1; \qquad m_2 = \sum_{n=-\infty}^{\infty} (n\omega_L)^{2} J_{n}^{2}(\beta) = \omega_{L}^{2} \frac{\beta^{2}}{2} \tag{2.52}$$

From the spectral spread-moment relation [100], modulation index can be calculated. The variance

$$\sigma_{\omega}^{2} = \frac{m_2 - m_1^{2}}{m_0} = m_2 \tag{2.53}$$

Substituting (2.52) in (2.53), the modulation index

$$\beta = \sqrt{2}(\sigma_\omega/\omega_L) \tag{2.54}$$

Thus, the modulation index β can be estimated from standard deviation of the power spectrum. Frequency domain technique suffers in finding mean of the signal near Nyquist frequency with broad spectral spread in low signal-to-noise environment. To overcome this, time domain processing technique [35], [43], [101] can be applied to estimate the accurate spectral mean. The equivalent time domain integrals of mean frequency using Plancherels theorem:

$$\bar{\omega} = \frac{\frac{j}{2}\int_{-\infty}^{\infty}(x(t)\frac{dx^*}{dt} - x^*(t)\frac{dx}{dt})dt}{\int_{-\infty}^{\infty} x^*(t)x(t)dt} \tag{2.55}$$

Using (2.55), the mean frequency is written in terms of in-phase $I(t) = \cos(\beta\sin(\omega_L t + \phi_L) + \phi_0)$ and quadrature phase $Q(t) = \sin(\beta\sin(\omega_L t + \phi_L) + \phi_0)$

$$\bar{\omega} = \frac{\int_{-\infty}^{\infty}(I(t)\frac{dQ(t)}{dt} - Q(t)\frac{dI(t)}{dt})dt}{\int_{-\infty}^{\infty}(I^2(t) + Q^2(t))dt} \tag{2.56}$$

The complex representation of $x(t)$ in (2.37) can be represented as $x(t) = A(t)e^{j\theta(t)}$, where the instantaneous amplitude and phase are $A(t)$ and $\theta(t)$ respectively. Thus the instantaneous phase is represented as

$$\theta(t) = \tan^{-1}\left(\frac{Q(t)}{I(t)}\right) \tag{2.57}$$

From (2.57), instantaneous frequency [41] can be written as

$$\omega = \frac{d\theta(t)}{dt} = \frac{\left(I(t)\frac{dQ(t)}{dt} - Q(t)\frac{dI(t)}{dt}\right)dt}{P(t)} \tag{2.58}$$

where $P(t) = I^2(t) + Q^2(t)$ is the instantaneous power of the signal. Substituting (2.58) in (2.56),

$$\bar{\omega} = \frac{\int_{-\infty}^{\infty} P(t)\frac{d\theta(t)}{dt}dt}{\int_{-\infty}^{\infty} P(t)dt} = \frac{\int_{-\infty}^{\infty} P(t)\frac{d}{dt}\left(\tan^{-1}\frac{Q(t)}{I(t)}\right)dt}{\int_{-\infty}^{\infty} P(t)dt} \tag{2.59}$$

After the determination of mean frequency, β can be estimated similar to the frequency domain procedure as described in (2.50)-(2.54). Four different expressions for the mean frequency (2.59) are presented in terms of power spectrum density function, autocorrelation function, averaging function and signum function for time-stationary field [66]. In [42], the mean and standard deviations are expressed in terms of autocorrelation function. The algorithm [43] provides accurate values for instantaneous frequency and outperform the Fourier transform approach in poor signal-to-noise environments. The differentiate and cross multiply (DACM) [41] algorithm applies the computation of instantaneous frequency (2.58). The extended DACM algorithm [35] is free of nonlinear problems. It is capable of measuring time-varying vibration and complex movement patterns. This ensures that the original movement pattern can be directly measured. Traditional DACM algorithm is sensitive to noise due to need for differentiators in calculating mean, while the intentionally introduced accumulator in the extended DACM is able to suppress any kind of white noise with a zero mean.

The standard deviation methods are better estimators when vibration is large compared to interference with high SNR and enough samples. It possesses good linearity compare to ratio method. Time-domain processing is easier and low cost [43], thus superior to frequency domain processing. Frequency domain processing is slow, therefore these are slow estimators. Differentiation in (2.58) increases the high frequency noise [41].

2.2.3.6 Kalman filtering method

The vibrating signal can be extracted from the noisy received signal using Kalman filter approach [44]-[46]. The extracted vibrating signal (2.23) can be written with noise term $n(t)$ as a band limited system.

$$\begin{aligned} y(t) &= S(t) - \bar{S}(t) \\ &= \beta \sin\left(\omega_L t + \phi_L\right) + n(t) \\ &= \beta \sin(\omega_L t) \cos\phi_L + \beta \cos(\omega_L t) \sin\phi_L + n(t) \end{aligned} \tag{2.60}$$

Expressing (2.60) in matrices

$$\begin{aligned} y(k) &= [\sin(\omega_L k)\cos(\omega_L k)][\beta \cos\phi_L\ \beta \sin\phi]^T + n(k) \\ &= [h_1(k)\ h_2(k)][x_1(k)\ x_2(k)]^T + n(k) \end{aligned} \tag{2.61}$$

$y(k) = H_k x(k) + n(k)$, where $x_1(k)$ and $x_2(k)$ are state variables. Equation (2.60) can be written in terms of second order differential equation as

$$\frac{d^2y(t)}{dt^2} + \omega_L^2 y(t) = 0 \tag{2.62}$$

Equation (2.62) is transformed into second order state-space from

$$\begin{bmatrix} x_1(k+1) \\ x_2(k+1) \end{bmatrix} = \begin{bmatrix} 1 & 0 \\ 0 & 1 \end{bmatrix} \begin{bmatrix} x_1(k) \\ x_2(k) \end{bmatrix}; \quad x(k+1) = \Phi_k x(k) \tag{2.63}$$

The estimation $x(k)$ is given by minimizing the mean square error,

$$P_k = E[(x(k) - \hat{x}(k))\ (x(k) - \hat{x}(k))^T] \tag{2.64}$$

where $\hat{x}(k)$ is the estimation of $x(k)$. Kalman filter algorithm can be used to estimate the state variables. The amplitude (β) and phase (ϕ_L) can be found in terms of state variables as

$$\beta(k) = \sqrt{x_1^2(k) + x_2^2(k)}; \quad \phi_L(k) = \tan^{-1}\left(\frac{x_2(k)}{x_1(k)}\right) \tag{2.65}$$

Kalman filter continuously calculates optimal weights, the current state from the last estimated state and the current measurement by calculating a weighted mean of the two [41]. Kalman filter is being an effective tool to estimate a small tissue motion with a displacement of tens nanometers and a slow velocity in submillimeter per second with a known vibration frequency [45]. The Kalman filter iteratively estimates the best amplitude and phase that matches the harmonic motion with a given frequency from noisy data based on the LMS criteria. It is simple digital form, stable, robust, recursive, applicable in real-time [46].

The Kalman algorithm is stable and robust. This method offers good estimation when vibration is very weak, noisy and distorted with the limited number of samples [44]. Thus the method is good in noise cancellation compare to DACM algorithm. Kalman filter based approach is an effective tool for small displacements in presence of noise [45]. The Kalman filter provides error covariance which indicates reliability of measurements [46]. Kalman filter shows estimation errors in small displacements and small velocity in submillimeter per second [45].

2.2.3.7 Phase locking schemes

Phase locking scheme can be applied to extract the vibrating signal from the received ultrasonic signal. The received ultrasonic signal is frequency or phase modulated by the vibrating signal. Different types of phase locked loops and digital phase locked loop techniques had been presented in [49], [50] with detailed discussion on various PLL components. Arterial wall motion parameters are estimated using phase locking schemes in [47]. A sliding discrete Fourier transform (SDFT) based phase locking scheme [102] has been applied for frequency demodulation in [103]. From a vibration measurement system, the received ultrasonic signal $S_0(t) = A_2 \cos(\omega_0 t + \phi_0 + \beta \sin(\omega_L t + \phi_L))$ can be fed to the SDFT phase locking scheme. The numerically controlled oscillator (NCO) input (α) would extract the sinusoidal vibration signal. Hence, the vibration signal can be extracted from ultrasonic received signal using SDFT phase locking scheme. In a new phase-locking procedure, SDFT has introduced to split periodic signals into selected harmonic components, as on-line time functions [102]. To avoid the phase and magnitude errors, the sampling frequency adaptively adjusted using the phase-error itself i.e. phase error is nullified by the adaptive adjustment of the NCO frequency. This method also provides purer extracted harmonic signals as real-time functions with very little magnitude and phase errors in contrast to some conventional PLL procedures in which the presence of dc and other harmonics would require heavy filtering of input signal, causing phase lag. This method could also be fitted to FPGA devices as an on-line estimation of vibration analysis.

In this method, the Doppler signal can be extracted as an on-line estimation. Instantaneous Doppler signal can be retrieved from PLL. Digital implementation of PLL is easier compare to other algorithms. PLL techniques perform well but easily affected by additive noise and difficult to remain locked to the desired input.

2.2.3.8 Least squares method

In order to find the instantaneous object position, complex correlated successive received signal is demodulated. Then, based on the standard least-square method, normalized mean square difference $\alpha_n(\hat{\beta}_n; \delta_x)$ is defined between the successive demodulated complex signals $y(x + \delta_x; t + \Delta T)$ and $y(x; t)$, where $\hat{\beta}_n(\delta_x)$ is change in complex amplitude and δ_x is the movement of the object during the period of succeeding pulses ΔT. The correlation term, which provides the corresponding minimum least-square value is the modulation index [52]. The term $\alpha_n(\hat{\beta}_n; \delta_x)$ is minimized when

$$\hat{\beta}_n(\delta_x) = \frac{\sum\limits_{x \epsilon R} y^*(x; t) \cdot y(x + \delta_x; t + \Delta T)}{\sum\limits_{x \epsilon R} |y(x; t)|^2} \tag{2.66}$$

where R is the range around the object position $x(t)$ and $y^*(x; t)$ denotes the complex conjugate of $y(x; t)$. Spatial resolution depends on sampling periods of the demodulated received signal.

2.2.3.9 Zero-crossing method

The zero-crossing methods are preferred in frequency demodulation techniques. The product of two adjacent samples are computed, if the product is negative, it indicates a zero crossing has occurred [54]. A discrete PLL capable of counting the zero-crossing points is proposed in [56]. In a zero-crossing method [53], the instantaneous angular velocity of a shaft is defined as $\omega(t) = \omega_0 + \bar{\omega}(t)$, where ω_0 is a constant, $\bar{\omega}(t)$ is zero-mean angular velocity vibration and $|\bar{\omega}(t)| \ll \omega_0$. The term $\bar{\omega}(t)$ relates to the shaft angle vibration $\bar{\theta}(t)$ as

$$\bar{\theta}(t) = \int \bar{\omega}(t)dt \tag{2.67}$$

where $\bar{\omega}(t)$ is measured as

$$\bar{\omega}(t) = \omega(t) - \omega_0 \tag{2.68}$$

To estimate $\bar{\omega}(t)$, instantaneous angular velocity $\omega(t)$ is measured as an average value based on the zero-crossing technique [53] during time interval Δt

$$\omega(t_n) \approx \bar{\omega}(t_n) = \frac{2\pi}{N\Delta t_n} \tag{2.69}$$

where $\Delta t_n = t_{n-1} - t_n$ is the time btween two consecutive zeros and N is the number of identical cogs in the rotating shaft. Zero-order interpolations are employed to demodulate the frequency modulated carrier [55].

The advantage in this method is easy to find the zero crossing points. In this method the modulation frequency variation should be much slower than carrier frequency variation. Frequency offset of the carrier and offset of the sampling frequency have an impact on demodulation [57].

2.2.4 Phase shift computation due to parametric effect

The parametric phase shift is introduced by the ultrasonic beam propagation through low frequency pressure medium, which causes phase change. Considering plane waves for both ultrasonic beam and low pressure field from vibrating body, the variation of propagation velocity in the interaction zone depends on two factors as mentioned in [14], [72], [76]. One is propagation velocity due to excess pressure and second one is the velocity variation of a high frequency ultrasonic beam in the pressure field induced by a low frequency wave of the vibration.

2.2.4.1 Forward parametric phase shift

(i) The change in propagation velocity due to excess pressure is expressed as

$$\Delta c_1 = \frac{B}{2A}\frac{P_L(x_f,t)}{\rho_0 c_0} = \frac{\gamma-1}{2}\frac{P_L(x_f,t)}{\rho_0 c_0} \tag{2.70}$$

where, P_L is the pressure of the low frequency wave, A and B are the first and second order coefficients of Taylor series expansion for low pressure field respectively. The ratio is also related to γ as $B/A = \gamma - 1$, where $\gamma = c_P/c_V$ is the ratio of the specific heats at constant pressure and constant volume and ρ_0 is the equilibrium density of air.
(ii) Local propagation velocity (particle velocity) variation due to transport of the high frequency ultrasonic beam by the low frequency wave

$$\Delta c_2 \quad = \quad V_L(x_f,t)\cos\theta_1 \tag{2.71}$$

where V_L the particle velocity amplitude of the low frequency wave, and θ_1 is the angle between the propagation directions of the two waves. The total variation of the velocity along the high frequency beam is

$$\Delta c \quad = \quad \Delta c_1 + \Delta c_2 = (B/2A\rho_0 c_0)P_L(x_f,t) + V_L(x_f,t)\cos\theta_1 \tag{2.72}$$

From the Fig. 2.4, let t be the time taken when the high frequency beam reaches the

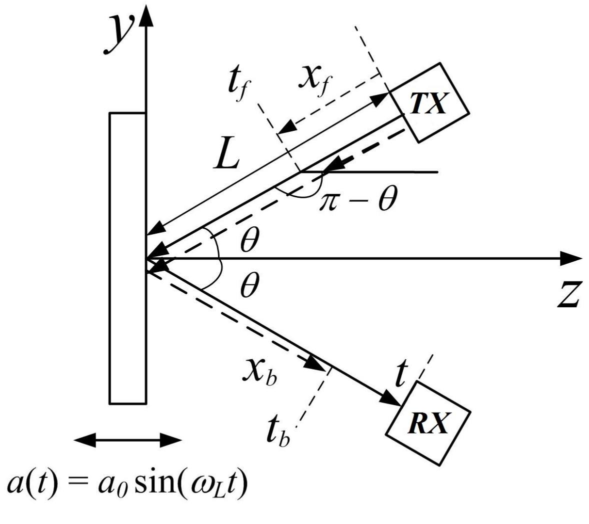

Fig. 2.4: Phase shift computation by forward and backward parametric effects

receiver and the interaction takes place at distance x_f from the emitter at time t_f . Since $\alpha_0 << L$ and $\Delta c << c_0$; the total time t can be expressed as,

$$t \cong \frac{2L}{c_0} = t_f + \frac{L - x_f}{c_0} + \frac{L}{c_0} \tag{2.73}$$

In this case, the ultrasound beam from emitter, and low pressure waves from vibrating object intersect at angle $\theta_1 = \pi - \theta$. The low frequency wave that interacts at the point with the ultrasonic beam has been emitted by the moving surface at time $t_f - (L - x_f)\cos\theta/c_0$. The forward parametric phase shift is

$$\begin{aligned} \phi_{PT} &= \int_0^L \frac{\omega_0 \Delta c}{c_0^2} dx_f \\ &= \frac{\omega_0}{c_0^2}\int_0^L \left((B/2A\rho_0 c_0)P_L(x_f,t) + V_L(x_f,t)\cos(\pi-\theta)\right) dx_f \end{aligned} \tag{2.74}$$

From the plane wave relation, $P_L = \rho_0 c_0 V_L$, replacing V_L in terms of P_L, and low frequency plane wave

$$P_L(x_f,t) = P_L \cos\left(\omega_L\left(t - \frac{L}{c_0} - \frac{L - x_f}{c_0}\right) - \frac{\omega_L}{c_0}(L - x_f)\cos\theta\right) \tag{2.75}$$

Equation (2.74) becomes

$$\phi_{PT} = \frac{\omega_0 P_L L}{2\rho_0 c_0^3}\left(\frac{B}{A} + 2\cos(\pi-\theta)\right)\cos\left(\omega_L\left(t - \frac{L}{2c_0}(3+\cos\theta)\right)\right) D(\theta_+) \tag{2.76}$$

where λ_L is the low pressure field wavelength developed due to vibrating surface. The parametric directivity is $D(\theta_+) = sinc\left(\frac{\pi L}{\lambda_L}(1+\cos\theta)\right)$.

2.2.4.2 Backward parametric phase shift

The low frequency wave emitted by the moving surface at the time $t_b - ((x_b - L)\cos\theta/c_0)$ interacts with the ultrasonic beam with an angle θ at point x_b as shown in Fig. 2.4. So, $\Delta c = (B/2A\rho_0 c_0)P_L(x_b,t) + V_L(x_b,t)\cos\theta$. Thus, the backward parametric phase shift is calculated by integrating from L to $2L$.

$$\phi_{PR} = \int_{L}^{2L} \frac{\omega_0 \Delta c}{c_0^2} dx_b = \frac{\omega_0}{c_0^2} \int_{L}^{2L} \left(\frac{(B/A) + 2\cos\theta}{2\rho_0 c_0} P_L(x_b, t) \right) dx_b \tag{2.77}$$

where,

$$P_L(x_b, t) = P_L \cos\left(\omega_L(t - \frac{2L - x_b}{c_0}) - K_L(x_b - L)\cos\theta \right) \tag{2.78}$$

$$\phi_{PR} \quad = \quad \frac{\omega_0 P_L L}{2\rho_0 c_0^3} \left(\frac{B}{A} + 2\cos\theta \right) \cos\left(\omega_L(t - \frac{L}{2c_0}(1 + \cos\theta)) \right) D(\theta_-) \tag{2.79}$$

where $D(\theta_-) = sinc\left(\frac{\pi L}{\lambda_L}(1 - \cos\theta)\right)$. Thus, the total phase shift offered by parametric effect in the received ultrasonic signal is

$$\phi_P = \phi_{PT} + \phi_{PR} \tag{2.80}$$

The parametric phase shift introduces phase error in Doppler phase shift measurement from received ultrasound wave. To compute the phase-shift undergone by the reflected wave, the moving boundary (Doppler effect) is separated from the effect of the moving medium (Parametric effect) [72]. Thus, the phase errors introduced by parametric effect are reduced at the output [76].

2.2.4.3 Scattering pressure field

The secondary pressure field is generated by the interaction of high frequency ultrasonic beam and low frequency exhibited from vibrating surface. This scattered pressure field can be included in determining parametric phase shift when wave deformation is considered for the analysis. The scattered pressure field involved in vibration measurement can be computed mostly from the Westervelt and KZK equations.

M. J. Lighthill [84], [85] introduced the sound wave interaction, which was experimented by Ingard and Brown for two perpendicular intersecting sound beams in air [78]. Then, Westervelt [79] proved that there is no scattering pressure exists as mentioned in [78].

Since then, Westervelt equation has been experimented by the researchers for the presence of scattered pressure field from two primary waves [80], [81], [83]. Diffraction of radiation of beams has been produced in all real sources of finite dimension and all the conducting media of the beams attenuate sound. The combined effect of diffraction, absorption and nonlinearity can be described by utilizing the KZK nonlinear parabolic wave equation [58], [59]. The diffraction of ultrasonic beam could be developed as Gaussian beam [58], [77]. A series of advantages using Gaussian beam function to define the beam field of an axis symmetric acoustical radiator could be found in [77] and applied in defining the scattering of sound by sound [104]. The combined effect of Doppler and parametric [14], [59] have been applied on vibration measurement applications [72], [75], [76].

2.3 Analysis

2.3.1 Issues

The ultrasonic vibration measurement system encounters certain issues related to time-domain and frequency domain processing. The issues arise during the phase shift computation of the Doppler and parametric effects are listed in this section.

Sound-beam shape: The effect of sound-beam shape are required to be determined for losses in the backscattered Doppler shifted signal from a blood vessel [105].

Sources of errors in Doppler vibration velocity measurement: The measurement error of vibration velocity of the object [106] is influenced by

(i) inaccuracy in the Doppler frequency measurement,

(ii) velocity variation of ultrasonic wave in air,

(iii) instability of the frequency of transmitter, and

(iv) accurate determination of the inclination angle of both transmitter and receiver during the measurement.

Effects of noise: The Doppler signal generally tends to be much lower than the carrier signal that results in poor signal-to-noise ratio. The error is introduced by the noisy environment in β estimation [99].

Sampling effect: Aliasing effect can be serious when the fold-over frequency or sampling frequency is not proper. Thus, to remove aliasing effects, the final sampling condition should satisfy $f_s = 2f_{fold} \geq \beta_{max} f_L$. High accuracy is predicted under proper sampling conditions even when the signal-to-noise ratio is poor [99].

Non-linear effect: If the received signal is not perfectly sinusoidal because of some medium or vibration source nonlinearities, Doppler spectrum shape will deviate from fundamental and second harmonic of the Bessel spectrum. Thus, the received signal can be written as

$$S_0(t) = A_2 \cos(\omega_0 t + \phi_0 + \beta \sin(\omega_L t + \phi_1) + \beta_2 \sin(2\omega_L t + \phi_2)) \tag{2.81}$$

The nonlinearity $N_2\,\% = \beta_2/\beta \times 100$, where β and β_2 are modulation indeces of fundamental and second harmonics of vibration respectively. At the worst case of 10 % nonlinearity, all the time-domain phase operation estimators introduce less than 1.2 % estimation error [33]. Slight deviations from single-frequency oscillation, would be caused by nonlinear or non ideal medium or source effects, and are found to have little contribution to the total estimation error [99].

Diffraction effect: Ultrasonic transmitting source is considered as plane wave to simplify the theoretical background. To determine the exact vibration amplitude of the surface, the parametric effect has been investigated and calculated under the plane wave assumption [14] in addition to the Doppler effect. However, the low-frequency acoustic wave emitted by a small vibrating body is not a plane wave. In fact, the plane wave assumption in is no longer valid [76]. Normally, due to the finite size of transducer, diffraction effect occurs at the source that could be the error in plane wave assumption. The ultrasonic beam propagation is not a plane wave due to the diffraction effect but it could be a Gaussian type expansion [58].

Parametric interaction: The phase shift of parametric effect is proportional to the low-frequency pressure and vibration speed. This phase shift need to be canceled from Doppler vibration measurement to obtain higher accuracy [72], [75], [76].

Quasi-stationary approximation: Doppler effect assumes the quasi-stationary approximation, which means scattering field by a moving surface is to be considered as stationary field as if the surface was frozen at that time [14]. However, it is inherently inconsistent, and therefore quasi-approximation might lead to erroneous results [91].

Effects of air speed in acoustic vibration measurement: As air speed increases, the acoustic sensor detects a progressively richer turbulent spectrum that reduces the sensitivity of the sensor [75]. In turn, optical sensors are prone to tremendous signal losses.

Relative position between RF echo and time window: In phase shift estimation between RF echoes of two consecutive frames, the RF echo is time shifted in comparison with that of the previous frame. However, the position of the time window for the Fourier transform is not changed between the two consecutive frames. This change in relative position between the RF echo and the time window has a strong influence on the estimation of the artery-wall displacement, resulting in error. To suppress this error, the phase shift should be estimated at the actual RF center frequency [107].

In-phase (I) and Quadrature (Q) component effects: Phase difference between I and Q component other than 90° and different amplitudes of I and Q lead to a periodically varying angular velocity even at constant object velocities [41].

Effects of large value of β: Doppler sidebands with mean frequency and its harmonics cannot be ignored if β value is large [94].

Systematic error in zero-crossing: In the measurement of angular velocity vibrations of rotating shafts, the zero-crossing method introduces a systematic error dependent on the frequency of the vibration harmonic [53].

Pull-in-range of PLL: Frequency demodulation as well as β estimation would be possible only if the carrier frequency variation is within the pull-in-range of the PLL.

Bandwidth Vs Resolution: One of the factors that directly affect the precision of both time-domain correlation and Doppler measurements is the bandwidth of the transmitted pulse. In the case of time-domain correlation, the higher the bandwidth, shorter pulse, the better the resolution. For Doppler systems, a high-bandwidth transmitted pulse will produce a broader Doppler spectrum, however the precision of Doppler measurements improves with a lower bandwidth. Thus, a compromise between resolution and precision must be made [89].

2.3.2 Comparison

The different techniques reviewed in section 2.2.3 are compared for various parameters and ranges for which the particular method is adopted. The parameters such as vibration amplitude, velocity, frequency, ultrasonic carrier frequency used for transmission are listed in Table 2.1. The methods did not fall into the category presented in section 2.2.3 are also reviewed and listed in Table 2.2. The performance comparison would provide the detailed analysis of different methods and their suitable applications. Choosing the ultrasonic carrier would yield certain range of vibration velocity, vibration amplitude, and vibration frequency.

From Table 2.1, it can be observed that Kalman method is applied to measure the tissue softness. The method provides excellent estimations for very small, submicron level, harmonic vibrations. It has potential for noninvasive and quantitative stiffness measurements of tissues such as artery. The difference of estimation results between Kalman filter method and laser vibrometer is less than 10 % [45]. Further, the ratio method is also preferred to know the mechanical properties of the soft tissue [38]. Furthermore, the standard deviation method is applied in cardiac activity monitoring, blood flow velocity detection, and tissue vibration. In blood flow detection under skull by Doppler Effect, center of gravity is calculated in mean frequency which is defined in terms of power spectrum density. The use of ultrasonic system has several advantages over magnetic resonance imaging (MRI) and X-ray computed tomography (CT) [108].

In PLL techniques, the spatial resolution of the tracking is limited by the clock frequency of the employed circuit up to several tens of megahertz with same upper limit of velocity estimation. Thus, PLL techniques cannot reach the spatial resolution obtained by the Least-square method [68]. Similarly, the spatial resolution in the estimation of object displacement is achieved in less than several micrometers using least square technique [68] compared to the correlation techniques [42]. The methods listed in Table 2.1 measure the vibration signal information using Doppler effect by neglecting the parametric effect except the PLL technique [76].

Table 2.2 lists the various procedures that utilize only the Doppler effect, Doppler and parametric effects. In these methods the vibration signal information is obtained through measuring the phase shift, time delay, Doppler frequency etc. In combined Doppler and parametric effects, few procedures try to cancel out the parametric effect by placing the microphone in between the transmitter and receiver at some distance [76]. If the parametric effect is considered for extracting the vibration signal then the measurement accuracy is increased. In surface velocity measurement of liquid [72], the vibration amplitude in the order of picometer could be estimated. Similarly, the liquid velocity of 0.1 mm/s could be measured.

2.3.3 Applications

Various applications of vibration measurement techniques are also listed in Table 2.1 and Table 2.2. The Tables provide the listed applications like measurement of mechanical structure vibrations and medical diagnosis. In the medical diagnosis, mainly, the ultrasonic vibration measurements include artery wall vibrations, ventricle wall vibration, cardiac activity monitoring, tissue vibration, bone vibration measurement in fracture healing monitoring, blood velocity measurement, artery shear wave velocity measurement, elasticity and viscosity of tissues, harmonic motion of tissue, and Bovine muscle motion. In mechanical structure vibration measurements include flexible beam vibrations, production line of car manufacturing, surface velocity of liquid, and angular vibration of rotating shafts.

2.4 Summary

The phase shift introduced by Doppler effect in the received ultrasonic signal can be computed by estimating the modulation index. Therefore, classification of various vibration signal parameter estimation procedures for Doppler ultrasonic measurement systems are reviewed. From this literature review, vibration parameters estimation techniques have been broadly classified into classical method, phase operation method, ratio method, correlation method, standard deviation method, Kalman filtering method, phase-locking method, least square method and zero crossing method. Further, the computation of phase shift due to forward and backward parametric effects are reviewed along with scattered pressure field generation. In this review chapter, various methods are analyzed for the frequency of ultrasonic carrier, vibration amplitude, frequency, velocity and their suitability for different applications with their merits and demerits.

Table 2.1: Comparison of different methods

S.No.	Techniques	Ultrasonic carrier	Vibration velocity	Vibration amplitude	Vibration frequency	Applications
1.	Conventional method [2]	40 kHz	336 m/s maximum	734.0032 mm maximum	$<$ 25 Hz	Mechanical structure vibrations
2.	Ratio method (Ultrasonic Doppler frequency) [38]	3 MHz	up to 1000 cm/s	100 μm	100 - 400 Hz	Viscoelastic / mechanical properties of soft tissues
3.	Ratio method [37]	NA	NA	NA	100 Hz	Wall vibrations in stenosed arteries
4.	Correlation method and Standard deviation method [42]	3 MHz	<130 cm/s	NA	NA	Blood flow imaging
5.	Correlation method [39]	3.5 MHz	NA	10 μm - 1 mm	5 Hz - 1.5 kHz	Ventricle wall vibration
6.	Standard deviation method and extended DACM [35]	20 GHz	NA	1 $\pm$ 0.1 mm	1 Hz	Mechanical vibrations and cardiac activity monitoring
7.	Standard deviation method [108]	1 MHz	50 -70 cm/s	NA	NA	Blood flow detection under skull
8.	Standard deviation method, NMD and quadrature method [13]	5 MHz	low in mm/s	$<$ 30 nm	200 Hz	Tissue vibration
9.	Kalman method [45]	5 MHz	7.88 - 12.5 m/s	NA	100 - 500 Hz	Shear wave velocity of an artery
10	Kalman method [46]	5 MHz	9.03 $\pm$0.51 m/s	$\pm$500 nm peak-peak	200 Hz	Elasticity and viscosity of tissue
11.	Kalman method (Pulse echo ultrasound) [44]	5 MHz	0.095 - 11.0 mm/s	30.2 nm - 3.50 μm	200 Hz	Harmonic motion of tissue
12.	Doppler shift and PLL technique [47]	8.866 MHz	NA	$<$ 0.28 mm	$<$ 5 kHz	Arterial-wall motion

S.No.	Techniques	Ultrasonic carrier	Vibration velocity	Vibration amplitude	Vibration frequency	Applications
13.	PLL and parametric effect [76]	200 kHz	NA	NA	1-3 kHz	Doppler velocimetry for vibrating body of 100 mm diameter
14.	Pulse Doppler ultrasound and PLL [105]	5 MHz	100 cm/s	NA	NA	Blood flow
15.	FM discriminator and integrator [106]	2 MHz	0.0002 m/s	0.001 mm	10 kHz	Mechanical structure vibrations
16.	Doppler shift with FM demodulator [71]	410 kHz	10 mm/s	NA	60 Hz	Production line at Volvo car corporation
17.	Phase detector and low-pass filter [34]	80 kHz	NA	0.2 m	< 50 Hz	Flexible beam vibrations
18.	Least-square method [52]	4 MHz	NA	< 100 μm	up to 1 kHz	Heart wall vibrations
19.	Constraint least-squared approach [51]	NA	$\pm$ 0.015 m/s peak-peak	< 300 μm	NA	Blood flow and arterial wall vibrations simultaneously
20.	Zero-crossing method [53]	40 MHz	shaft rotating at 2500 rpm	NA	Mechanical vibration of $0.010°$ at 10 Hz	Angular vibration of rotating shafts

Table 2.2: Comparison of miscellaneous methods

S.No.	Techniques	Ultrasonic carrier	Vibration velocity	Vibration amplitude	Vibration frequency	Applications
1.	Quadrature phase demodulation [109]	5 MHz	425 cm/s	2 μm	145 Hz (100-750 Hz)	Tissue vibration and blood velocities
2.	Quadrature method with Frequency-modulated [94]	2.16 MHz	20 - 80 cm/s	NA	$<$ 1 k Hz	Blood velocity measurements
3.	Time-domain echo tracking using Flip-Flop [67]	5 MHz	NA	0.78 mm peak-peak	$< 1\ kHz$	Arterial-wall motion
4.	Doppler shift and transition time [68]	3.5 MHz	0.000379 - 0.107 m/s	0.01 μm to 10 cm	0.01 Hz to 10 kHz	Heart wall vibration
5.	Doppler effect [110]	40 kHz	± 12 cm/s	-0.3 - 0 mm peak-peak	a few Hz - more than 2 kHz	Electro-mechanical vibrator
6.	Doppler and parametric [72]	30 MHz	down to 0.1 mm/s	down to 5 pm	NA	Surface velocity in a liquid
7.	Doppler and parametric [14]	420 kHz	NA	NA	100 Hz - 12 kHz	Parametric effect on vibration measurement
8.	Combined Doppler and parametric [75]	120 kHz	NA	200 nm	40 Hz	Vibrating surfaces covered with low-lying vegetation such as grass
9.	Ultrasonic vibrometry 2D FFT spectrum [69]	5 MHz	2 - 20 cm/s	5 μm	300 - 600 Hz	Tissue vibration and velocity
10.	Vibration-based technique called Vibrometry [111]	4 MHz	NA	NA	100 - 500 Hz	Bone vibration measurement, monitoring of fracture healing and diagnosis of osteoporosis
11.	Vibro-acoustic Doppler [112]	50 MHz	69.4 cm/s	NA	NA	Velocity of fluid
12.	Vibrating scattering medium [96]	9 MHz	NA	1000 nm	200 Hz	Bovine muscle motion

Chapter 3

Synchronization technique for Doppler signal extraction in ultrasonic vibration measurement systems

3.1 Introduction

Vibration measurement based on Doppler effect is considered as the most common technique because of its advantages such as non-contact measurement, reliability, and cost effectiveness. The ultrasonic vibration measurement can perform well in rough surfaces, opaque gases, dusty environment, and at higher velocities compared to optical methods. Moreover, when vibration amplitude increases the output of the optical sensor is distorted significantly [113], [114]. A RF polarimetry transducer uses electromagnetic wave polarization properties instead of Doppler shift and it has claimed to be ten-times cost effective compared to laser vibrometry [115]. The ultrasonic transducer is much cheaper and easy to handle. However, the sources of errors in Doppler vibration measurement is influenced by (i) inaccuracy in Doppler frequency measurement, (ii) velocity variation of ultrasonic wave in air, (iii) instability of the frequency of the transmitter, and (iv) inaccurate determination of the inclination angle of both transmitter and receiver during measurement. In vibration measurements, ultrasonic signal employed may be of pulse wave [13], continuous wave, and frequency modulated continuous wave [94]. When continuous wave ultrasound is employed, the received signal is phase or frequency modulated due to Doppler effect experienced by the vibrating object. The received signal contains the moving object parameters such as amplitude, velocity and frequency. Different methods of Doppler signal extraction are discussed in [13], [94], [96]. The Doppler signal with directional information is extracted using different types of discrimination methods [93] such as sideband filtering, offset carrier demodulation, and in-phase/quadrature-phase demodulation. The in-phase/quadrature-phase technique is employed in almost all vibration parameter estimation methods for Doppler signal extraction. Furthermore, the estimation of modulation index from the phase modulated received signal would help in determining the vibration parameters. The modulation index estimation procedures have been reviewed in chapter 2 and they are categorized along with merits and demerits. In brief, conventional method [33] cannot perform well when received signal is not pure sinusoid. All phase-operation estimators [33], [34] are sensitive to sampling frequency variation and therefore fixed number of samples are used for signal processing. The ratio method [37] requires intensive computation or large look-up tables. The correlation method [39] is applicable only for small vibration amplitudes. The estimators which employ standard deviation method [40], [41] are slow because frequency domain processing is involved. Kalman filter method [45] shows error for small displacements and velocity. In case of least-square method [51], spatial resolution depends on the sampling periods. The modulation frequency variation should be much slower than carrier frequency variation in zero-crossing method [53] for efficient demodulation. Though PLL techniques perform well, they are easily affected by additive noise. Moreover, a trade-off between resolution and speed of convergence is required [48].

Furthermore, apart from aforementioned modulation index estimation techniques, chaotic pulse position modulation (CPPM) with synchronization technique for distance measurement [116], [117] is proposed for eliminating the cross-talk problem and multipath fading. However, the chaotic system performance depends on the initial conditions. The small angle-approximation approach has a problem when the vibration amplitudes are comparable to the carrier wavelength [35] and it causes strong nonlinear harmonics and inter-modulation products in the reflected signal. Though the arctangent demodulation approach overcomes the harmonic problem, the differentiate and cross-multiply (DACM) phase demodulation algorithm outperforms the arctangent demodulation approach in the presence of noise [36]. Therefore, the existing techniques fail when

- the received signal is not purely sinusoidal
- it is sensitive to sampling frequency variation
- less computational complexity is required
- faster estimation is required
- large vibration amplitude and frequency are to be measured
- large carrier deviation due to path length, Doppler effect, and parametric effects are

present in the received signal.

In this research work, a synchronization technique is proposed for extracting the Doppler signal in ultrasonic vibration measurement system using moving window discrete Fourier transform (MWDFT) filter. In this technique, the received ultrasonic signal is tracked for variation in carrier. The quadrature detection is performed with the help of MWDFT. The FM to AM conversion is done by tuned MWDFT. A simple multiplier followed by another MWDFT suppresses the carrier from the received signal and hence the Doppler signal is retrieved. The extracted Doppler signal is further processed to extract the phase modulating signal by sampling period adjustment of the MWDFT. The extracted modulated signal possesses the vibration amplitude and frequency information. These parameters had been obtained for an electrodynamic vibration system by implementing the synchronization technique in FPGA.

3.2 MWDFT-PLL algorithm for Doppler signal extractor

The experimental set-up for the proposed Doppler signal extractor is shown in Fig. 3.1. An electrodynamic vibration test equipment is used to simulate the disc vibration at desired amplitude and frequency. A pair of transducers in which one transducer emits the continuous ultrasonic wave of 40 kHz toward the vibrating disc and another transducer receives the phase modulated ultrasonic signal as shown in Fig. 3.1. An electronic circuit is connected to the transmitting transducer to supply a source of 40 kHz as a carrier beam. The carrier beam propagates towards vibrating object with angle (θ) to the normal of vibrating surface. The transmitting beam is expressed as

$$S_c(t) \quad = \quad A_c \cos(\omega_c t) \qquad (3.1)$$

where A_c is amplitude of carrier signal and ω_c is the angular carrier frequency. The vibrating body obeys the expression

$$a_0 \quad = \quad A_m \sin(\omega_m t) \qquad (3.2)$$

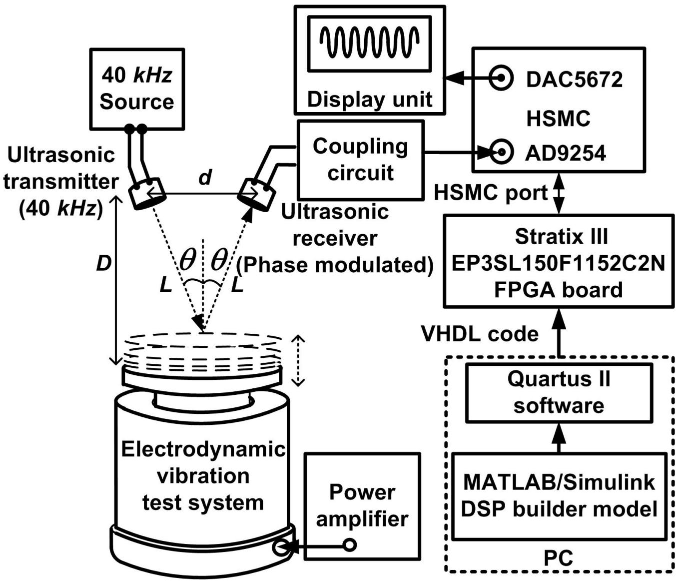

Fig. 3.1: Experimental set-up for the proposed Doppler signal extractor.

where A_m and ω_m are amplitude and angular frequency of vibration respectively. These parameters are need to be estimated using the proposed synchronization technique. The phase modulated received signal from the receiver can be expressed as

$$S_i(t) \quad = \quad A'_c \cos(\omega_c t + \phi_D(t) + \phi_P(t) + \phi_0) \tag{3.3}$$

where A'_c is amplitude of the received signal; the phase shift introduced by surface displacement due to Doppler effect is $\phi_D(t) = \beta \sin(\omega_m t)$; the phase modulation index is $\beta = 2A_m\omega_c \cos(\theta)/c_0$, c_0 is speed of sound; the phase shift $\phi_0 = 2Lk_0 = 2L\omega_c/c_0$ is due to the path length $2L$ between transmitter and receiver and k_0 is wave number; $\phi_P(t)$ is the phase shift introduced by parametric effect which is ignored in the estimation procedure. Therefore, the received signal is phase shifted due to (i) path length ϕ_0, (ii) Doppler effect $\phi_D(t)$, (iii) and parametric effect $\phi_P(t)$.

Considering the speed of ultrasound in air as $c_0 \simeq 346\ m/s$, the phase shift ϕ_0 will be multiple of 2π or wavelength of carrier beam λ_c as long as L is multiple of 4.325 mm. In the proposed method, L can be adjusted in multiple of 4.325 mm so that ϕ_0 term can be completely ignored in further derivation, i.e. (3.3) can be written as

$$S_i(t) \quad = \quad A'_c \cos(\omega_c t + \beta \sin(\omega_m t)) \tag{3.4}$$

where $\beta = \pm\Delta f_c/f_m$; Δf_c is the carrier frequency deviation; f_m is the frequency of vibration. Thus, the range of $\beta : -\Delta f_c/f_m < \beta < +\Delta f_c/f_m$. The received frequency modulated signal (3.4) is applied to the coupling circuit to remove 50 Hz noise and then amplified. Then, the amplified signal is fed to the ADC of high speed mezzanine card (HSMC) for data conversion. The converted digital signal is processed by the synchronization technique shown in Fig. 3.2 to extract the modulating signal. The proposed technique employs MWDFT filter as a quadrature detector, carrier suppressor or Doppler signal extractor, PI controller, and sampling pulse generator.

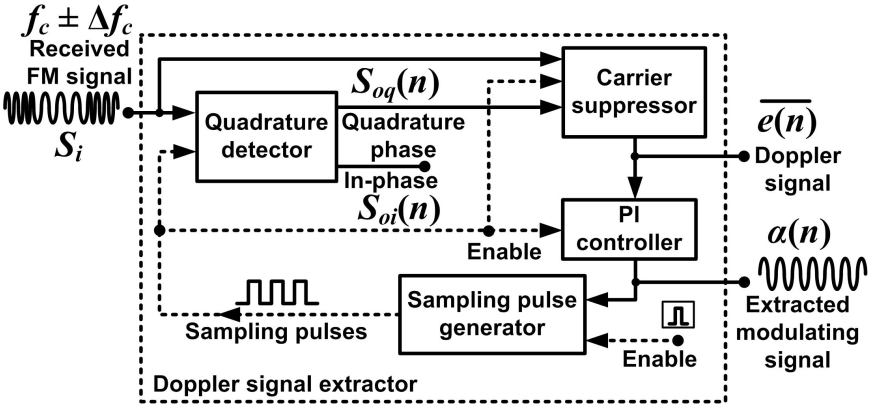

Fig. 3.2: Proposed Doppler signal extractor.

3.2.1 MWDFT filter as a quadrature detector

The MWDFT is deployed as quadrature detector. The block diagram of quadrature detector is shown in Fig. 3.3(a). The MWDFT is an IIR filter consisting of a comb filter [118] followed by a complex resonator. One resonator is driven by a single comb filter to obtain the in-phase and quadrature signals. The difference equation obeyed by MWDFT is

$$\begin{aligned} S_{o1}(n) &= [S_{o1}(n-1) - (2/N)r^N S_i(n-N) \\ &+ (2/N)S_i(n)]re^{j2\pi/N} \end{aligned} \tag{3.5}$$

where N is the window length of the filter; r is the damping factor; $S_i(n)$ is the received discretized ultrasonic signal; $S_{o1}(n)$ is the instantaneous complex signal from the filter

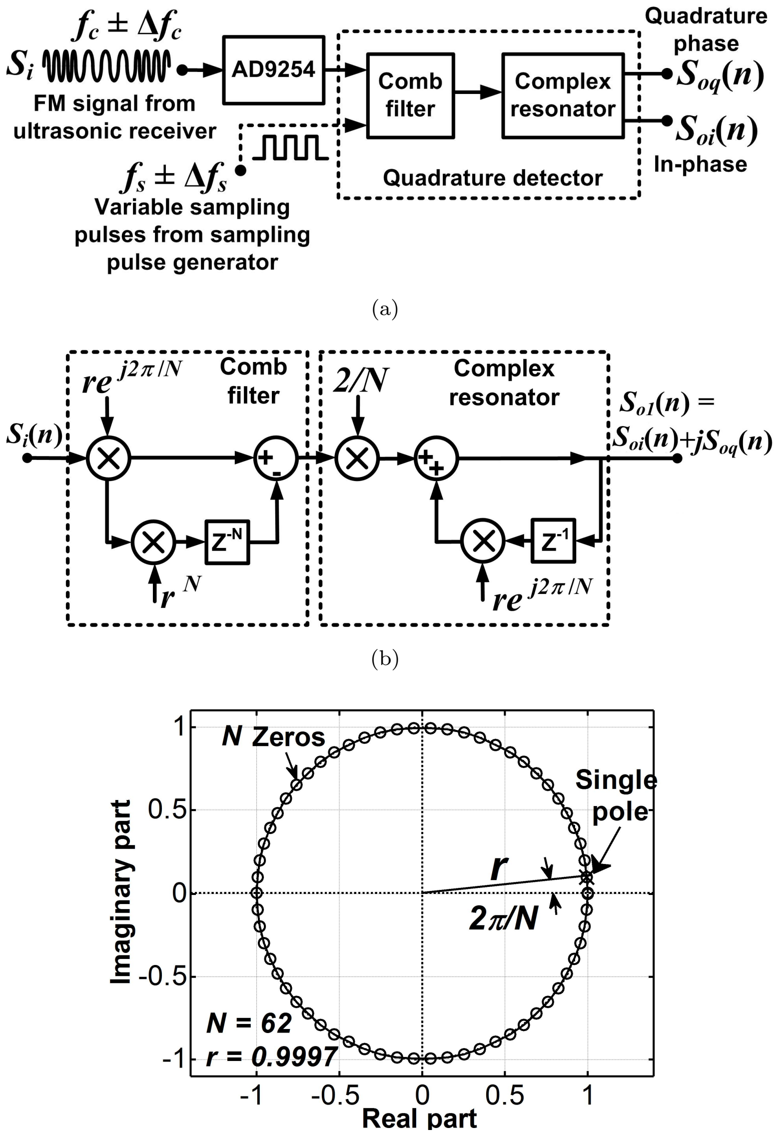

(a)

(b)

(c)

Fig. 3.3: Quadrature detector (a) Quadrature detection based on MWDFT (b) MWDFT structure (c) Pole-zero diagram of MWDFT.

output, $S_{o1}(n) = S_{oi}(n) + jS_{oq}(n)$. The z-domain transfer function of the quadrature detector is obtained as

$$H_{MWDFT1}(z) = \frac{2}{N}\frac{(1 - r^N z^{-N})re^{j2\pi/N}}{1 - re^{j2\pi/N}z^{-1}} \tag{3.6}$$

The comb filter and complex resonator structure of MWDFT is shown in Fig. 3.3(b). This complex filter has N $(= 62)$ zeros equally placed in the z-plane with radius r $(= 0.9997)$. A single complex pole $z = re^{j2\pi/N} = r\cos(j2\pi/N) + jr\sin(j2\pi/N)$ cancels the complex zero at that location as illustrated in Fig. 3.3(c). The frequency response of H_{MWDFT1} can be expressed as

$$H_{MWDFT1}(w) = re^{-j(\omega T(N-1)/2-\pi/N)}\frac{(2/N)\sin(\omega TN/2)}{\sin(\omega T/2-\pi/N)} \tag{3.7}$$

The in-phase $S_{0i}(n)$ (real - part) and quadrature phase $S_{0q}(n)$ (imaginary - part) components are obtained from the quadrature detector (3.6) as

$$\begin{aligned} H_{MWDFT1i}(z) &= \frac{2}{N}\frac{(1-r^N z^{-N})(r\cos(2\pi/N)-r^2z^{-1})}{1-2r\cos(2\pi/N)z^{-1}+r^2z^{-2}} \\ H_{MWDFT1q}(z) &= \frac{2}{N}\frac{(1-r^N z^{-N})(r\sin(2\pi/N))}{1-2r\cos(2\pi/N)z^{-1}+r^2z^{-2}} \end{aligned} \tag{3.8}$$

Two complex poles $z = r\cos(2\pi/N) \pm jr\sin(2\pi/N)$, a conjugate pair present in the in-phase and quadrature components of (3.8). Therefore, in-phase provides real sine signal and quadrature component generates the real cosine signal unlike the complex signal in (3.6). The quadrature detector passes the carrier frequency and rejects the harmonics of carrier by pole-zero cancellation. Therefore, the in-phase (sine) and quadrature (cosine) components of the carrier with its variations had been produced at the output of quadrature detector. The frequency response of the H_{MWDFT1} in-phase component is shown in Fig. 3.4, it could be observed that unit magnitude and zero phase shift at 40 kHz. Hence, it passes the carrier frequency and its variation. From the in-phase and

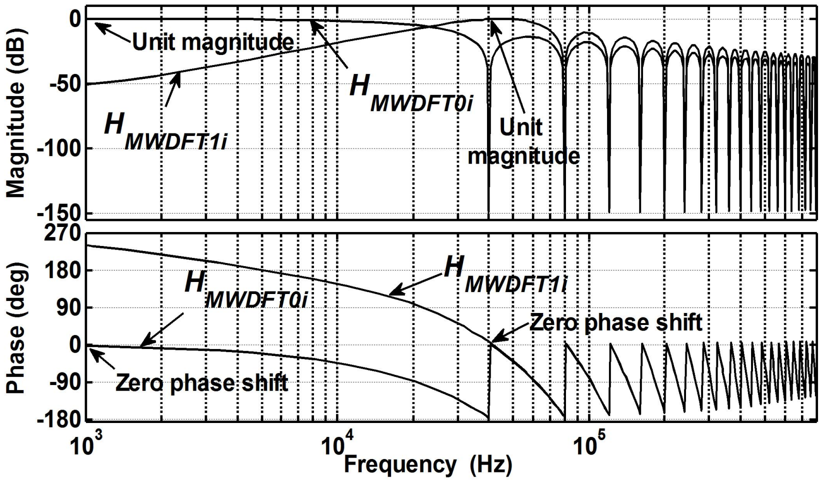

Fig. 3.4: Frequency responses of H_{MWDFT0} and H_{MWDFT1} for center $f_c = 40\ kHz$.

quadrature components of MWDFT1, the magnitude and phase errors are determined for a fixed sampling frequency f_s. The magnitude error and phase curves for r =1 and r = 0.9997 of in-phase and quadrature-phase components are shown in Fig. 3.5. These

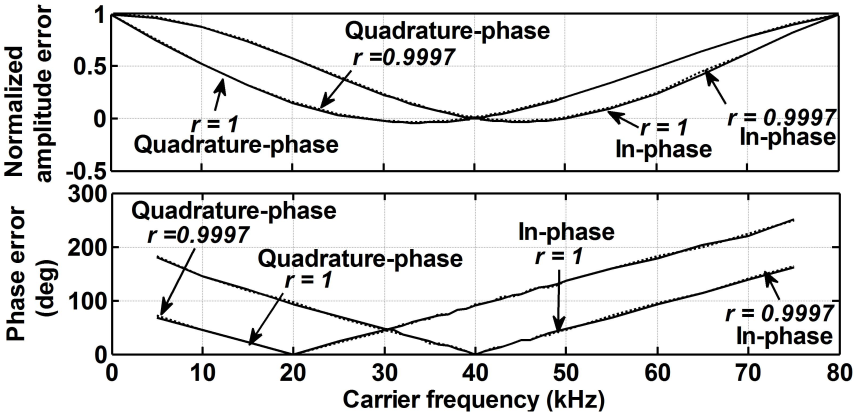

Fig. 3.5: Magnitude and phase error curves of in-phase and quadrature-phase components for center $f_c = 40\ kHz$.

magnitude and phase errors are corrected by adaptive sampling pulse adjustment. When the MWDFT1 is operated at suitable f_s, the quadrature detector converts the received ultrasonic FM signal into AM signal. Thus, the deviation in carrier frequency is reflected as AM at the outputs of quadrature detector. The quadrature component is modeled as

$$S_{oq}(n) \quad = \quad (1 - m \cos \omega_m n) \times A'_{c1} \cos(\omega_c n + \beta \sin \omega_m n + \phi) \tag{3.9}$$

where A'_{c1} is amplitude of FM-to-AM signal; $m = \frac{\Delta f_c}{f_c}$ is amplitude modulation index; ϕ is phase shift introduced by the MWDFT1 which may be either leading or lagging. These amplitude and phase variations of the in-phase and quadrature-phase components would be nullified, when the MWDFT1 starts tracking the $S_i(n)$.

3.2.2 Doppler signal extraction

The quadrature component $S_{oq}(n)$ and the received ultrasonic signal $S_i(n)$ are processed for carrier suppression using a multiplier followed by a moving window filter H_{MWDFT0} as shown in Fig. 3.6(a). The z-domain transfer function of MWDFT0 is expressed as

$$H_{MWDFT0}(z) = \frac{1}{N} \frac{1 - r^N z^{-N}}{1 - r z^{-1}} \tag{3.10}$$

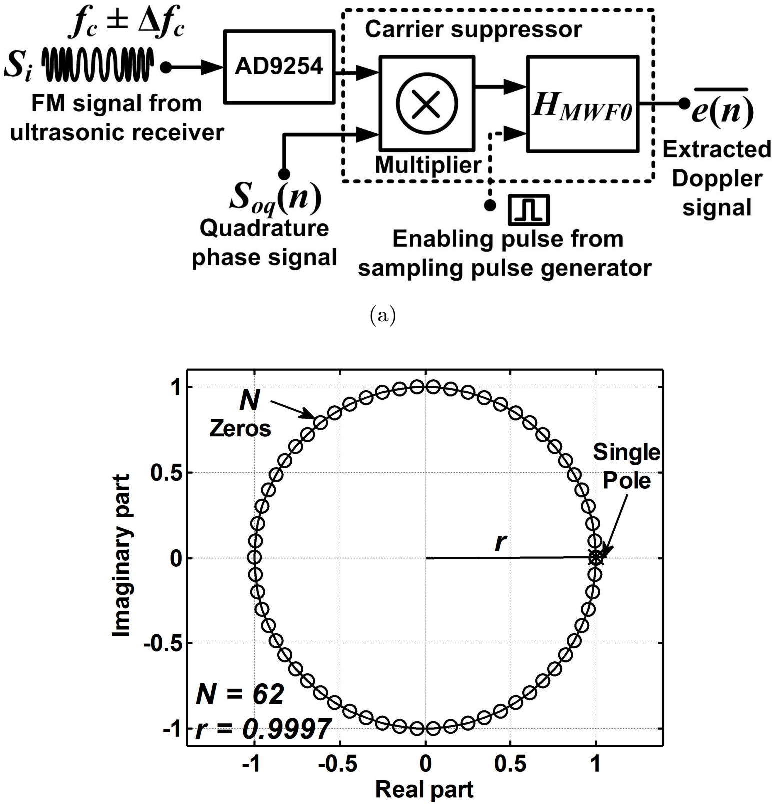

(a)

(b)

Fig. 3.6: Doppler signal extraction (a) Block diagram of Doppler signal extractor (b) Pole-zero diagram of MWDFT0.

The $H_{MWDFT0}(z)$ has N zeros equally spaced in z-plane at radius r and its only one pole at $z = r$ cancels a zero at that location as shown in Fig. 3.6(b), so that the filter can extract d.c. and small frequency variation around d.c. Frequency response of $H_{MWDFT0}(z)$ in-phase component is shown in Fig. 3.4. The unit magnitude and zero phase shift around d.c can be noticed. Therefore, it passes the d.c and its variation and rejects the fundamental and other harmonic frequencies. From the received ultrasonic signal, the carrier is removed by the following process:

$$\begin{aligned}
S_i(n)S_{oq}(n) &= A'_cA'_{c1}[\cos(\omega_c n + \beta\sin\omega_m n)\cos(\omega_c n + \beta\sin\omega_m n + \phi)](1 - m\cos\omega_m n) \\
&= A'_cA'_{c1}[\cos(\omega_c n + \beta\sin\omega_m n)(\sin(\omega_c n + \beta\sin\omega_m n)\cos\phi \\
&+ \cos(\omega_c n + \beta\sin\omega_m n)\sin\phi)](1 - m\cos\omega_m n) \qquad (3.11)
\end{aligned}$$

Bessel function is normally applied to expand a sinusoidal function that contains another sinusoidal function as a phase term. Therefore, (3.11) is expanded through Bessel function to determine the frequency components present in the output of carrier suppressor. Bessel function of (3.11) is

$$\begin{aligned}S_i(n)S_{oq}(n) = A'_cA'_{c1}[\sum_{k=-\infty}^{\infty} J_k(\beta)\cos(\omega_c n + k\omega_m n)(\cos\phi \sum_{k=-\infty}^{\infty} J_k(\beta)\sin(\omega_c n + k\omega_m n) \\ + \sin\phi \sum_{k=-\infty}^{\infty} J_k(\beta)\cos(\omega_c n + k\omega_m n))](1 - m\cos\omega_m n) \qquad (3.12)\end{aligned}$$

Expanding (3.12) up to first order term and removing the carrier through $H_{MWDFT0}(z)$, for $J_0(\beta) \simeq 1$, $J_1(\beta) \simeq \beta/2$, and $J_{-1}(\beta) \simeq -\beta/2$, the extracted Doppler signal is represented as

$$\begin{aligned}\bar{e}(n) &= A'_cA'_{c1}(\beta^2/4 + 1/2)\sin\phi - A'_cA'_{c1}(\beta^2/8)[\sin(2\omega_m n + \phi) - \sin(2\omega_m n - \phi)] \\ &+ mA'_cA'_{c1}(\beta^2/16)[\sin(3\omega_m n + \phi) - \sin(3\omega_m n - \phi)] \\ &- mA'_cA'_{c1}(\beta^2/16 + 1/4)[\sin(\omega_m n + \phi) - \sin(\omega_m n - \phi)] \qquad (3.13)\end{aligned}$$

The vibration signal parameters are present in (3.13). The error signal $\bar{e}(n)$ is considered as Doppler signal after the removal of carrier frequency. The $\bar{e}(n)$ is further processed by PI controller to remove the higher order terms of ω_m.

3.2.3 PI controller

The extracted Doppler signal, (3.13) is applied to the PI controller as shown in Fig. 3.7. The output of PI controller is expressed as

$$\alpha(n) = K_P\bar{e}(n) + K_I\bar{e}(n) + \alpha(n-1) \qquad (3.14)$$

where K_P and K_I are proportional and integral gains. The K_P and K_I values are chosen to remove integer multiple of ω_m from (3.13). The amplitude of α_{p-p} is limited to ±1. The $\alpha_{p-p}(n)$ can be related with carrier deviation as

$$\alpha_{p-p}(n) = \cos\left(\frac{2\pi(f_c \pm \Delta f_c)N}{f_{ena}}\right) \qquad (3.15)$$

where f_{ena} is the enabling frequency of the sampling generator. Thus, the modulating signal is extracted as α_{p-p} and the vibrating parameters can be estimated from (3.15).

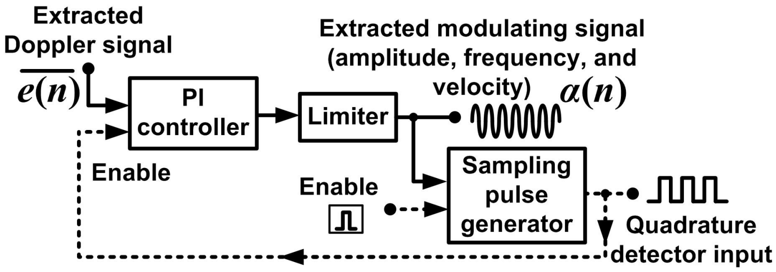

Fig. 3.7: PI controller and sampling pulse generator.

From the α_{p-p}, the Δf_c could be computed. Using the expression of β and Δf_c, the vibration amplitude A_m can be determined.

3.2.4 Sampling pulse generator

The SPG is a cascade connection of quadrature type oscillator and zero-crossing detector. The block diagram representation of SPG is shown in Fig. 3.8. The difference equation

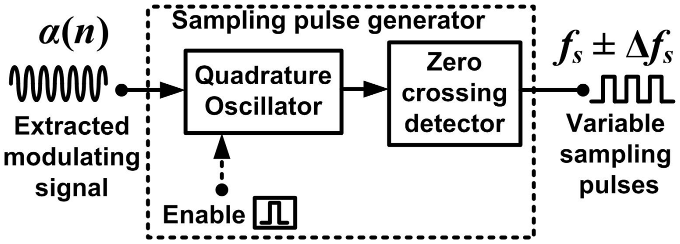

Fig. 3.8: Sampling pulse generator (SPG).

of the oscillator is

$$\begin{aligned} x(n) &= \alpha x(n-1) + (\alpha-1)y(n-1) \\ y(n) &= (\alpha+1)x(n-1) + \alpha y(n-1) \end{aligned} \tag{3.16}$$

This oscillator generates the sine $x(n)$ and cosine $y(n)$ signals of required f_s, which could be varied with respect to the extracted modulating signal. Further, the zero-crossing detector converts the variable f_s into variable sampling pulses. The SPG outputs the sampling pulses to moving window filters and PI controller. The sampling pulses are proportional to α_{p-p} which in turn reflects the carrier frequency deviation. Therefore, the modulating signal adjusts the sampling generator to provide the correct sampling pulses

$f_s \pm \Delta f_s$. These pulses enable the MWDFT1, MWDFT0, and PI controller to correct the error observed at the output of in-phase and quadrature-phase components. At steady state, the $\alpha(n)$ retrieves the modulating signal consisting of vibration amplitude A_m and vibration frequency f_m.

3.2.5 Linearized model of MWDFT-PLL

The linearized model of Fig. 3.2 is shown in Fig. 3.9. Time-domain input signal of amplitude A_1 and drift frequency $f_1 = f_0 + \Delta f$ is

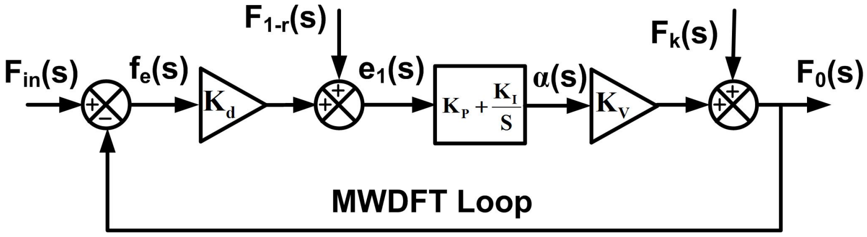

Fig. 3.9: Linearized model of MWDFT-PLL

$$\begin{aligned} S_i(t) &= A_1 \sin(2\pi f_1 t) \\ &= A_1 \sin(2\pi(f_0 + \Delta f)t) \end{aligned} \tag{3.17}$$

where f_0 is the center frequency and Δf frequency deviation in input signal. The input signal S_i is applied to the quadrature detector (MWDFT filter). The resultant real part (S_{oi}) and quadrature part (S_{oq}) are

$$\begin{aligned} S_{oi}(t) &= A_2 r \sin(2\pi f_1 t \pm r\Delta\phi_1) \\ &\simeq A_2 \sin(2\pi f_1 t \pm \Delta\phi_1) + A_2(r-1)\sin(2\pi f_1 t \pm (r-1)\Delta\phi_1) \end{aligned} \tag{3.18}$$

$$\begin{aligned} S_{oq}(t) &= -A_2 r \cos(2\pi f_1 t \pm r\Delta\phi_1) \\ &\simeq -A_2 \cos(2\pi f_1 t \pm \Delta\phi_1) - A_2(r-1)\cos(2\pi f_1 t \pm (r-1)\Delta\phi_1) \end{aligned} \tag{3.19}$$

where A_2 is the amplitude of the MWDFT output signals, r is the damping factor and $\Delta\phi_1$ is the phase shift introduced by input drift frequency. The change in step input frequency produces the MWDFT output signals of same frequency but introduces phase shift $\Delta\phi_1$. Thus, a phase detector is required for correcting the introduced phase. The phase detector gain K_d is obtained from the slope of the phase detector characteristics. After linearization, K_d was found to be 20.0065 / Hz. During the locking process, the MWDFT PLL keeps correcting the change in phase $\Delta\phi_1$ caused by drift in input signal frequency. Also, the introduction of r causes magnitude and phase errors in the MWDFT output signals. So the effect of r has been modelled as F_{1-r} signal ($\simeq 1-r$), which is added to the phase detector output signal and the error e_1 is determined as shown in Fig. 3.9. The PI controller with the proportional gain K_p and integral gain K_I, processes the error e_1 and produces control signal α signal which is passed to the SPG unit. The linearised SPG characteristics could be expressed by $F_0(s) = K_v\alpha(s) + F_k(s)$, where $K_v = 237$ is the SPG gain obtained from the slope of the SPG characteristics and $F_k(s) = f_s/N$ is the center frequency of the SPG; f_s is sampling frequency. From Fig. 3.9, the transfer function model of MWDFT PLL, relating to the input frequency $F_{in}(s)$, the effect of damping factor $F_{1-r}(s)$ and center frequency of SPG $F_k(s)$ can be written as

$$\begin{aligned} F_0(s) &= \frac{K_1 s + K_3}{(1+K_1)s + K_3} \quad F_{in}(s) + \frac{s}{(1+K_1)s + K_3} \quad F_k(s) \\ &+ \frac{K_pK_vs + K_IK_v}{(1+K_1)s + K_3} \quad F_{1-r}(s) \end{aligned} \tag{3.20}$$

where $K_1 = K_dK_pK_v$ and $K_3 = K_dK_vK_I$. The transfer function of error E_1 is

$$\begin{aligned} E_1(s) &= \frac{K_d s}{(1+K_1)s + K_3} \quad F_{in}(s) + \frac{-sK_d}{(1+K_1)s + K_3} \quad F_{k0}(s) \\ &+ \frac{s}{(1+K_1)s + K_3} \quad F_{1-r}(s) \end{aligned} \tag{3.21}$$

The transfer function of frequency error F_e is

$$\begin{aligned} F_e(s) &= \frac{s}{(1+K_1)s + K_3} \quad F_{in}(s) + \frac{-s}{(1+K_1)s + K_3} \quad F_{k0}(s) \\ &+ \frac{-K_pK_vs - K_IK_v}{(1+K_1)s + K_3} \quad F_{1-r}(s) \end{aligned} \tag{3.22}$$

3.2.6 Velocity measurement along with vibration parameters

When vibrating object is moving with constant velocity, the received ultrasonic signal (3.4) can be expressed as

$$S_i(t) = A_c \cos(\omega_c t + \beta \sin(\omega_m t) + \beta_v t) \tag{3.23}$$

where, $\beta_v = 2\omega_c v \cos(\theta)/c_0$ is the second modulation index due to velocity component (v). The velocity term introduces another dc component in (3.15), which is proportional to velocity itself. Therefore, vibration amplitude and velocity can be easily estimated simultaneously by measuring $\alpha(n)$.

3.3 Simulation results

The proposed method is tested for estimating vibration parameters with various modulating signals through $\bar{e}(n)$ and $\alpha(n)$. The synchronization technique is simulated using Altera DSP builder components in MATLAB/Simulink environment. An input signal as (3.4) with 40 kHz carrier is generated to test the performance of the proposed technique. The number of samples per cycle of the carrier is $N = 62$. The MWDFT1 is tuned to a center frequency of 40 kHz ultrasonic carrier. Therefore, the enabling frequency of the proposed algorithm is 40 $kHz \times 62 \times 4 = 9.92$ MHz.

Table 3.1: Performance of the proposed method for $f_c = 40$ kHz, $\theta = 10°$, $c_0 = 346$ m/s, $K_P = 0.01$ (Simulation)

f_m (Hz)	K_I	β range	Max. A_m (mm)	α_{p-p}	Estimated A_m (mm)	% error in A_m
10	0.003	0.2 - 3000.0	2096.89	1.8473	2095.83	0.05
100	0.003	0.2 - 300.0	209.68	1.8475	209.63	0.02
200	0.010	0.2 - 150.0	104.84	1.8480	104.87	0.08
500	0.010	0.2 - 60.0	41.94	1.8510	42.09	0.36
1000	0.010	0.2 - 10.0	6.99	0.7677	7.01	0.32
2000	0.010	0.2 - 5.0	3.49	0.7705	3.52	0.70
3000	0.011	0.2 - 2.0	1.40	0.4720	1.41	1.12
4000	0.011	0.2 - 1.0	0.70	0.3112	0.70	0.53
5000	0.012	0.2 - 1.0	0.70	0.3915	0.70	0.34
6000	0.012	0.2 - 0.5	0.35	0.2302	0.34	2.08

3.3.1 Vibration parameters

The maximum carrier deviation is determined by applying step change in carrier frequency. The positive carrier step of 39 kHz is applied for 40 kHz center frequency (40 - 79 kHz) at the input. The synchronization between MWDFT1 in-phase output and received ultrasonic signal is achieved. Similarly, the maximum carrier deviation for the negative step (40 - 6 kHz) was found to be 34 kHz. Therefore, carrier frequency range was found to be 6 - 79 kHz with respect to a center frequency of 40 kHz, for $K_P = 0.01$ and $K_I = 0.003$. As K_I increases the operating range becomes smaller. Therefore, the product of vibration amplitude and frequency (βf_m) can affect the carrier deviation by maximum ± 34 kHz. Hence, the carrier deviation of ± 34 kHz can be tracked. Within this range, either A_m or f_m can be varied at the input and carrier tracking could be achieved. Various vibration frequencies f_m, the tolerable range of β, and the estimated vibration amplitudes from $\alpha_{p-p}(n)$ are listed in Table 3.1. It could be observed that as the vibration frequency increases, the K_I should be increased to reduce error in the estimated vibration amplitude. Hence, simulation results conclude that the vibration amplitude of 2095.83 mm for low frequency vibration of 10 Hz to 0.34 mm for the high frequency vibration of 6 kHz could be measured. The maximum percentage error observed in the vibration amplitude is 2.08%. The Doppler signal extractor is tested with the data provided in Table 3.1. The input to the algorithm is applied with β of 10 and $f_m = 1$ kHz for initial 1.3 ms and at 1.3 ms the β is changed to 0.5 and f_m is set to 6 kHz. The performance of the technique for these two cases of β and f_m are shown in Fig. 3.10. The input FM signal, the in-phase and quadrature components of the MWDFT are shown in trace 1, trace 2, and trace 3 respectively. The extracted Doppler signal for $f_m = 1$ kHz and $f_m = 6$ kHz is shown in trace 4. The retrieved modulating signal with $\beta = 10$ and $\beta = 0.5$ is shown in trace 5. To improve the clarity, the generated adaptive sampling pulses are shown for 0.84 s in trace 6.

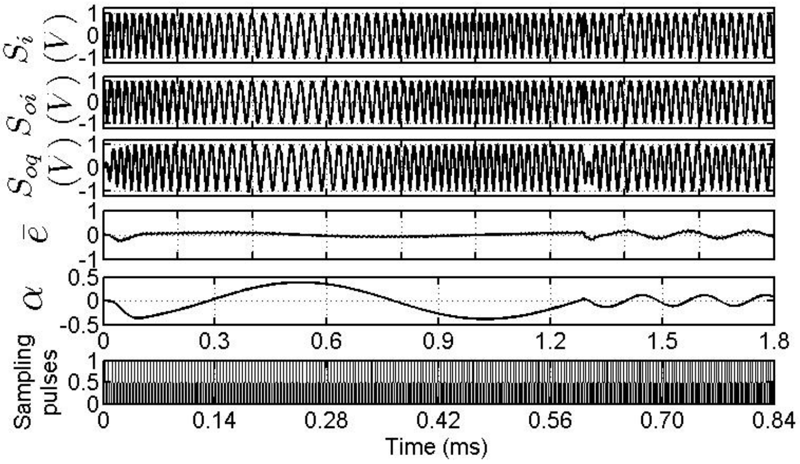

Fig. 3.10: Input signal, MWDFT in-phase component, MWDFT quadrature component, Doppler signal, retrieved modulating signal, and sampling pulses (Simulation).

3.4 Implementation of the proposed scheme

3.4.1 Experimental set-up

The proposed measurement system is shown in Fig. 3.1. The experimental set-up consists of a pair of 40 kHz ultrasonic transducer, the GL 40 - 2T and GL 40 - 2R as shown in Fig. 3.11. This pair is used for experiments and its specification is provided in Table 3.2. From function generator, the ultrasonic carrier of 40 kHz is fed to the transmitting transducer. The frequency modulated signal reflected from vibration test equipment is received at the target transducer. Electrodynamic vibration test system is used as test object for this experiment. The micron make electrodynamic vibration test equipment consists of power amplifier (model: MPA-0050) as shown in Fig. 3.12 and electrodynamic vibration generator, i.e. dynamic shaker (model: MEV-0050) as shown in Fig. 3.13. It

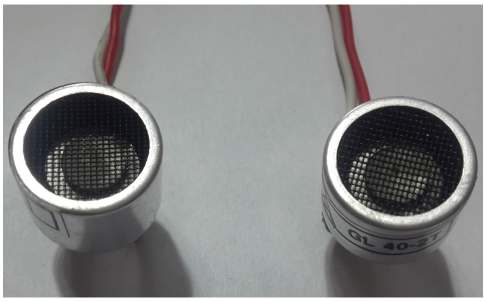

Fig. 3.11: A pair of Ultrasonic transducer (40 kHz center frequency)

Table 3.2: Specification of ultrasonic transducer

Parts number	Transmitter (GL 40-2T)	Receiver (GL 40-2R)
Center frequency	40.0 ± 1.0 kHz	40.0 ± 1.0 kHz
Driving voltage	20 V (RMS)	20 V (RMS)
Bandwidth	5.0 kHz / 100 dB	5.0 kHz / -75 dB
Sound pressure level	112 dB/40 ± 1.0 kHz	NA
Sensitivity	NA	67 dB/40 ± 1.0 kHz
Operating temperature	-20°C to +70°C	-20°C to +70°C
Capacitance	2000 pF ± 20%	2000 pF ± 20%
Operating range	2 m	-

has a frequency range of 1 Hz - 10 kHz. Power amplifier could excite the dynamic shaker for displacement.

Fig. 3.12: Power amplifier to excite electrodynamic shaker at different frequencies

3.4.1.1 Analog circuit

An Agilent function generator (model 33220 A) with 20 MHz bandwidth is used to generate the 40 kHz ultrasonic signal at the transmitter. The ultrasonic signal of 100 mV peak-to peak is fed to the ultrasonic transducer GL 40 - 2T. The transducer pair is placed to face towards the dynamic shaker at an angle $\theta = 10°$ to the normal of the plane surface. The horizontal distance between the two transducers $d = 2.4$ cm, the vertical

Fig. 3.13: Electrodynamic shaker

distance between transducers and shaker $D = 6.8\ cm$. To avoid the larger phase shift (ϕ_0) due to path length, the d/D ratio is chosen to maintain the angle less than 10°. The ultrasonic receiver circuit is shown in Fig. 3.14. The received ultrasonic signal is fed to the amplifier circuit designed using OP27 OPAMP. The amplified output is connected to SubMiniature connector A (SMA) through the serial interface circuit to ADC (AD 5294) of data conversion HSMC. The input signal is sampled at 150 MS/s and the maximum voltage limit is 2 V. The chip select signal (CNTL - control signal) is applied to the ADC through HSMC port from FPGA. The chip select signal controls the read and write cycles of the ADC. The data conversion card is connected to the Stratix III FPGA board with FPGA chip EP3SL150F1152C2N through HSMC port connector as shown in Fig. 3.15. The on-board clock of 50 MHz is used for processing. Further, FPGA generates the ADC clock (CLK_A), which synchronizes the serial interface read and write cycles.

3.4.1.2 Digital circuit

From ADC, the 14-bit digital data is passed to the FPGA through HSMC port to process the received signal. The digitized signal is amplified and sampled at 10 MHz at the input of synchronization process. The proposed scheme is designed in MATLAB/Simulink DSP builder and these blocks are shown in Fig. 3.16. Then, the DSP builder blocks are converted to VHDL code with the help of Quartus II synthesizer. After successful

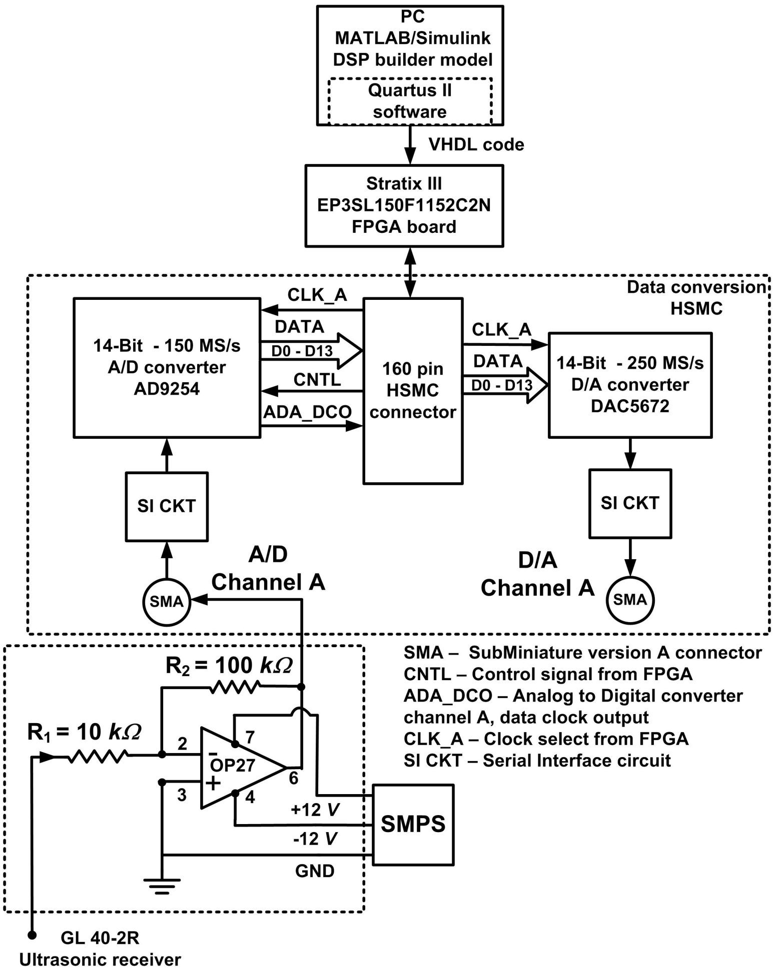

Fig. 3.14: Receiver circuit of the proposed measurement system.

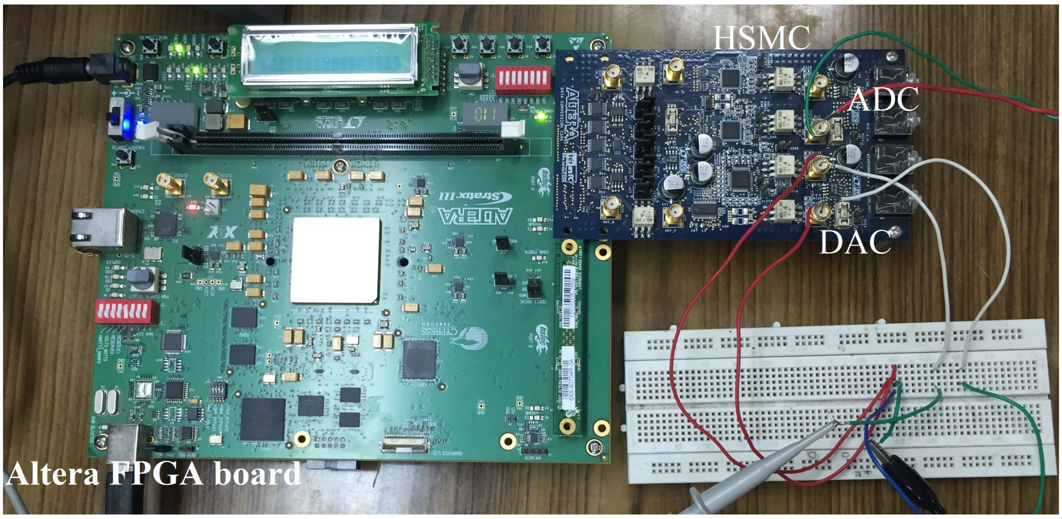

Fig. 3.15: Altera FPGA board with HSMC connector

compilation, the converted VHDL code is downloaded to the FPGA board through USB-Blaster JTAG connection. The processed 14-bit digital data and clock select from FPGA are fed to the DAC (DAC 5672) through HSMC port. The analog output is collected through the serial interface circuit for display and these units are shown in Fig. 3.17.

3.4.2 Performance of the Doppler signal extractor

A frequency modulated wave S_i is generated by the function generator with a carrier frequency of 40 kHz. From 50 MHz FPGA clock, a 10 MHz clock is derived to enable the various blocks of the algorithm. The 40 kHz FM carrier is modulated by 10 kHz sine wave with $\beta = 0.2$ and fed to the ADC of FPGA board. The performance of the proposed method with retrieved modulating signal α_{p-p} is shown in Fig. 3.18. These intermediate signals are tapped from FPGA for 8192 samples using signal tap analyzer. The received ultrasonic signal S_i is shown in Fig. 3.18 trace 1. The in-phase S_{oi} and quadrature S_{oq} components obtained from the quadrature detector are shown in trace 2 and trace 3 respectively. The extracted Doppler signal $\bar{e}$ after carrier removal is shown in trace 4. The α which carries the information of A_m and f_m is shown in trace 5. The sampling pulses of SPG are shown in trace 6. The received signal is processed using the synchronization technique in the FPGA and α_{p-p} of the extracted modulating signal is measured. Further, the vibration amplitude A_m can be determined as

$$\begin{aligned}\pm\Delta f_c &= \frac{f_{ena}}{2\pi N}\cos^{-1}(\alpha_{p-p}) - f_c \\ A_m &= \frac{\pm\Delta f_c \; c_0}{2 f_m \omega_c \cos(\theta)}\end{aligned} \tag{3.24}$$

Likewise, the modulating frequency is varied from 10 Hz to 2000 Hz for different β. This test cases are listed in Table 3.3. The α_{p-p} is measured for each test case and A_m is computed using (3.24). The vibration amplitude errors for various carrier deviation in mm are provided in Table 3.3. Since the f_{ena} is chosen as 10 MHz, the center carrier frequency f_c is 10 $MHz/(4 \times 62) = 40.32258$ kHz. The proposed method can estimate A_m of 1365 mm and f_m of 2 kHz for $K_P = 0.01$, and $K_I = 0.03$. This range could be

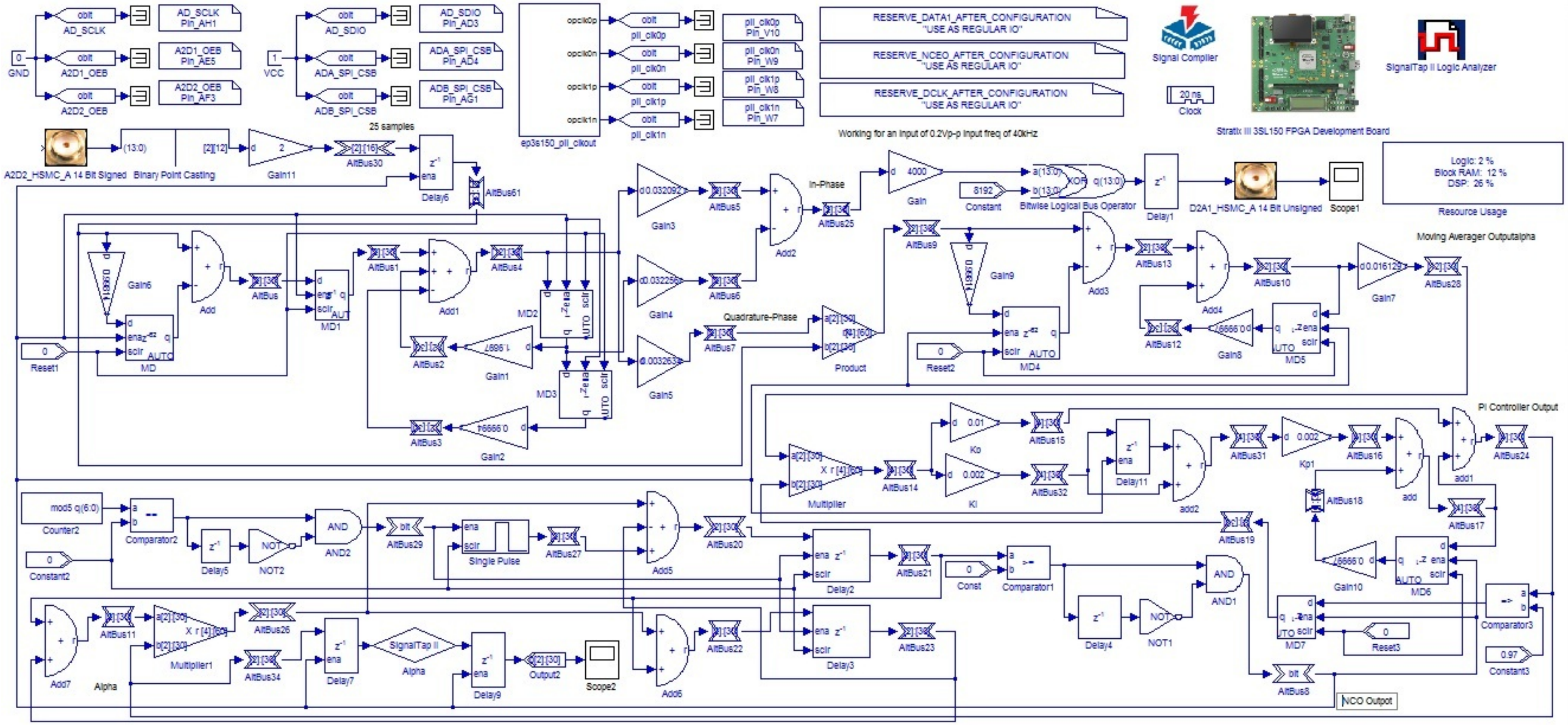

Fig. 3.16: Implementation of MWDFT-PLL algorithm for vibration measurement

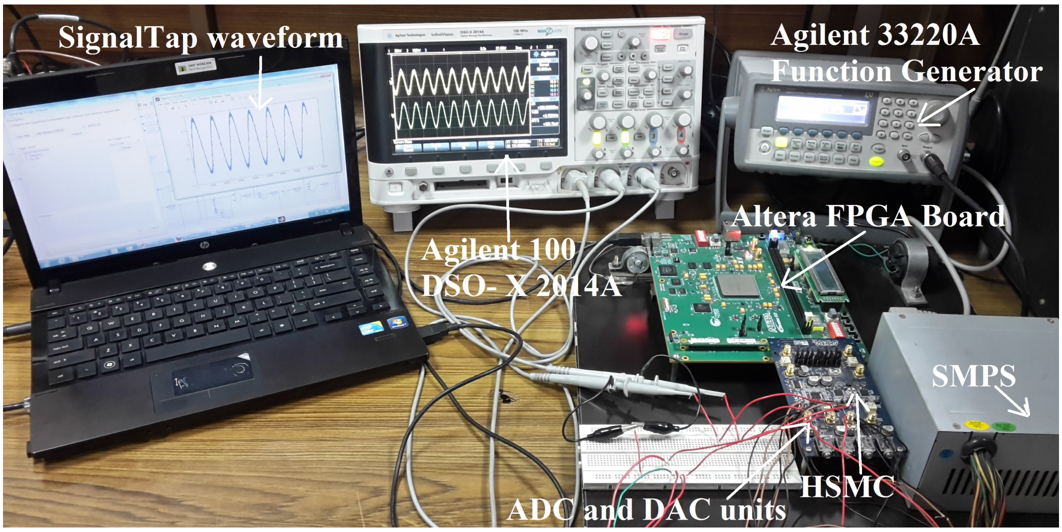

Fig. 3.17: Vibration measurement system with display units

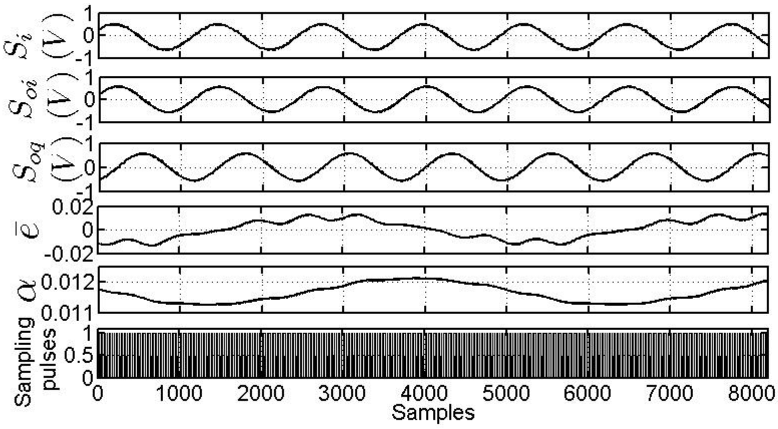

Fig. 3.18: Tapped intermediate signals of proposed synchronization technique (Experiment).

adjusted from the inference given in Table 3.1. The maximum percentage error in the estimation of A_m was found to be 2.76% at low frequency of vibration.

The signal tap analyzer could tap maximum of 8192 samples for a single tap from FPGA. To analyze the spectrum of MWDFT1 and extracted vibration signal outputs, these signals are recorded and plotted with a offline tool. For Table 3.3 data of $f_m = 2\ kHz$ and $\beta = 1$, the MWDFT1 in-phase signal is shown in Fig. 3.19 trace 1. The spectrum shown in trace 2 confirms the presence of 40 kHz, 38 kHz and 42 kHz frequency components. The extracted α_{p-p} is plotted in trace 3 and its spectrum is shown in trace 4. The spectrum of vibration signal shows the presence of 2 kHz frequency. Similarly, for $f_m = 2\ kHz$ and $\beta = 4$, the results are shown in Fig. 3.20. Trace 1 shows the MWDFT1 in-phase

Table 3.3: Measured α_{p-p} for different f_m and β, for $N = 62$, $r = 0.9997$, $f_c = 40.32258\ kHz$, $K_P = 0.01$, $K_I = 0.03$.

f_m (Hz)	various β											
10		$\beta = 100$			$\beta = 150$			$\beta = 1000$			$\beta = 2000$	
	α_{p-p}	A_m (mm)	% error	α_{p-p}	A_m (mm)	% error	α_{p-p}	A_m (mm)	% error	α_{p-p}	A_m (mm)	% error
	0.0770	68.54	1.94	0.1145	101.95	2.6	0.7585	692.4	0.95	1.3880	1365.23	2.34
100		$\beta = 50$			$\beta = 100$			$\beta = 150$			$\beta = 200$	
	0.3890	34.84	0.31	0.7485	68.27	2.32	1.0890	102.48	2.25	1.3910	136.89	2.07
200		$\beta = 10$			$\beta = 60$			$\beta = 100$			$\beta = 130$	
	0.1530	6.81	2.50	0.8980	41.40	1.19	1.3920	68.51	1.98	1.6880	89.41	1.60
500		$\beta = 5$			$\beta = 10$			$\beta = 50$			$\beta = 55$	
	0.2010	3.58	2.54	0.3850	6.90	1.34	1.6500	34.54	1.18	1.7430	37.67	2.01
1000		$\beta = 1$			$\beta = 5$			$\beta = 10$			$\beta = 25$	
	0.0780	0.69	0.66	0.3860	3.45	1.09	0.7530	6.87	1.70	1.6550	17.35	0.72
2000		$\beta = 0.5$			$\beta = 1$			$\beta = 5$			$\beta = 7$	
	0.0790	0.35	0.61	0.1585	0.71	1.01	0.7670	3.50	0.23	1.0650	5.00	2.14

component, and its spectrum is shown in trace 2. The increase in vibration amplitude could also be observed from its spectrum and the presence of frequency components 40 kHz, 38 kHz and 42 kHz. The extracted vibration signal and its spectrum are shown in trace 3 and trace 4 respectively. Trace 4 confirms the presence of 2 kHz vibration frequency. Scaling factor of 10 is applicable to these data with respect to Table 3.3 data. To validate the performance of the algorithm, experimental investigation with the vibration equipment is carried out. The performance of the algorithm is compared with results obtained from the FM carrier which is generated by function generator. The comparison results are provided in Table 3.4. For various f_m frequencies, the α_{p-p} is measured for the both received signals. The S_i signal received from ultrasonic transducer

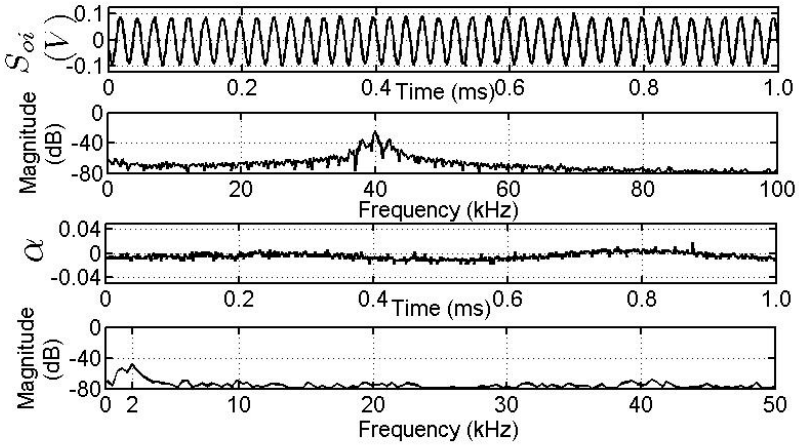

Fig. 3.19: MWDFT1 in-phase component and its spectrum, extracted modulating signal and its spectrum for $f_m = 2$ kHz and $\beta = 1$ (Experiment).

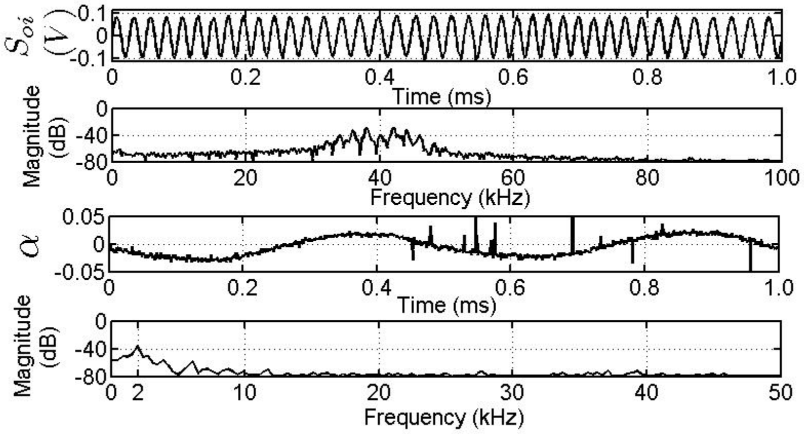

Fig. 3.20: MWDFT1 in-phase component and its spectrum, extracted modulating signal and its spectrum for $f_m = 2$ kHz and $\beta = 4$ (Experiment).

of the vibration equipment is mentioned in the Table 3.4 as S_i from test equipment (T. E.). Another received signal S_i is generated from the function generator (S_i from F. G). The measured α_{p-p} for both cases are compared and found that these values are almost equal. From the α_{p-p}, A_m is measured through the computation of β. These test cases are repeated for different carrier deviations. It is inferred from Table 3.4 that the peak-peak value of the demodulated signal is almost equal for FM signal generated by function generator and the signal received from the ultrasonic receiver. Thus, the algorithm can efficiently extract the vibration information. The vibration frequency is limited to 100 Hz for the proposed equipment because of the 40 kHz ultrasonic transducers employed in the hardware. However, the proposed algorithm can extract the wide variation in FM of 2 kHz as given Table in 3.3. Furthermore, the algorithm could extract maximum ±34 kHz variation in carrier either in terms of frequency or amplitude.

3.4.3 Resource utilization and power dissipation

The proposed synchronization technique for vibration parameter estimation is implemented in Stratix III FPGA chip EP3SL150F1152C2N. The resource utilization summary is given in Table 3.5. The resources consumed by the algorithm is logic blocks of 2%, Block RAM of 12%, and DSP block elements of 26%. The details of adaptive look up tables (ALUTs) and registers included in the logic blocks, 18-bit multipliers of FPGA are provided in Table 3.5. The proposed algorithm can be fit into the FPGA device with 13.34% resources. The resource utilization comparison was made with other techniques proposed in [48], [53]. The algorithm for angular measurements of vibrating shafts [53] consumes 94% of the resources. The harmonic measurement algorithm [48] based on modulated MWDFT filter consumes 35% of the resources. The power dissipation of the proposed algorithm is estimated by the power analyzer tool. The core dynamic power dissipation was found to be 71.83 mW, core static thermal power dissipation is 617.70 mW and I/O thermal power dissipation is 95.48 mW. Therefore, the total thermal power dissipation is 785.00 mW.

Table 3.4: Measured α_{p-p} for different f_m and $N = 62$, $r = 0.9997$, $f_c = 40.32258\ kHz$, $K_P = 0.01$ $K_I = 0.03$

$f_m(Hz)$	Test equipment																	
	S_i from T. E.			S_i from F. G.			S_i from T. E.			S_i from F. G.			S_i from T. E.			S_i from F. G.		
	α_{p-p}	A_m mm	β	α_{p-p}	A_m mm	β	α_{p-p}	A_m mm	β	α_{p-p}	A_m mm	β	α_{p-p}	A_m mm	β	α_{p-p}	A_m mm	β
20	0.0043	1.90	2.74	0.0040	1.80	2.54	0.0084	3.70	5.35	0.0080	3.60	5.09	-	-	-	-	-	-
30	0.0048	1.40	2.08	0.0040	1.20	1.70	0.0090	2.70	3.82	0.0080	2.40	3.40	0.0134	4.00	5.69	0.0130	3.90	5.52
40	0.0044	0.98	1.40	0.0040	0.89	1.27	0.0090	2.00	2.86	0.0090	2.00	2.86	0.0130	2.90	4.14	0.0120	2.70	3.82
50	0.0040	0.71	1.02	0.0034	0.61	0.87	0.0074	1.30	1.88	0.0070	1.20	1.78	0.0108	1.90	2.75	0.0100	1.80	2.55
60	0.0030	0.44	0.64	0.0026	0.39	0.55	0.0062	0.92	1.32	0.0058	0.86	1.23	0.0090	1.30	1.91	0.0084	1.20	1.78
70	0.0030	0.38	0.55	0.0030	0.38	0.55	0.0054	0.68	0.98	0.0050	0.64	0.91	0.0086	1.10	1.56	0.0082	1.00	1.49
80	0.0020	0.22	0.32	0.0016	0.18	0.25	0.0050	0.55	0.79	0.0044	0.49	0.70	0.0070	0.78	1.11	0.0064	0.71	1.01
90	0.0020	0.20	0.28	0.0020	0.20	0.28	0.0038	0.37	0.54	0.0032	0.32	0.45	0.0054	0.53	0.76	0.0050	0.49	0.71
100	0.0018	0.16	0.23	0.0016	0.14	0.20	0.0040	0.36	0.51	0.0040	0.36	0.51	0.0054	0.48	0.68	0.0050	0.44	0.63

Table 3.5: Resource utilization using Stratix III FPGA EP3SL150F1152C2N in the proposed technique

Logic blocks	Block RAM	DSP block 18-bit elements
2% includes ALUTs = 1044/113600 (< 1%) includes dedicated logic registers = 1864/113600 (2%)	12% 675584/5630976	26% 100/384

3.4.4 Effect of active devices and other elements

The main advantages of this ultrasonic vibration measurement system are high resolution, low cost, non-contact measurement, and it can be easily installed. The factors affecting the performance of the proposed system are (i) interference (ii) air turbulence (iii) temperature variation (iv) OPAMP features.

(i) Interference between transmitter and receiver occurs if the transmitted and received waves occupy the same space. Therefore, the distance between transmitter and receiver should be set accordingly. In the proposed system, it is kept as 2.4 cm. Further, the presence of power- line interference in the received signal affects the measurement. A small resistor connected across the receiver terminals can remove the 50 Hz noise. (ii) Air turbulence between the transducers, the vibration object and transducers must be avoided to nullify the measurement error. Air turbulence will expand and contract the wavelength of the ultrasound. Therefore, the measurable range of the object vibration amplitude is mainly dependent on the degree of attenuation of the reflected ultrasound. The reflecting surface must be solid, large, and smooth enough to reflect ultrasound.

(iii) Ultrasonic transmitters and receivers are very sensitive to environmental temperature variations. The temperature and air pressure should be kept unchanged to avoid an error in measurement. In the amplifier circuit, thermoelectric voltages generated by dissimilar metals at the input terminal contacts of OPAMP can degrade the performance. Therefore, best operation will be obtained when both input contacts are maintained at the same temperature.

(iv) Slew rate can result in a nonlinear distortion of rapidly-varying signals applied to the amplifier input.

3.4.5 Comparison with existing techniques

The proposed method is compared with the existing techniques, those employ the ultrasonic transducers of 40 kHz. The measurable vibration amplitude range is 0.35 - 1365 mm and vibration frequency is 2 kHz. For high frequency vibration, the carrier modulation could not be detected by the 40 kHz ultrasonic transducers. However, the synchronization technique could extract α_{p-p} for the combination of either large β and small f_m or small β and large f_m. Furthermore, the proposed method is compared with existing β estimation techniques and the comparison results are presented in Table 3.6. Furthermore, the proposed technique is also compared with other vibration measurement techniques and the results are provided in Table 3.7.

3.4.5.1 Impure/distorted received signal

(i) The β estimation techniques: When the ultrasonic received signal is not purely sinusoidal, the conventional method [2], ratio method [37], Kalman filter [44], and zero-crossing method [53] fail to estimate the β and hence, vibration parameters could not be estimated properly. Further, truncated received sinusoid causes large bias in conventional method. The phase-operation method [33], correlation method [39], and standard deviation method can tolerate only 10% nonlinearity in the received signal. However, the proposed method can perform well in presence of harmonics, because the MWDFT rejects harmonics.

(ii) Other techniques: When the received signal contains harmonics, the PLL [48] and extended DACM [35] can remove harmonics. The CPPM [116] technique is insensitive to channel distortions. The proposed technique removes harmonics and distortions due to the presence of tuned MWDFT.

Table 3.6: Comparison with modulation index estimation techniques

Methods	Impure / Distorted S_i	Presence of noise	f_s variation	Phase shift - path length and Doppler	Frequency range	Amplitude range
Conventional [2], [33]	No	No	NA	Yes	$< 25\ Hz$	734.0032 mm max.
Phase-operation [33]	Up to 10% nonlinearity	Noise is amplified	Sensitive	NA	NA	Large vibration
Ratio [38]	No	Poor SNR	No	Yes	100 - 400 Hz	100 μm
Correlation [33], [39], [119]	Up to 10%	Up to 20 dB	No	Yes	5 Hz - 1.5 kHz, 1 - 2 Hz (HR)	10 μm - 1 mm, 0.2 - 0.5 mm (HR)
Standard deviation [13], [40]	Up to 10%	20 dB	No	NA	200 Hz	$< 30\ nm$
Kalman filter [44]-[46], [120]	No	60 dB (noise level)	No	Yes, pulse echo	200 Hz, 100 - 500 Hz (HM)	60 nm p-p
Least squares [52]	NA	Suppresses noise	NA	NA	Up to 1 kHz	$< 100\ \mu m$
Zero-crossing [53]	No	10 dB	Up-sampled	NA	0.010° at 10 Hz	NA
Proposed method	Yes	SNR 7 dB	$f_s = 4f_cN$	Yes	10 Hz - 2 kHz	0.35 - 1365 mm.

3.4.5.2 Noisy received signal

(i) The β estimation techniques: Kalman filter [45] approach performs well in noisy environment with a noise level of 60 dB. The zero-crossing method [53] can tolerate up to 10 dB SNR. The conventional method fails to estimate parameters and noise is amplified in phase-operation method [33]. The correlation method [119] and standard deviation [40] perform well with 20 dB SNR. The least-square technique can suppress the noise. But, the proposed method can tolerate up to SNR of 7 dB. The increase in SNR is observed after noise removal in (S_{oi}) which was found to be 17.8 dB. Moreover, the MWDFT filter removes the noise efficiently.

Table 3.7: Comparison with other techniques

Methods	Impure / Distorted S_i	Presence of noise	f_s variation	Phase shift - path length and Doppler	Frequency range	Amplitude range
PLL [48]	Yes	SNR 30 dB	Variable sampling	NA	50 Hz	NA
CPPM with synchronization [116]	Insensitive	SNR 0 dB	NA	Yes	1 - 10 Hz	0.5 - 1 V
Extended DACM algorithm [35]	Yes	High	NA	Yes	1.425 Hz	1±0.1 mm
Vector signal analyzer (VSA) [75]	NA	NA	NA	Yes, parametric	150 Hz	200 nm min.
Photoelectric method [113]	NA	NA	NA	Optical power ratio	Up to 40 kHz	3.2 μm
Radio frequency polarization [115]	NA	16 dB	NA	Electro-magnetic wave polarization	0.1 - 25 kHz	2 nm - 10 cm
Proposed method	Yes	SNR 7 dB	$f_s = 4f_cN$	Yes	10 Hz - 2 kHz	0.35 - 1365 mm.

(ii) Other techniques: The PLL [48] tolerates SNR of 30 dB, CPPM [116] and extended DACM [35] perform well for high SNR. The RF polarization [115] can perform well for SNR 16 dB.

3.4.5.3 Sensitive to sampling frequency variation

(i) The β estimation techniques: The ratio method [38], correlation method [33], standard deviation method [13], and Kalman method [44] fail to estimate β under f_s variation. The phase-operation method [33] is very much sensitive to f_s variation. In zero crossing method [53], the output of ADC is upsampled to improve the SNR. In the proposed method, sampling frequency can be fixed as $f_s = 4f_cN$.

(ii) Other techniques: Variable sampling period technique is employed in PLL technique [48] similar to the proposed method.

3.4.5.4 Modulation index estimation in the presence of various phase shifts

(i) The β estimation techniques: The received ultrasonic signal undergoes modulation due to ϕ_D, ϕ_0, and ϕ_P. In the presence of ϕ_0 and ϕ_D, the conventional [33], ratio [38], correlation [39], and Kalman filter [44] methods could determine the β. Similarly, the proposed method can estimate vibration parameters in the presence of ϕ_D and ϕ_0 and the ϕ_P is neglected.

(ii) Other techniques: The CPPM [116] and DACM [35], VSA [75] methods can determine ϕ_0 and ϕ_D. The VSA can also estimate the ϕ_P. The photoelectric method and RF polarization did not involve the Doppler effect.

3.4.5.5 Vibration frequency and amplitude range

(i) The β estimation techniques: The conventional [2], ratio [38], standard deviation [13], Kalman [44], and zero-crossing [53] methods can measure low vibration frequencies. The least-square [75] and correlation [39] methods can measure up to 1 kHz and 1.5 kHz respectively. The ratio [38], standard deviation [13], Kalman filter [46], and least-square [52] methods are suitable for small vibrations if the f_m is known. The conventional [2], phase-operation [33], and correlation [119] are suitable for large A_m. The proposed method can perform well upto the carrier variation of ±34 kHz this carrier variation can be either in A_m or in f_m. With the proposed set-up, the A_m range of 0.35 - 1365 mm and f_m of 2 kHz can be measured.

(ii) Other techniques: The PLL [48], CPPM [116], DACM [35], and VSA [75] methods can measure low vibration frequencies. The photoelectric method [113], [114] and RF polarization [115] can measure high vibration frequencies but these methods did not involve Doppler effect. The VSA and photoelectric method can measure small vibrations. The DACM, CPPM and RF polarization can measure the large vibrations.

3.4.5.6 Resources consumed / computation complexity (CC)

(i) The β estimation techniques: The proposed technique is implemented in FPGA with resource consumption of 13.34%. The zero crossing method [53] is also implemented in FPGA with 94% resources.

(ii) Other techniques: The PLL technique is implemented in FPGA with 35% resources [48]. The extended DACM can reduce the processing time by a factor of 75% [35].

3.5 Summary

The phase modulated received ultrasonic signal is demodulated by the synchronization technique which involves MWDFT. The vibration parameter estimation is achieved through the Doppler signal extraction of the received ultrasonic signal. Simulation studies confirms that the proposed synchronization technique can tolerate a maximum carrier deviation of $\pm 34\ kHz$ in terms of vibration amplitude and frequency for a 40 kHz carrier. The experimental investigation demonstrates the capability of the proposed technique in extracting the vibration parameters through Doppler signal extraction. The proposed method is validated for the maximum vibration frequency of 2 kHz and vibration amplitude range of of 0.35 - 1365 mm. The proposed method is implemented in FPGA with the resource utilization of 13.34%.

Chapter 4

MWDFT-based mono-component AM-FM signal decomposition

4.1 Introduction

When an ultrasonic carrier deviation is large ($\geq 6\ kHz$) because of the vibration frequency, the received signal appears as AM-FM signal instead of phase or frequency modulated signal. However, the vibration information is present only in frequency modulating signal. To separate the AM signal from FM signal, the MWDFT-PLL is modified in such a way that the sampling pulse generator produces sampling pulses suitable for MWDFT bin-1 and MWDFT bin-0 for the retrieval of frequency and amplitude modulation signals, respectively. Hence, this method presents how the frequency and amplitude variation of mono-component AM-FM could be retrieved simultaneously. An AM-FM signal comprising of a sinusoidal carrier signal, whose amplitude and frequency vary as instantaneous sinusoids could be identified in the various fields such as communication systems, speech processing, image processing, and vibration systems. Estimation of the information stored in instantaneous amplitude (IA) and instantaneous frequency (IF) is a demodulation problem. In general, AM-FM signals could be classified as mono-component and multi-component AM-FM signals [121]. Hilbert transform, Teager-Kaiser energy operator or energy separation algorithm, empirical mode decomposition (EMD), and phase locking schemes are some of the successful techniques for the decomposition of mono-component AM-FM signals. The first one, Hilbert transform approach involves linear integral operator, whereas the energy operator or separation algorithms employ the non-linear differential operator [122]. Second approach: amplitude and frequency demodulation techniques based on energy operators presented in [123] can track the AM envelope and estimate the instantaneous frequency of FM signals approximately. Assumptions adopted in the procedure are: AM and FM information signals have bandwidth much smaller than the carrier frequency and/or they do not vary much in value with respect to the carrier. Further, higher order differential operators had been proposed in [124] with similar assumptions mentioned in [123] for the AM-FM demodulation. Furthermore, energy demodulation method had been applied to two component AM-FM signal mixtures [125]. Energy separation algorithms are very much suitable for smaller frequency deviation about the carrier. For signals with large frequency deviation, and modulation indices of the carrier, the energy operator provides amplitude and frequency demodulation errors. Hence the generalized energy operator had been developed in [126] based on frequency transformations for signals with large deviation and modulation indices. The performance improvement in energy separation algorithm had been achieved by passing the signals through bandpass filters; this helps in capturing AM-FM information from noisy modulated signals [127]. The discrete AM-FM function demodulation had been developed using quasi-eigenfunction approximations (QEA) [128].

In addition to single component demodulation, the multi-component AM-FM demodulation problem had been solved by state space estimation techniques, linear prediction, parametric approach, techniques based on Hankel and Toeplitz matrices and energy demodulation approaches [129], [130]. An asymptotically exact approach using Hilbert transform had been proposed for speech signals in [131] .

The third approach, EMD is an adaptive demodulation technique for analyzing the mono-component and multi-component, nonlinear and non-stationary signals. Further, it models the signal as a series of intrinsic mode functions (IMFs) plus a residual signal. The mono-component and multi-component signal decomposition undergo mode-mixing problem and detection of envelope extreme points. These problems have been addressed in [132] and improvement has been ascertained comparing to the Deering and Kaisers approach. EMD could be employed as a filter bank for non-stationary signal estimation [133], and it is used to decompose the complex valued non-stationary or nonlinear time series [134].

The phase locking schemes are another class of demodulation techniques which are popular in the field of AM-FM demodulation [60], [61]. A frequency selective AM/FM demodulator based on phase locked loop is proposed using discrete components [135], in which the FM and AM demodulations can be controlled independently. A FM demodulator design using phase locked loop and its frequency response characteristics are presented in [136]. At low frequency deviations, the response exhibits linear operation, whereas for high frequency deviations the frequency response shows the non-linear behavior and the loop looses modulation tracking. A method is proposed to determine the carrier-to-noise-ratio (CNR) for FM signals based on threshold analysis of PLL demodulators [137]. For an input signal consists of frequency modulated carrier and frequency modulated interferer, a FM demodulator involving two phase locked loops is proposed to retrieve the stronger and weaker received signals in [138]. Moreover, design and synthesis procedure of all pole phase lock tracking filters facilitates PLL modeling [139]. A PLL FM modulator performance under Gaussian modulation is studied in [140], however, it could be observed that the substantial reduction in the modulation limit, beyond which PLL fails to lock, due to input bandpass filter.

The motivation behind this work is to propose a phase-locked loop based method to decompose mono-component AM-FM signal for large variation in carrier frequency and large variation in amplitude. It is noted from the literature that the existing techniques are suitable for low variation in carrier and amplitude. This chapter describes a method of mono-component AM-FM signal decomposition based on MWDFT phase locking technique. The proposed demodulation technique for AM-FM signal demodulation falls under the category of combining the feed-forward and feedback demodulation techniques. In the case of feed-forward demodulation the FM signal is converted into AM using a filter and the feedback demodulation involves phase locking schemes [103]. In this research work, the application of MWDFT based PLL has been extended to mono-component AM-FM demodulation. The proposed scheme is capable of extracting IF and IA for the signals comprising of large variation in frequency and amplitude. The wide operating range of the PLL scheme facilitates in achieving the large variation in AM-FM signal demodulation. In addition, the MWDFT incorporated in the PLL would extract the message signals in presence of noise.

4.2 Adaptive sampling frequency based MWDFT-PLL

The block diagram representation of the proposed phase locking scheme with filter structures for the decomposition of AM-FM signals is shown in Fig. 4.1. The MWDFT-PLL is designed to track the frequency modulated sinusoidal carrier; while tracking the carrier, the variation in amplitude and frequency information could be obtained from PLL. The instantaneous frequency tracking structure 1 and instantaneous amplitude tracking structure 2 are integrated into single PLL structure. The major portion, structure 1, of the adaptive scheme comprises of MWDFT filter, moving averager, proportional and integral (PI) controller and SPG. The z-domain transfer function of MWDFT filter [102] is expressed as

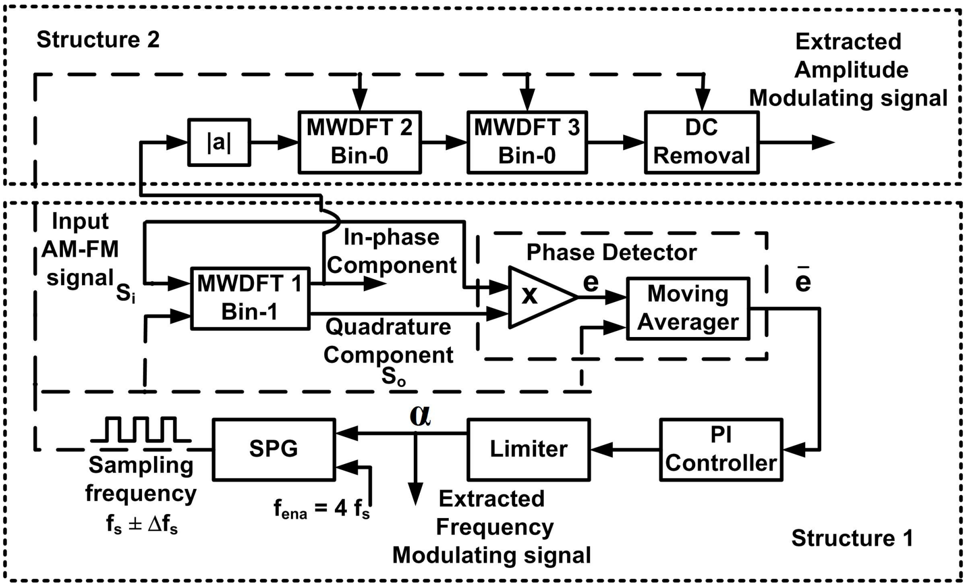

Fig. 4.1: Block diagram representation of adaptive sampling frequency based MWDFT-PLL

$$H_k(z) \quad = \quad \frac{(1-r^N z^{-N})(re^{j2\pi k/N})}{1-re^{j2\pi k/N}z^{-1}} \tag{4.1}$$

Where, k is the bin index; N is the window length; r is the damping factor. The in-phase and quadrature component z-domain transfer functions could be found in [103]. The moving averager transfer function [141] can be expressed in z-domain as

$$H_{MA}(z) \quad = \quad \left(\frac{1}{N}\right)\left[\frac{1-r^N z^{-N}}{1-rz^{-1}}\right] \tag{4.2}$$

The PI controller transfer function is written as

$$H_{PI}(z) \quad = \quad K_P + \frac{K_I}{1 - z^{-1}} \tag{4.3}$$

where K_P and K_I are the proportional and integral gains respectively. The difference equation of SPG [142]:

$$\begin{bmatrix} x_1(k+1) \\ x_2(k+1) \end{bmatrix} = \begin{bmatrix} \alpha & \alpha - 1 \\ \alpha + 1 & \alpha \end{bmatrix} \begin{bmatrix} x_1(k) \\ x_2(k) \end{bmatrix} \quad x_1(0) = 1; \;\; x_2(0) = 0. \tag{4.4}$$

Where, α is the control signal, which is fed to SPG by the PI controller.

The second portion, structure 2 in Fig. 4.1, consists of MWDFT and DC removal filters is supplemented to the MWDFT PLL especially to retrieve the amplitude modulated signal. The z-domain transfer function of MWDFT bin-0 [141] is written as

$$H_0(z) = \left(\frac{1}{N}\right) \left[\frac{1 - r^N z^{-N}}{1 - rz^{-1}}\right] \quad r = 0.9998 \tag{4.5}$$

The z-domain transfer function of DC removal filter [141] is

$$H_{DC}(z) = \frac{1 - z^{-1}}{1 - az^{-1}} \quad a = 0.9998 \tag{4.6}$$

Transfer function model of structure 2 is a cascaded connection of MWDFT bin-0 and DC removal filter that could be expressed as

$$H_{structure2}(z) = \left(\frac{1}{N^2}\right) \left[\frac{1 - r^N z^{-N}}{1 - rz^{-1}}\right]^2 \left[\frac{1 - z^{-1}}{1 - az^{-1}}\right] \tag{4.7}$$

Bode diagrams of MWDFT bin-0 and MWDFT bin-1 are depicted in Fig. 4.2. The magnitude plot shows the carrier or fundamental frequency for the MWDFT bin-1 is chosen as 40 kHz. The fundamental bin allows the carrier frequency to vary ideally from 0 to 80 kHz and the spectrum shows the maximum amplitude could be obtained at 40 kHz. At maximum amplitude, the phase shift offered by MWDFT bin is zero and it could be observed form Fig. 4.2. The phase shift varies from 270° to -180° and the magnitude varies from -50 to -150 dB; the maximum amplitude occurs at 40 kHz, which is 0 dB.

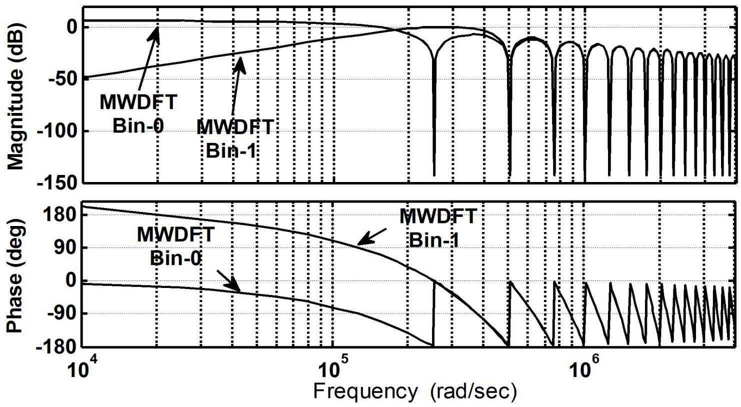

Fig. 4.2: MWDFT magnitude and phase plots for the 40 kHz FM carrier

At 80 kHz MWDFT shows the sharp rejection. Bode diagrams of MWDFT bin-0 is superimposed with MWDFT bin-1 plots. MWDFT bin-0 exhibits the sharp rejection at 40 kHz frequency. MWDFT bin-0 passes the frequencies from 0 to 40 kHz, attenuation in magnitude increases as the frequency moves away from d.c. and it exhibits almost flat response at low frequencies. This characteristics of flat response is utilized to extract the AM by suppling the same sampling frequency for both the MWDFT bin-1 and MWDFT bin-0. The overlapping characteristics of MWDFT bin-1 and bin-0 facilitate the extraction of large variation in AM frequency.

4.2.1 Instantaneous frequency tracking

The input AM-FM signal is fed to the MWDFT filter bin-1, in which the harmonic bin number k is set to 1, to extract the FM carrier that is considered as the fundamental frequency. The MWDFT-PLL scheme employs the principle of adaptive sampling frequency control. In the process of instantaneous frequency tracking, the AM-FM input signal is fed to the MWDFT filter which can produce in-phase and quadrature components. Since the MWDFT is tuned to center frequency of the FM carrier (f_c), the output signals, in-phase and quadrature components are produced at the frequency of the FM carrier. However, frequency modulation at the input causes the center frequency of the carrier to drift. Consequently, the drift in center frequency introduces magnitude and phase errors in the output of MWDFT in-phase and quadrature components. In particular, the magnitude error due to sinusoidal frequency variation at the input is reflected as amplitude modulation at the output of MWDFT in-phase and quadrature components. Hence MWDFT is a filter that converts FM into AM, the resultant signals from MWDFT turn out to be AM signal with phase error. Thus it can be stated that the sinusoidal drift in carrier frequency is reflected as an AM signal in the MWDFT output. But the input signal is already modulated by sinusoidal AM. As a result, the envelopes of the MWDFT in-phase and quadrature components contains two AM frequencies, one due to the FM at the input signal and another caused by AM at the input.

The simple multiplier present in the Fig. 4.1 acts as a phase detector, which correlates the input AM-FM signal (S_i) and the quadrature component (S_0) of the MWDFT and produces an error signal $e(n)$. The moving averager provides an average of $e(n)$, and the averaged error signal is further supplied to PI controller for control action. The control signal $\alpha(n)$ is fed to the SPG for producing the sampling pulses ($f_s = f_s + \Delta f_s$) as shown in Fig. 4.1. SPG sampling pulses are supplied to MWDFT bin-1 to track the FM carrier. The frequency of the carrier is varied sinusoidally and hence the sampling pulses supplied to the MWDFT is also forced to vary accordingly in the PLL locking operation. So $\alpha(n)$ produces a signal which is the modulation frequency of FM at the input AM-FM signal. Thus the instantaneous frequency of AM-FM mono-component signal could be extracted using the adaptive sampling frequency based MWDFT-PLL. The frequency modulation index $\beta = \Delta f_c / f_{m2}$ where, Δf_c is the variation in carrier frequency; f_{m2} is the frequency of the FM signal. The MWDFT-PLL scheme is designed to extract both FM and AM signals with large frequency variation. Amplitude of extracted signal reflects the depth of frequency modulation index β.

4.2.2 Instantaneous amplitude tracking

The phase locked AM-FM signal from the MWDFT bin-1 in-phase component possesses the information of amplitude modulated signal. The sinusoidal amplitude variation is as such reflected in the phase locked MWDFT output. Further, to retrieve the AM signal, the in-phase component of MWDFT is passed through the full-wave rectifier. The resultant rectified signal is fed to MWDFT bin-0 block, which is enabled by the same sampling frequency of FM carrier, to extract the modulation signal of AM. Two MWDFT bin-0 blocks have been employed to smoothen the extraction. Furthermore, the extracted AM is passed to the DC removal block to eliminate the dc component present in the extracted amplitude modulation signal. The entire process of extraction of amplitude modulation signal is shown in Fig. 4.1 as structure 2. Advantages of the extended scheme could be described as follows:

(i) The sampling frequency produced by the SPG is used to extract AM using MWDFT bin-0 filter. Hence the wide variation in AM frequency could be extracted using the proposed phase locking scheme.

(ii) The proposed scheme is applicable to extract the large variation in frequency and amplitude modulation signals simultaneously.

The depth of both AM and FM could be varied and tracked using adaptive sampling frequency control. The amplitude modulation index $M_1 = \frac{E_{max}-E_{min}}{E_{max}+E_{min}}$ where, M_1 is the amplitude modulation index; E_{max} and E_{min} are the maximum and minimum values of the envelope obtained from MWDFT in-phase component. Wide variation in instantaneous amplitude and phase tracking had been achieved by utilizing the sampling pulses produced from the SPG as shown in Fig. 4.1. The sampling pulses, which facilitates the locking of FM carrier are utilized to enable the MWDFT bin-0 for extracting the instantaneous amplitude as well. Similar to FM extraction, amplitude of the extracted AM increases with increase in AM modulation index M_1 or depth.

4.2.3 Linearized model of MWDFT-PLL for AM-FM model

Linearized transfer function model of the MWDFT-PLL structure 1 are presented in [102], [143]. This model is reproduced in Fig. 4.3. The MWDFT Bin-1 block was subjected to

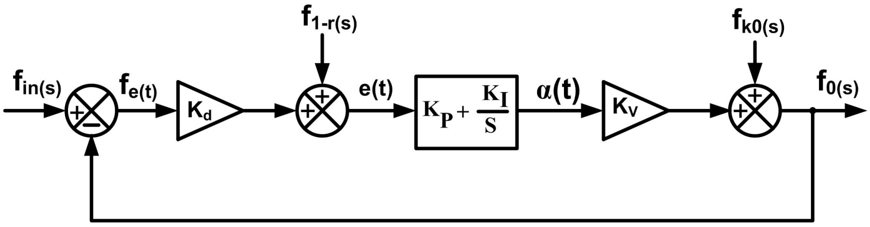

Fig. 4.3: Linear model of MWDFT-PLL structure 1

an input of varying frequency with fixed sampling frequency. The phase error curve was obtained for various frequency. The phase error slope K_d was determined from the curve. Further, the SPG gain was determined from its characteristics. Since these procedures involve linear fitting, the model is shown in s domain in Fig. 4.3. The z-domain transfer function of structure 1 can be represented as

$$\begin{aligned}
F_0(z) &= \frac{[K_1/(1+K_1)] - \left[((1+K_1)e^{-(K_2/(1+K_1))T_s} - 1)/(1+K_1)\right] z^{-1}}{1 - e^{-(K_2/(1+K_1))T_s} z^{-1}} \quad F_{in}(z) \\
&+ \frac{[1/(1+K_1)]\,(1-z^{-1})}{1 - e^{-(K_2/(1+K_1))T_s} z^{-1}} \quad F_{k0}(z) + \frac{\left[\frac{K_4(1+K_1)+K_2^2K_3-K_2K_4(1+K_1)}{(K_2/(1+K_1))}\right]}{1 - e^{-(K_2/(1+K_1))T_s} z^{-1}} \quad F_{1-r}(z) \\
&- \frac{\left[\frac{\left[K_4(1+K_1)e^{-(K_2/(1+K_1))T_s}+K_2^2K_3-K_2K_4(1+K_1)\right]z^{-1}}{(K_2/(1+K_1))}\right]}{1 - e^{-(K_2/(1+K_1))T_s} z^{-1}} \quad F_{1-r}(z) \qquad (4.8)
\end{aligned}$$

where $K_1 = K_dK_PK_V$, $K_2 = K_dK_VK_I$, $K_3 = K_PK_V$, $K_4 = K_VK_I$, T_s is the sampling period, and K_V is SPG gain [139]. It can be concluded that the closed loop transfer function of MWDFT PLL is a type 0 and order 1 system with respect to the frequency input.

4.3 Analysis of AM-FM frequency extraction

4.3.1 Mono-component AM-FM signal model

The mono-component AM-FM signal consists of the sinusoidal modulation in amplitude and frequency had been considered for the analysis. The MWDFT input signal:

$$S_i(t) = (1 + M_1 \sin\omega_{m1}t)(\sin(\omega_c t + \beta\sin\omega_{m2}t)) \qquad (4.9)$$

Where, M_1 is the AM modulation index; β is the frequency modulation index; ω_{m1} is the angular frequency of AM message signal; ω_{m2} is the angular frequency of FM message signal; ω_c is the FM carrier signal. Equation (4.9) can be expanded as

$$S_i(t) = (1 + M_1 \sin\omega_{m1}t)((\sin\omega_c t\cos(\beta\sin\omega_{m2}t)) + (\cos\omega_c t\sin(\beta\sin\omega_{m2}t))) \qquad (4.10)$$

From [144],

$$\begin{aligned}
\cos(\beta\sin\omega_{m2}t) &= J_0(\beta)+2J_2(\beta)\cos 2\omega_{m2}t+......+2J_{2n}(\beta)\cos(2n)\omega_{m2}t+....\\
\sin(\beta\sin\omega_{m2}t) &= 2J_1(\beta)\sin\omega_{m2}t+2J_3(\beta)\sin 3\omega_{m2}t+...\\
&+ 2J_{2n-1}(\beta)\sin(2n-1)\omega_{m2}t+... \qquad (4.11)
\end{aligned}$$

Therefore, Bessel function expansion of input AM-FM signal can be expressed as,

$$S_i(t)=(1+M_1\sin(\omega_{m1}t))\sum_{n=-\infty}^{+\infty}J_n(\beta)\sin(\omega_c t+n\omega_{m2}t) \qquad (4.12)$$

Where, J_n is the n^{th} order cylindrical Bessel function of the first kind. Expanding the (4.12) for $n = 0, 1, 2, 3$.

$$\begin{aligned}
S_i(t) &= (1+M_1\sin(\omega_{m1}t))[J_0(\beta)\sin(\omega_c t)+J_1(\beta)[\sin(\omega_c+\omega_{m2})t-\sin(\omega_c-\omega_{m2})t]\\
&+ J_2(\beta)[\sin(\omega_c+2\ \omega_{m2})t+\sin(\omega_c-2\ \omega_{m2})t]\\
&+ J_3(\beta)[\sin(\omega_c+3\ \omega_{m2})t-\sin(\omega_c-3\ \omega_{m2})t]+.........] \qquad (4.13)
\end{aligned}$$

Further expansion of (4.13) yields the following spectral components

$$\begin{aligned}
S_i(t) &\cong J_0(\beta)\sin(\omega_c t)+J_1(\beta)[\sin(\omega_c+\omega_{m2})t-\sin(\omega_c-\omega_{m2})t]\\
&+ J_2(\beta)[\sin(\omega_c+2\ \omega_{m2})t+\sin(\omega_c-2\ \omega_{m2})t]\\
&+ J_3(\beta)[\sin(\omega_c+3\ \omega_{m2})t-\sin(\omega_c-3\ \omega_{m2})t]\\
&- J_0(\beta)M_1[\cos(\omega_c+\omega_{m1})t-\cos(\omega_c-\omega_{m1})t]\\
&+ J_1(\beta)M_1[-\cos(\omega_c+\omega_{m1}+\omega_{m2})t-\cos(\omega_c+\omega_{m2}-\omega_{m1})t\\
&+ \cos(\omega_c-\omega_{m2}+\omega_{m1})t-\cos(\omega_c-\omega_{m2}-\omega_{m1})t]\\
&+ J_2(\beta)M_1[-(\cos(\omega_c+\omega_{m1}+2\ \omega_{m2})t-\cos(\omega_c+2\ \omega_{m2}-\omega_{m1})t)\\
&+ (-(\cos(\omega_c-2\ \omega_{m2}+\omega_{m1})t-\cos(\omega_c-2\ \omega_{m2}-\omega_{m1})t))]\\
&+ J_3(\beta)M_1[-(\cos(\omega_c+3\ \omega_{m2}+2\ \omega_{m1})t-\cos(\omega_c+3\ \omega_{m2}-\omega_{m1})t)\\
&+ (\cos(\omega_c-3\ \omega_{m2}+\omega_{m1})t-\cos(\omega_c-3\ \omega_{m2}-\omega_{m1})t)] \qquad (4.14)
\end{aligned}$$

MWDFT quadrature component signal model could be expressed as

$$S_{O\ quad}(t) \cong -(\cos(\omega_c t)(1 + M_1 \sin(\omega_{m1} t))(1 - M_2 \cos(\omega_{m2} t))) \tag{4.15}$$

Where, M_2 is the modulation index of the FM signal converted into AM by MWDFT filter.

Further expansion of (4.15) yields the following spectral components in MWDFT quadrature component,

$$\begin{aligned} S_{O\ quad}(t) \cong & -\cos(\omega_c t) - \frac{M_1}{2}[\sin(\omega_c + \omega_{m1})t - \sin(\omega_c - \omega_{m1})t] \\ + & \frac{M_2}{2}[\cos(\omega_c + \omega_{m2})t - \cos(\omega_c - \omega_{m2})t] \\ + & \frac{M_1 M_2}{2}[\sin(\omega_c + \omega_{m1} + \omega_{m2})t - \sin(\omega_c - \omega_{m1} - \omega_{m2})t] \\ - & \frac{M_1 M_2}{2}[\sin(\omega_c + \omega_{m1} - \omega_{m2})t - \sin(\omega_c - \omega_{m1} + \omega_{m2})t] \end{aligned} \tag{4.16}$$

The phase detector correlates the spectral contents of (4.14) and (4.16) and the moving averager output could be represented by the following spectral components,

$$\begin{aligned} \overline{e(t)} \cong & J_1(\beta) M_1 M_2 \cos(\omega_{m1})t + J_1(\beta) M_1^2 M_2 \sin(2\ \omega_{m1})t - J_1(\beta) M_1^2 \sin(\omega_{m2})t \\ + & J_1(\beta)\frac{M_2}{2}\sin(2\ \omega_{m2})t + J_1(\beta)\frac{3M_1}{2}\cos(\omega_{m1} + \omega_{m2})t \\ - & J_1(\beta)\frac{3M_1}{2}\cos(\omega_{m1} - \omega_{m2})t - J_1(\beta)\frac{M_1^2}{2}\sin(2\ \omega_{m1} - \omega_{m2})t \\ + & J_1(\beta)\frac{M_1^2}{2}\sin(2\ \omega_{m1} + \omega_{m2})t + J_1(\beta)\frac{M_1 M_2}{4}\cos(2\ \omega_{m2} - \omega_{m1})t \\ - & J_1(\beta)\frac{3M_1 M_2}{4}\cos(2\ \omega_{m2} + \omega_{m1})t - J_1(\beta)\frac{M_1^2 M_2}{2}\sin(2\ \omega_{m1} + 2\ \omega_{m2})t \\ - & J_1(\beta)\frac{M_1^2 M_2}{4}\sin(2\ \omega_{m1} - 2\ \omega_{m2})t \end{aligned} \tag{4.17}$$

Substituting $J_1(\beta) \cong \beta/2$ for small values of modulation index in (4.17),

$$
\begin{aligned}
\overline{e(t)} &\cong (\beta/2)M_1M_2\cos(\omega_{m1})t + (\beta/2)M_1^2M_2\sin(2\ \omega_{m1})t - (\beta/2)M_1^2\sin(\omega_{m2})t \\
&+ (\beta/2)\frac{M_2}{2}\sin(2\ \omega_{m2})t + (\beta/2)\frac{3M_1}{2}\cos(\omega_{m1}+\omega_{m2})t \\
&- (\beta/2)\frac{3M_1}{2}\cos(\omega_{m1}-\omega_{m2})t - (\beta/2)\frac{M_1^2}{2}\sin(2\ \omega_{m1}-\omega_{m2})t \\
&+ (\beta/2)\frac{M_1^2}{2}\sin(2\ \omega_{m1}+\omega_{m2})t + (\beta/2)\frac{M_1M_2}{4}\cos(2\ \omega_{m2}-\omega_{m1})t \\
&- (\beta/2)\frac{3M_1M_2}{4}\cos(2\ \omega_{m2}+\omega_{m1})t - (\beta/2)\frac{M_1^2M_2}{2}\sin(2\ \omega_{m1}+2\ \omega_{m2})t \\
&- (\beta/2)\frac{M_1^2M_2}{4}\sin(2\ \omega_{m1}-2\ \omega_{m2})t
\end{aligned}
\tag{4.18}
$$

The spectral components present in the moving averager output are shown in Fig. 4.4. The spectral components for case (i) $\omega_{m2} > \omega_{m1}$, case (ii) $\omega_{m2} < \omega_{m1}$ and case (iii) $\omega_{m2} = \omega_{m1}$ are shown in Fig. 4.4(a), 4.4(b) and 4.4(c) respectively. The PI controller parameters, K_P and K_I must be tuned to extract only the ω_{m2} component by filtering out all other spectral components present in the moving averager output. The PI controller bandwidth should be chosen in such a way that ω_{m2} component should be allowed through PI.

4.4 Simulation results and discussion

The performance of MWDFT phase locking scheme is tested for retrieval of frequency and amplitude modulation signals simultaneously. A 40 kHz sinusoidal carrier is modulated by a 1 kHz sinusoidal signal and the amplitude variation is chosen as 1 kHz sinusoidal signal. The frequency modulation index is chosen to be 5 and the amplitude modulation index is 0.25. Through extensive simulation, the following test cases have been developed to decompose the synthetic mono-component AM-FM signal,

(i) Demodulation of FM and AM for a fixed carrier frequency

(ii) Step change in carrier and FM frequencies for a fixed AM frequency

(iii) Step change in carrier and AM frequencies for a fixed FM frequency

(iv) Sudden change in AM frequency for fixed carrier and FM frequencies

(v) Sudden change in FM frequency for fixed carrier and AM frequencies

(vi) Instantaneous frequency and amplitude extraction on synthetic speech signal

For case (i), Fig. 4.5(a) shows the extracted instantaneous frequency and amplitude

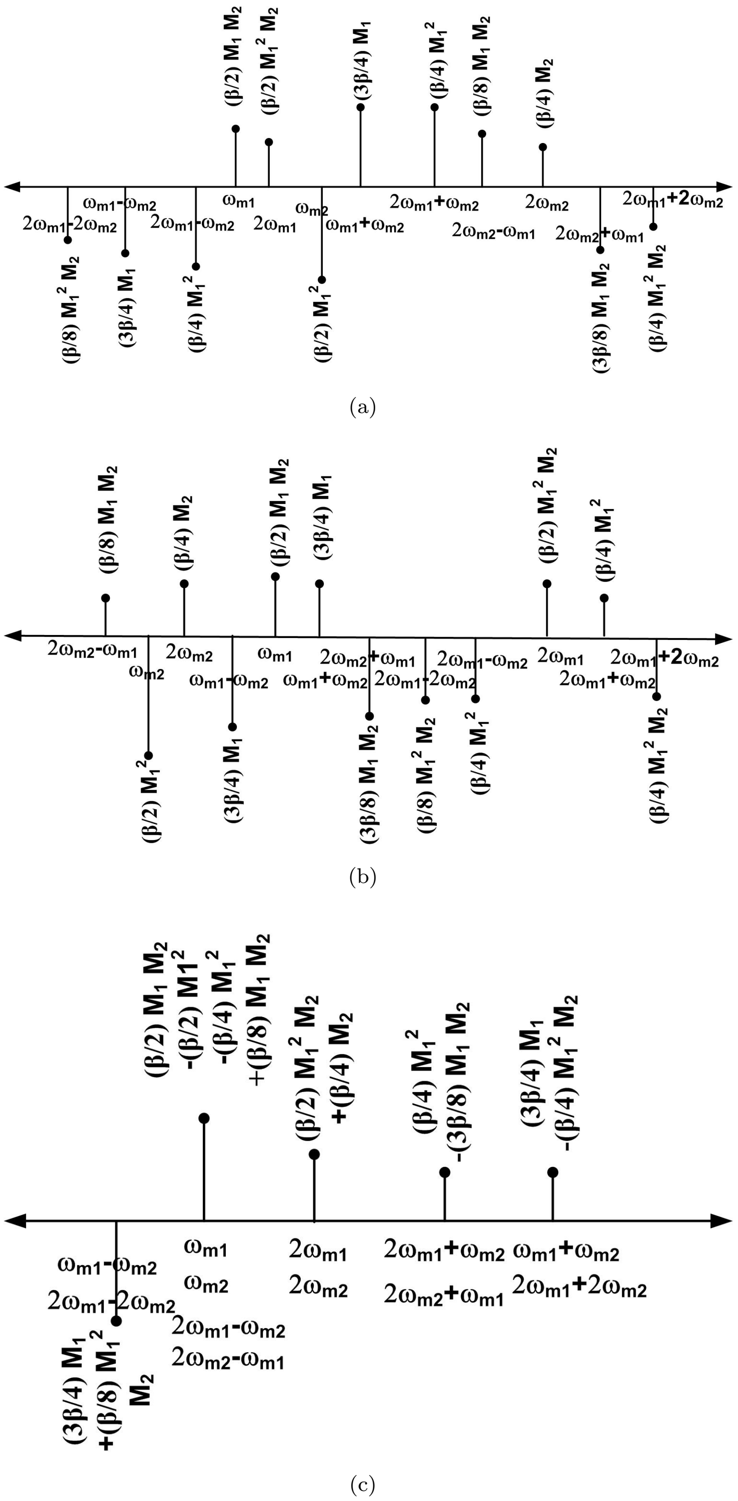

Fig. 4.4: Spectral components present in moving averager output for (a) $\omega_{m2} > \omega_{m1}$, (b) $\omega_{m2} < \omega_{m1}$, (c) $\omega_{m2} = \omega_{m1}$

variation for a carrier frequency of 40 kHz; $\beta = 5$; M_1= 0.25. The retrieved instantaneous frequency is 1 kHz and instantaneous amplitude without removing the dc is shown in Fig. 4.5(a).

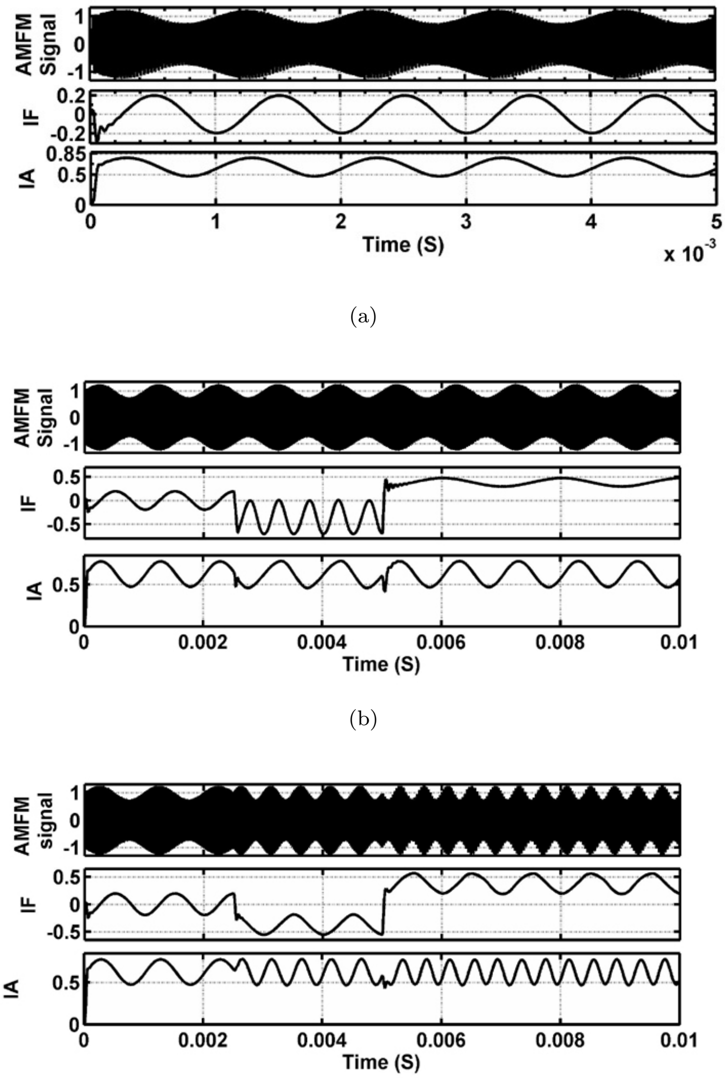

(a)

(b)

(c)

Fig. 4.5: (a) AM-FM demodulation for 40 kHz carrier frequency, 1 kHz FM, 1 kHz AM, $\beta = 5$, and $M_1 = 0.25$, (b) Effect of sudden change in carrier and FM for a fixed AM (c) Effect of sudden change in carrier and AM for a fixed FM (Simulation)

Case (ii), the effect of step change in carrier frequency and frequency modulating signal on instantaneous amplitude is depicted in Fig. 4.5(b). The carrier frequency is changed from 40 kHz to 50 kHz and frequency of the modulation signal is changed from 1 kHz to 2 kHz at t = 0.0025 s. Similarly, at t = 0.005 s carrier frequency is changed from 50 kHz to 30 kHz, and frequency modulation signal is changed from 2 kHz to 500 Hz. The sudden changes in carrier and frequency of FM could be seen from Fig. 4.5(b). Further, this effect introduces a spike in the retrieved AM signal at the step changing instant.

Case (iii), the effect of step change in carrier and amplitude modulation signals on instantaneous frequency extraction is depicted in Fig. 4.5(c). At t = 0.0025 s, the carrier is changed from 40 kHz to 50 kHz, and amplitude modulation signal is changed from 1 kHz to 2 kHz. At 0.005 s the carrier is changed to 50 kHz to 30 kHz and the amplitude modulation is changed to 2.5 kHz. The PLL performance under these conditions could be observed from Fig. 4.5(c). Furthermore, the effect of sudden change in frequency modulation signal has been studied.

Case (iv), at t = 0.0025 s the frequency of modulation signal is changed from 1 kHz to 2 kHz with $\beta = 5$; subsequently at t = 0.005 s the modulation signal is removed, the frequency of the modulation signal is zero, or d.c. The PLL acquires quick locking for the step change in FM that could be observed from Fig. 4.6(a). The effect of step change in amplitude modulating signal on instantaneous frequency is shown in Fig. 4.6(b). At t = 0.0025 s the amplitude modulation frequency is changed from 1 kHz to 2 kHz; and at t = 0.005 s the amplitude modulation is removed; the fundamental carrier is maintained at 40 kHz and frequency of the modulation signal 1 kHz. Fig. 4.6(a) and Fig. 4.6(b) depict the step change in frequency and amplitude modulating signals. At t = 0.0025 s modulating signals change from 1 kHz to 2 kHz; at t = 0.005 s modulating signals change from 2 kHz to d.c, without any variation in carrier signal.

The pull-in-range is obtained by conducting suitable tests on the MWDFT-PLL for a maximum step change in carrier frequency for positive and negative directions for which PLL can establish a lock with and without AM and FM. Since the pull-in range decides the maximum variation in FM frequency could be extracted by the PLL, the performance analysis had been carried out based on the pull-in-ranges obtain under variation in FM, AM, and modulation indices. To begin with, the unmodulated carrier frequency has been chosen as 40 kHz, and the sudden change in maximum carrier frequency, both in positive and negative directions is applied in order to determine the pull-in-range of the PLL which was found to be 29 $kHz \leftrightarrow 69$ kHz. Table 4.1 provides the pull-in ranges under various operating conditions of the PLL with the PI settings of $K_P = 0.01$ and $K_I = 0.02$, and center frequency of 40 kHz. For a frequency modulated input signal, increase in

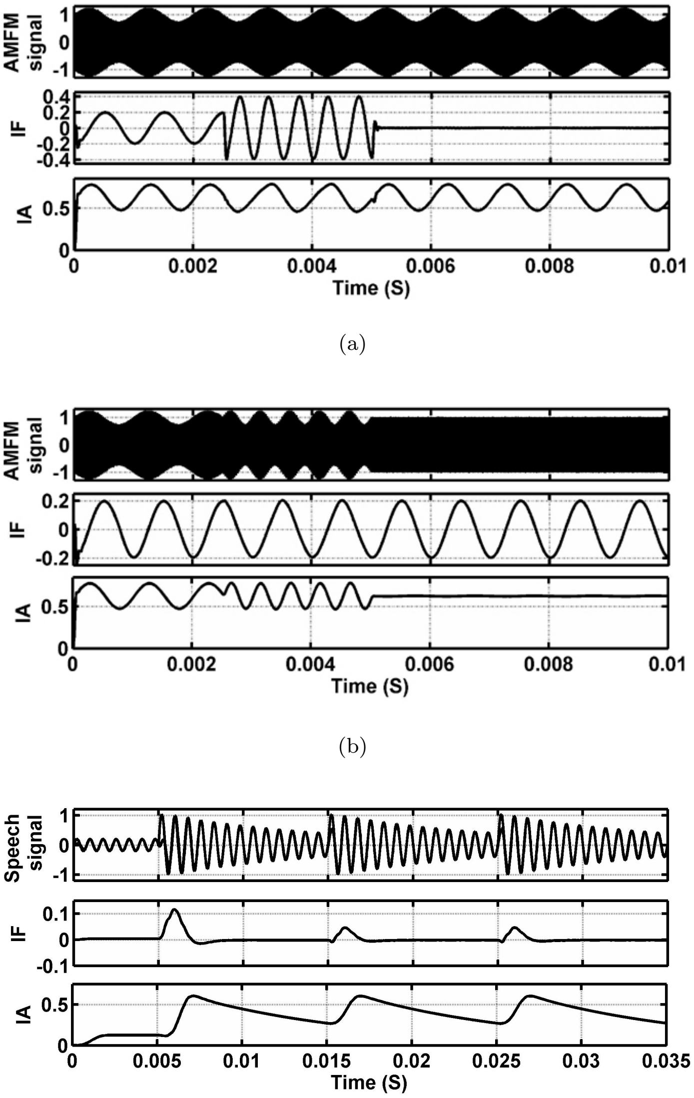

(a)

(b)

(c)

Fig. 4.6: (a) Effect of sudden change in FM on AM (b) Effect of sudden change in AM on FM (c) Speech demodulation; single formant at 1300 Hz, pitch frequency at 100 Hz (Simulation)

modulation, results in slight reduction in pull-in-range of the PLL. Similarly for AM-FM input signal, increase in modulation indices decreases the pull-in-range of the PLL. In addition, it is observed form the test results that increase in amplitude modulation index shifts the pull-in-range. Moreover, the locking time of the PLL for 40 kHz to 69 kHz was found to be 0.1 ms; likewise for 40 kHz to 29 kHz, lock time was found to be 0.2 ms. The decrease in $K_P = 0.001$ and $K_I = 0.002$, increases the pull-in-range as well as the lock time. The acquisition behavior depends on the PI settings. The PI

Table 4.1: Pull-in-range of MWDFT PLL for a carrier frequency of 40 kHz; sampling frequency 20.48 kHz; $K_p = 0.01$;$K_I = 0.02$

S.No.	AM frequency (f_{m1}) Hz	FM frequency (f_{m2}) Hz	FM Modulation Index (β)	AM Modulation Index (M_1)	Pull-in-range (kHz)
1.	-	-	-	-	$29 \longleftrightarrow 69$
2.	-	2000	5	-	$29 \longleftrightarrow 63$
3.	-	2000	10	-	$35 \longleftrightarrow 55$
4.	1000	-	-	0.25	$29 \longleftrightarrow 66$
5.	1000	1000	1	0.25	$30 \longleftrightarrow 65$
6.	1000	1000	5	0.25	$30 \longleftrightarrow 65$
7.	1000	1000	10	0.25	$33 \longleftrightarrow 62$

Table 4.2: AM-FM frequency ranges with the PI settings; $\beta = 5$; $M_1 = 0.25$

S.No.	AM Frequency (f_{m1}) Hz	FM Frequency (f_{m2}) Hz	PI Controller Settings	
			K_p	K_I
1.	100	100	0.001	0.002
2.	100	1000	0.01	0.01
3.	500	1000	0.01	0.015
4.	1000	1000	0.01	0.015
5.	2000	1000	0.01	0.015
6.	1000	2000	0.01	0.02
7.	2000	2000	0.01	0.02

settings for various AM and FM frequencies with modulation indices are listed in Table 4.2. Furthermore, a synthetic speech signal with a single formant at 1300 Hz and pitch frequency at 100 Hz had been generated to test the efficacy of the proposed algorithm. Extracted instantaneous change in frequency and corresponding amplitude variation at 0.005 s, 0.015 s, and 0.025 s could be observed from Fig. 4.6(c). The PI controller settings can be adjusted to avoid the delay in the response. The extracted information is smoother than the results proposed in [122]. Hence, the proposed algorithm can be applied to extract the instantaneous frequency and amplitude of a speech signal.

4.4.1 Comparison with existing techniques

The proposed method is compared with existing techniques such as Energy operation separation algorithm (EOSA), Smoothed energy operation separation algorithm (SEOSA), Long Hilbert transform separation algorithm (LHTSA), and Short Hilbert transform separation algorithm (SHTSA). For comparison, The ratio R of carrier frequency (f_c) to information signal bandwidth f_{m1} or f_{m2} are varied as R=10,100,200. The f_c is chosen as 2 kHz and f_{m1} or f_{m2} is chosen as 2 Hz, 20 Hz, and 200 Hz. The number of samples per cycle of the carrier was chosen as 10. The K_P and K_I values are chosen for reduced steady state error. Case (i) For a $f_{m1} = f_{m2} = 2$ Hz, the β is varied from 20 to 200 in steps of 20 for $R = 1000$. The error is calculated for various M_1 which is varying from 0.05 to 0.5 in steps of 0.05. The mean absolute error percentage (MAEP) was found to be 0.15 %.

Similarly, case(ii) for the ratio of R=100, the $f_{m1} = f_{m2}$ =20 Hz, the β is varied from 2 to 20 in steps of 2. The error is calculated for various M_1 which is varying from 0.05 to 0.5 in steps of 0.05. The MAEP was found to be 0.31 %.

Case (iii) for ratio of $R = 10$, the $f_{m1} = f_{m2} = 200$ Hz, the β is varied from 0.2 to 2 in steps of 0.2, and the error is calculated for various M_1 which is varying from 0.05 to 0.5 in steps of 0.05. The MAEP was found to be 0.77 %.

Case (iv) similar to case(i) conditions had been considered for amplitude extraction, the MAEP was found to be 1.24%.

Case(v) has been carried out by applying case (ii) conditions for amplitude extraction, the MAEP was determined as 1.52%.

Case (vi) with the conditions of case(iii) the MAEP was determined as 3.78%. The MAEP can be further reduced by choosing the more number of samples per cycle of the carrier. The proposed method could offer comparable error with other methods.

4.4.2 Discussion on entropy

The Shannon entropy was calculated for the extracted FM and AM signals. The extracted message signals were stored for samples of 102400. The AM modulation index M_1 is varied as 0.1 to 0.5 for the β values of 1, 5, 10, 15, 20. The Shannon entropy was calculated for FM. The value of entropy increases with an increase in β. The variation in entropy value is less when the M_1 is 0.1. As M_1 increases the variation in entropy is slightly higher. For larger values of β and M_1, the distortion is more. It can be concluded that for M_1 between 0.1 and 0.5 the β should be within 10. Similarly the Shannon entropy was calculated for extracted AM signal. It was observed that the entropy value is minimum for larger values of $M_1 = 0.5$ and $\beta = 20$.

4.5 Experimental results

The MWDFT-PLL performance is validated through experimental tests. The proposed scheme has been designed using Altera DSP builder blocks in MATLAB/Simulink environment Fig. 4.7 and Fig. 4.8. VHDL codes were generated for the entire scheme, and the codes were downloaded into a Stratix III FPGA. A synthetic mono-component AM-FM signal is generated which can be expressed as

$$S_i(t) = (1 + 0.25 \sin(2\pi 8000t)(\sin(2\pi 32000t + 1.25 \sin(2\pi 8000t)) \tag{4.19}$$

A high speed mezzanine card (HSMC) containing two 14-bit digital-to-analog converters (DAC) has been used with an stratix III field programmable gate array (FPGA) board to observe the outputs. Fig. 4.9(a) shows the AM-FM input signal to the PLL which is given in (4.17) and the extracted FM message signal of 8 kHz. The extracted AM of 8 kHz from the AM-FM is shown in Fig. 4.9(b). A AM-FM signal with a carrier frequency of 32 kHz with 128 samples per cycle and AM, FM frequencies of 8 kHz was generated. A 50 MHz FPGA board clock is utilized for performing experimental investigation. Since SPG requires its enabling frequency should be four times of the sampling frequency required by the MWDFT block, it was enabled at 16.384 MHz.

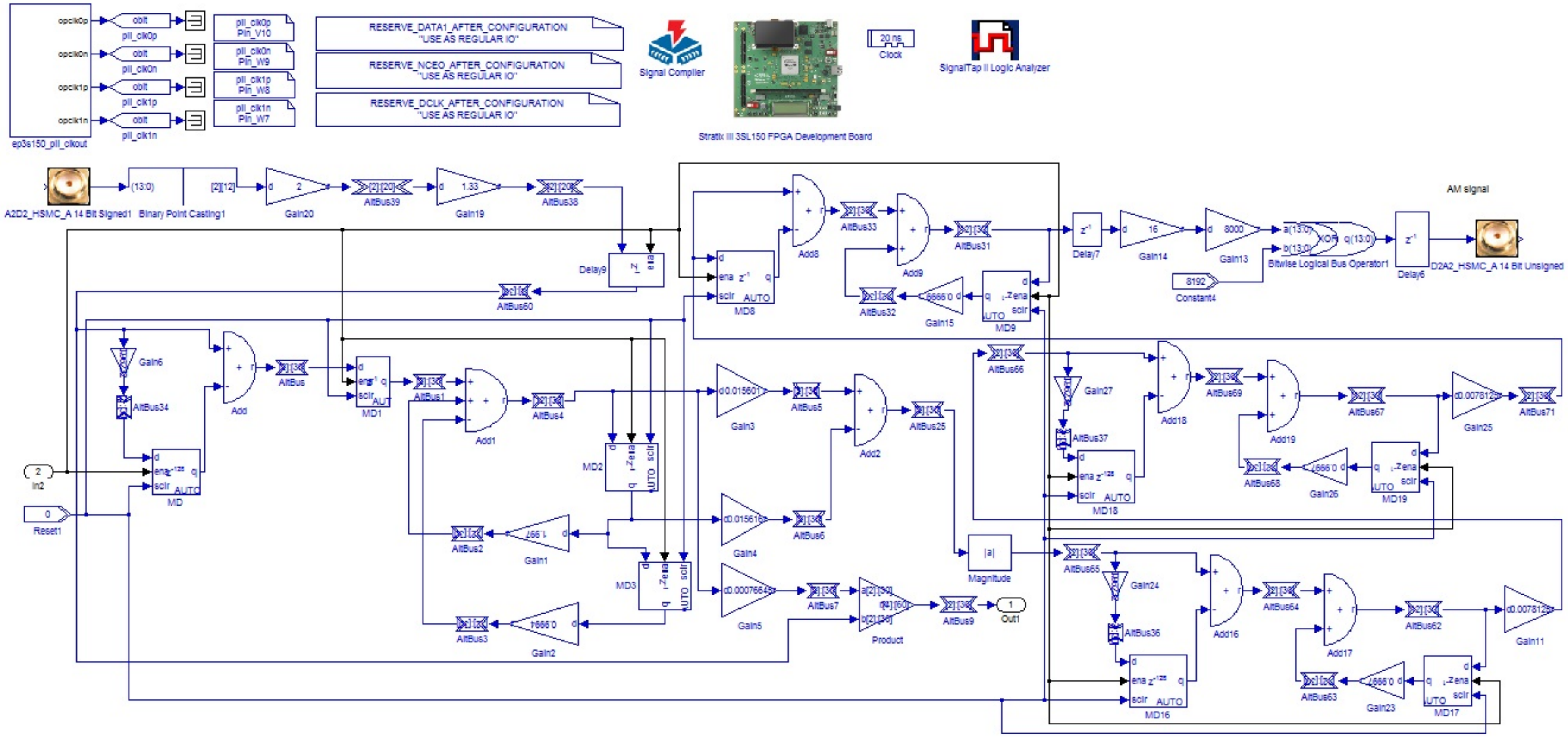

Fig. 4.7: Implementation of MWDFT-PLL for AM-FM frequency extraction (MWDFT 1 and Structure 2)

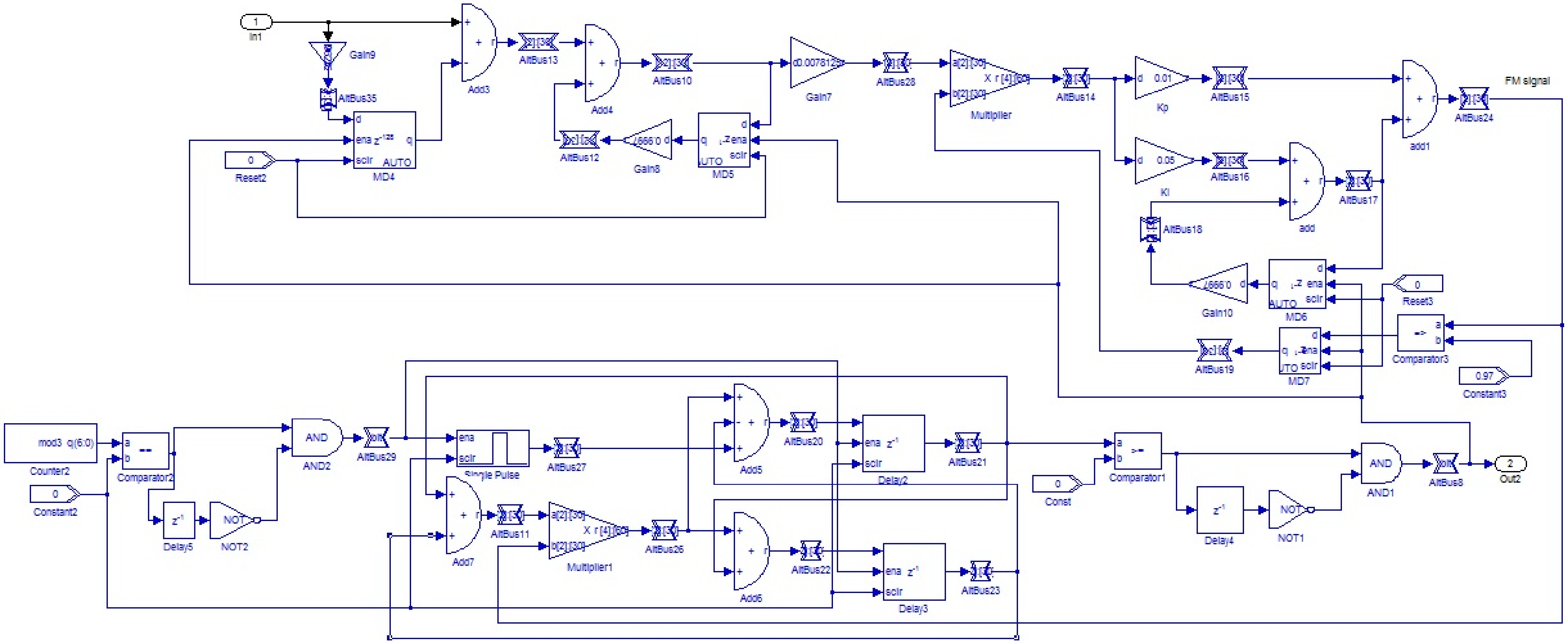

Fig. 4.8: Implementation of MWDFT-PLL for AM-FM frequency extraction (Structure 1)

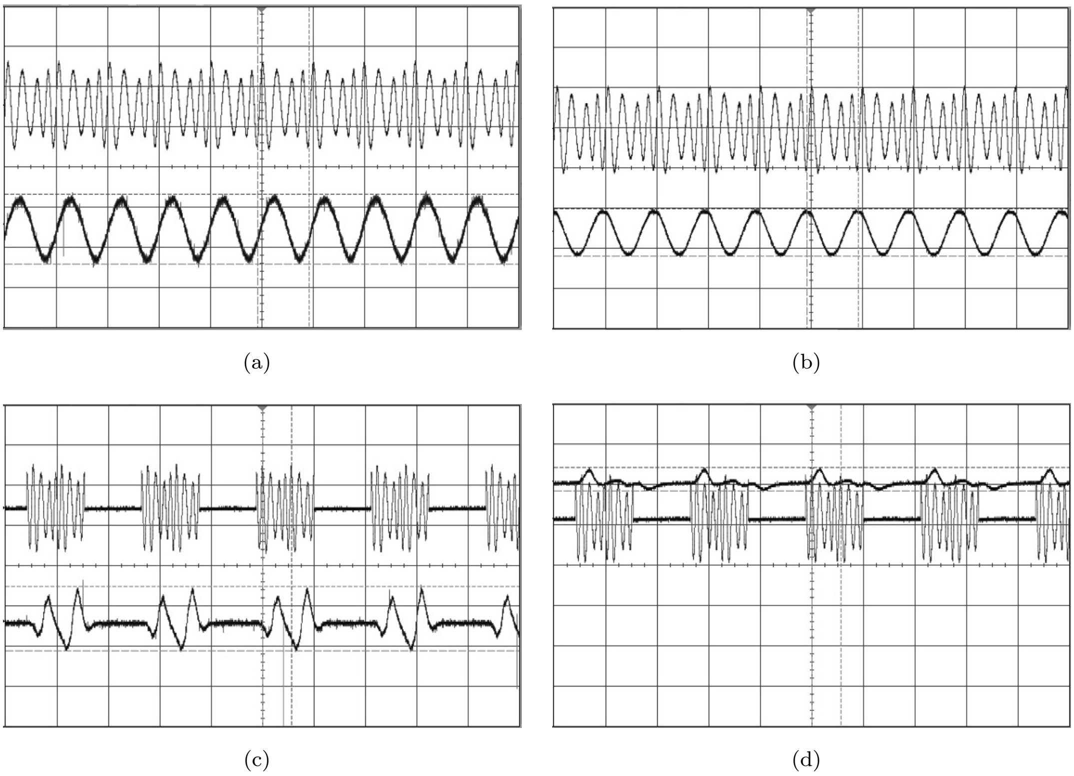
(a)

(b)

(c)

(d)

Fig. 4.9: (a) Extracted FM signal (trace 2 time scale of 124 μs/div and voltage scale of 50 mV/div) (b) Extracted AM signal from AM-FM input signal comprises of 32 kHz carrier, 8 kHz FM, 8 kHz AM, $\beta = 1.25$, and $M_1 = 0.25$ (trace 2 time scale of 124 μs/div and voltage scale of 200 mV/div) (c) Extracted FM signal (trace 2 time scale of 220 μs/div and voltage scale of 100 mV/div) (d) Extracted AM signal from AM-FM input signal comprises of 32 kHz carrier, 8 kHz FM, 8 kHz AM, $\beta = 1.25$, and $M_1 = 0.25$ for a dynamic change in carrier, FM and AM (trace 1 time scale of 220 μs/div and voltage scale of 200 mV/div). (Experiment)

The sampling frequency delivered by the SPG suitable for MWDFT bin-1 center frequency is 4.096 MHz. The clock of 50 MHz available in stratix III FPGA board had been divided to obtain a sampling frequency of 16.384 MHz, which is four times the 4.096 MHz (32 kHz X128 = 4.096 MHz) to run the entire PLL algorithm. The dynamic change in carrier, FM and AM are applied simultaneously by stopping the input signal for certain duration at arbitrary instant. The performance of the PLL in extraction of FM is depicted in Fig. 4.9(c). Similarly the performance of the PLL in extraction of AM is shown in Fig. 4.9(d). The extracted frequency is measured as 8.06 kHz for both FM and AM. The PI settings were chosen as $K_p = 0.01$ and $K_I = 0.01$. To ensure the PLL performance at different frequencies, the AM and FM frequency is changed to 4 kHz with $\beta = 1.25$,

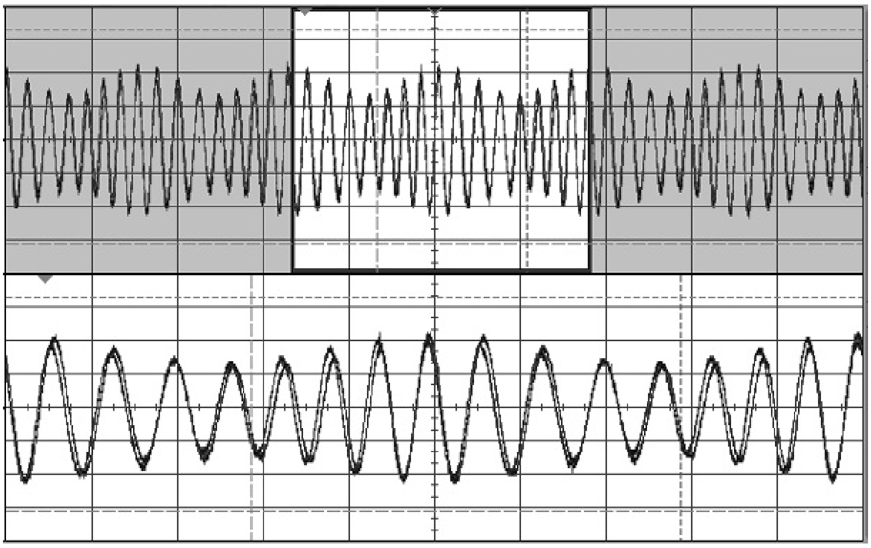

Fig. 4.10: AM-FM input signal and MWDFT in-phase component locking condition for a AM-FM signal carrier of 32 kHz, FM and AM modulation frequencies of 4 kHz, $\beta = 1.25$, and $M_1 = 0.25$ (trace 2 time scale of 140 μs/div and voltage scale of 50 mV/div) (Experiment)

$M_1 = 0.25$ and the locking condition of MWDFT in-phase component with input AM-FM signal shown in Fig. 4.10. The locking condition of the PLL could be seen from the zoomed portion of the Fig. 4.10. The experimental results for FM and AM extraction have been shown in two different figures because of the restriction of two DAC's available in HSMC board.

4.6 Summary

A AM-FM signal demodulation technique based on MWDFT filtering and phase locking scheme is proposed. A PLL has been designed to track the carrier signal; while the instantaneous amplitude and frequency information have been retrieved. The proposed scheme possesses quick acquisition behavior, wide operating range, stable, and negligible steady state error. With these characteristics, the proposed PLL is suitable for vibration analysis and speech processing. In vibration analysis, vibration frequency and amplitude can be extracted for large variations. In this research work, the wide operating range of the PLL has been exploited to extract large variation mono-component AM-FM signals. Further, the MWDFT PLL could be applied to multi-component AM-FM signal demodulation.

Chapter 5

MWDFT based Frequency-Locked Loop for FM demodulation

5.1 Introduction

Vibration measurement technique based on MWDFT-PLL has been proposed in chapter 3. It uses open-loop MWDFT filter in PLL algorithm. The input of PLL algorithm utilizes phase error for sampling frequency correction. Thus, it requires further calculation from the α signal to obtain modulation signal information. Further, PLL algorithm does not have the flexibility to increase it's bandwidth to cover larger range in vibration measurment. Therefore, this chapter proposed a scheme that used the closedloop MWDFT filter in FLL algorithm. The difference is that bandwidth can be increased through the closed-loop MWDFT filter and thus increases range of frequency demodulation. It also removes the inconvenient step of frequency estimation by frequency locking technique which utilizes the frequency error for sampling frequency correction.

Frequency estimation of time-varying sinusoidal signals has wide applications in the field of science and technology. Among the available techniques, phase-locked loop (PLL)/FLL filters are considered as most common techniques employed in frequency estimation. These frequency estimators are proved to be very efficient techniques for frequency demodulation [145], [146]. The moving-window based demodulation technique involves feed-forward and feedback demodulations. The MWDFT offers feed-forward demodulation as a tuned filter, which converts input frequency modulated (FM) signal into amplitude modulated (AM) signal. The AM signal is tracked by employing a feedback loop in the structure as PLL. The MWDFT can extract an instantaneous carrier variation of FM provided the sampling frequency (f_s) is adjusted adaptively to eliminate the windowing effect caused by carrier variation. Therefore, the moving-window based PLL involves adaptive f_s control and it could extract the FM variation successfully. The extracted modulation signal (α) reflects the depth of modulation (β) and then carrier variation ($f_c \pm \Delta f_c$) is obtained from α. In [147], first, the MWDFT is employed for extracting the fundamental frequency from the square-wave output of relaxation oscillator. Secondly, the MWDFT is employed in closed-loop for fixed f_s. To eliminate the windowing effect of both the MWDFTs adaptive f_s control is adopted. Further, the fundamental frequency of the square wave is estimated using MWDFT-FLL to measure the capacitance. Basically, this method estimates the frequency of input square-wave whereas the proposed method retrieves carrier deviation with single MWDFT.

In comparison to MWDFT-PLL, the proposed method focuses on (i) the bandwidth improvement, (ii) obtaining the carrier deviation directly from FLL, (iii) noise handling capacity, and (iv) less acquisition time. To this end, a MWDFT based FLL is proposed with adaptive f_s control. The proposed MWDFT-FLL offers frequency demodulation with less resources under following conditions:

(i) biased input,
(ii) large frequency deviation or large modulation index,
(iii) FM of decaying sinusoid,
(iv) noise and harmonics tolerance, and
(v) sampling adaptability.

Furthermore, the performance of MWDFT-FLL is compared with some promising existing techniques proposed in [148]-[150].

5.2 FM demodulation based on MWDFT-FLL

The proposed scheme involving (i) closed-loop MWDFT filter and (ii) adaptive f_s control is shown in Fig. 5.1. The received ultrasonic signal is an analog FM signal. This signal is applied to the ADC unit of the HSMC to convert in discrete-time domain. A discrete-time sinusoidal FM signal: $x_f(n) = A_1 sin(2\pi f_c n + \beta m(n))$ where, A_1 is amplitude of FM signal, f_c is carrier frequency, $\beta = \Delta f_c / f_m$ is the frequency modulation index, Δf_c is carrier deviation, and message signal $m(n) = sin(2\pi f_m n)$ is the real signal with frequency f_m. The received FM signal, $x_f(n)$ is applied to the MWDFT filter to extract the in-phase component $C_1(n)$ and quadrature phase component $S_1(n)$. The sampled input

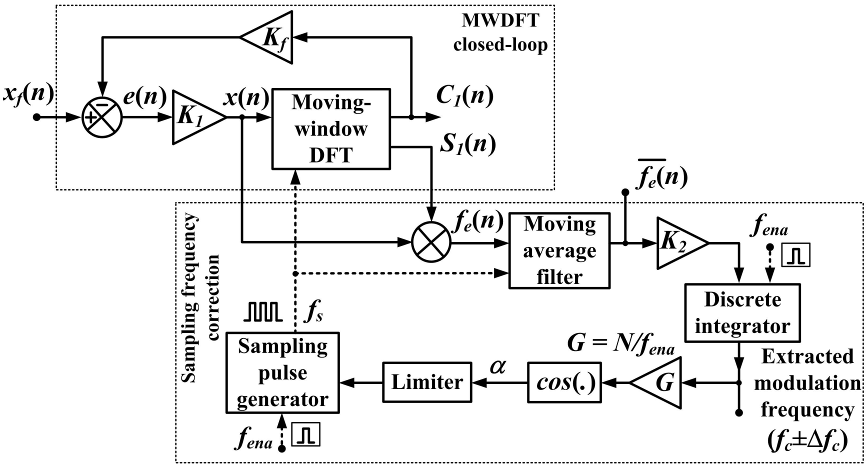

Fig. 5.1: Proposed MWDFT - FLL for FM demodulation.

$x(n)$ is applied to the MWDFT filter (open-loop) to extract the fundamental frequency component of (f_c). In MWDFT, at the n^{th} instant, the N-point DFT $(X_k(n))$ is computed for N input samples (previous samples) of $x(n)$ for a window width of N with help of previous instant DFT $(X_k(n-1))$ and moving the window by one sample. Therefore, the MWDFT is expressed in recursive form as

$$X_k(n) = [X_k(n-1) + \Delta x(n)]re^{j\theta_k} \tag{5.1}$$

where $X_k(n) = C_k(n) + jS_k(n)$ is the present instant DFT value, $C_k(n)$ and $S_k(n)$ are cosine and sine components of MWDFT filter output. The $\Delta x(n) = x(n) - r^N x(n-N)$, where $x(n)$ is sampled real input FM signal, r is damping factor, k is bin index, and $\theta_k = 2\pi k/N$. The MWDFT [151] algorithm (5.1) in matrix form is expressed as

$$\begin{aligned} \begin{bmatrix} C_k(n) \\ S_k(n) \end{bmatrix} &= \begin{bmatrix} r\cos\theta_k & -r\sin\theta_k \\ r\sin\theta_k & r\cos\theta_k \end{bmatrix} \begin{bmatrix} C_k(n-1) \\ S_k(n-1) \end{bmatrix} \\ &+ \begin{bmatrix} r\cos\theta_k \\ r\sin\theta_k \end{bmatrix} [x(n) - r^N x(n-N)] \end{aligned} \tag{5.2}$$

The typical r value is close to 1 $(r = 0.9998)$ which pushes the pole and zeros of the MWDFT inside the unit circle, so that instability is avoided. The frequency response of MWDFT (open-loop) is shown in Fig. 5.2. For fixed f_s, the variation in f_c will be reflected as magnitude and phase errors at $C_k(n)$ and $S_k(n)$. It could be observed that

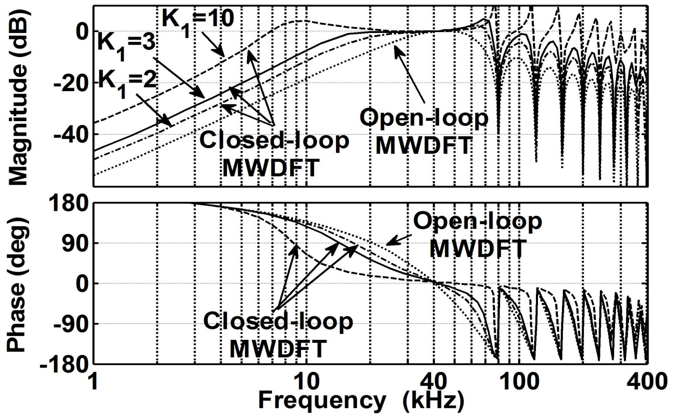

Fig. 5.2: Frequency responses of MWDFT for $k = 1$.

the unit magnitude and zero phase for center $f_c = 40\ kHz$ and bandwidth is limited. Therefore, when employing the open-loop MWDFT filter in PLL algorithm, range of f_m extraction is limited by bandwidth of the filter. Thus, the closed-loop MWDFT filter is introduced in FLL algorithm to increase the bandwidth.

5.2.1 MWDFT in closed-loop

To extract the fundamental component (f_c), $k = 1$, (5.2) is multiplied by $2/N$ using the DFT property. A closed-loop state-space model of (5.2) with negative feedback is developed to increase the bandwidth of MWDFT [147]. This structure is shown in Fig. 5.3. The parameter K_1 is feed-forward gain, K_f is feedback gain. For the closed-loop structure, $x_f(n)$ is the FM, sampled input, and $x(n)$ is the signal applied to MWDFT filter. The (5.2) becomes

$$\begin{aligned}\begin{bmatrix} C_1(n) \\ S_1(n) \end{bmatrix} &= \begin{bmatrix} r\cos\theta_1 & -r\sin\theta_1 \\ r\sin\theta_1 & r\cos\theta_1 \end{bmatrix} \begin{bmatrix} C_1(n-1) \\ S_1(n-1) \end{bmatrix} \\ &+ \begin{bmatrix} \frac{2}{N}K_1 r\cos\theta_1 \\ \frac{2}{N}K_1 r\sin\theta_1 \end{bmatrix} [x_f(n) - r^N x_f(n-N)] \\ &+ \begin{bmatrix} \frac{2}{N}K_1 K_f r\cos\theta_1 \\ \frac{2}{N}K_1 K_f r\sin\theta_1 \end{bmatrix} [-C_1(n-1) + r^N C_1(n-1-N)] \qquad (5.3)\end{aligned}$$

The frequency response of closed-loop structure is shown in Fig. 5.2. It could be observed that the negative feedback increases the bandwidth of MWDFT. Further, the responses are more flat around the tuned carrier $f_c = 40\ kHz$. Therefore, change in carrier frequency would result in less magnitude and phase errors at $C_1(n)$ and $S_1(n)$ in comparison with MWDFT open-loop response. The flat closed-loop response in Fig. 5.2 is also obtained for various K_1. These small magnitude and phase errors can be corrected by adaptive f_s correction.

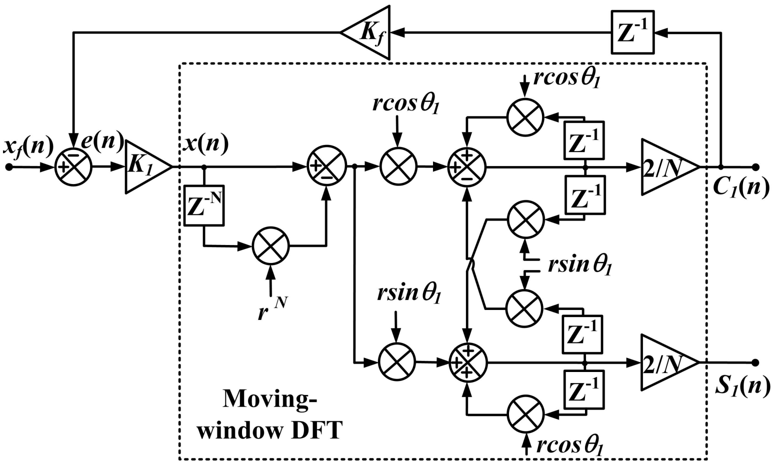

Fig. 5.3: MWDFT closed-loop structure.

5.2.2 Sampling frequency correction

The proposed scheme consists of closed-loop MWDFT and f_s correction mechanism [146]. The block diagram representation of the f_s correction of the proposed FM demodulator is shown in Fig. 5.1. For frequency estimation, let input signal be $x_f(n) = A_1 \sin(\omega_c n)$, then for carrier variation, $C_1(n) = A_2 \sin(\omega_c n \pm \phi)$ and $S_1(n) = A_2 \cos(\omega_c n \pm \phi)$. Further, error signal $e(n)$ is derived as $e(n) = x_f(n) - K_f C_1(n-1)$. Frequency error $f_e(n) = K_1(x_f(n) - K_f C_1(n-1)) \times S_1(n-1)$. Substituting the expressions of $x(n)$, $C_1(n-1)$ and $S_1(n-1)$ and then removing higher order frequency components by moving average filter $\overline{f_e(n)}$ is obtained. Under steady-state, the averager output signal is derived as

$$\begin{aligned}\overline{f_e(n)} &= (A_1^2 + K_f^2 A_2^2)(K_1^2 r/N) \sin\theta_1 \cos\omega_c \\ &- (K_1 K_f A_2^2 r/2) \sin(\omega_c + \theta_1) \qquad (5.4)\end{aligned}$$

The f_c can be extracted by integrating the $\overline{f_e(n)}$. Similarly, for the FM signal $x_f(n)$, the $\overline{f_e(n)}$ can be obtained that contains FM information in addition to carrier. The extracted f_c is passed through a cosine function to generate a signal (α) that reflects the change in f_c. The control signal α is applied as an input to sampling pulse generator (SPG) after passing through a limiter. The input of SPG $\alpha = \cos(2\pi(f_c \pm \Delta f_c)N/f_{ena})$, where f_{ena} is the enabling frequency of SPG. The $\overline{f_e(n)}$ adjusts f_s of MWDFT with SPG. For a FM signal, the discrete-time integrator (DTI) output signal (sinusoidal) will have the amplitude of $f_c \pm \Delta f_c$ and frequency of f_m after removing higher order spectral components. Thus, the f_m is retrieved from relation $\Delta f_c = \beta f_m$. The gain parameter K_2 is introduced before DTI to enhance the acquisition time of FLL. After convergence, (i) the $C_1(n)$ tracks the $x_f(n)$ (ii) DTI produces a message signal of amplitude $f_c \pm \Delta f_c$ with frequency of f_m, and (iii) SPG continuously producing $f_s \pm \Delta f_s$ pulses to enable the MWDFT.

5.2.3 Linearized model of MWDFT-FLL

To demonstrate the behavior of the proposed FLL, a linearized system model is developed in Fig 5.4. The transfer function of the system model is expressed as

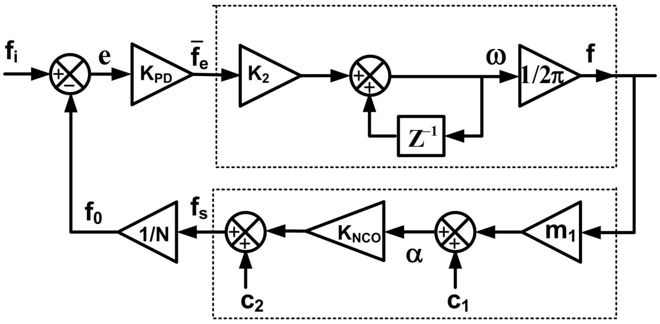

Fig. 5.4: Linearized model of MWDFT-FLL

$$\begin{aligned} f_0(z) &= \frac{K_{PD}K_2m_1K_{SPG}/2\pi N}{1+K_{PD}K_2m_1K_{SPG}/2\pi N - z^{-1}}f_i(z) \\ &+ \frac{(K_{SPG}/N)(1-z^{-1})}{1+K_{PD}K_2m_1K_{SPG}/2\pi N - z^{-1}}c_1(z) \\ &+ \frac{(1/N)(1-z^{-1})}{1+K_{PD}K_2m_1K_{SPG}/2\pi N - z^{-1}}c_2(z) \end{aligned} \tag{5.5}$$

Error e is calculated using input frequency f_i and output frequency f_0. For fixed f_s, the slope of f_c Vs $\overline{f_e}$ curve is plotted and $K_{PD} = 0.014$. The non-linear relation between the frequency f_c and α is linearized as $\alpha = m_1 f_c + c_1$, where $m_1 = -3.5 \times 10^{-5}$; $c_1 = 1.4$. The SPG expression between α and f_s is linearized as $f_s = K_{SPG}\alpha + c_2$, where $K_{SPG} = -3.6 \times 10^6$; $c_2 = 5.1 \times 10^6$. The f_s is converted into output frequency f_0 using $f_c = kf_s/N$ and $k = 1$.

5.3 Simulation Results

The MWDFT- FLL (Fig. 5.1) algorithm is implemented in MATLAB/Simulink using DSP builder tool. The closed-loop frequency responses (refer Fig. 5.2) are plotted for various K_1. As K_1 increases, the bandwidth of the MWDFT is increased. However, with f_s control, the operating range is decreased with increase in K_1. Therefore, $K_1 = 3$ is chosen to have more flat response. From frequency response, K_f is computed by the gain need to be added at f_c. For K_f selection, the frequency response of the closed-loop system for $K_f = 1$ is plotted. From this response, it was found that the gain of -9.356 dB is to be added at the center f_c to make it 0 dB. Thus, the gain K_f was found to be 0.663. The K_2 is chosen for faster convergence. The closed-loop parameters for simulation were set at $K_1 = 3$, $K_f = 0.663$, $K_2 = 303$, $r = 0.9998$ and $N = 128$. The following test-cases chosen for performance evaluation.

(i) Exponential decay: A FM signal with an exponential decaying f_m is applied as an input.

$$x_f(n) = A_1 \sin(2\pi f_c n + \beta e^{-\sigma n} \sin(2\pi f_m n)) \tag{5.6}$$

The parameters are $A_1 = 1$, $f_c = 40$ kHz, $f_m = 10$ kHz, $\beta = 1$ and $\sigma = 5000$. The performance of the FLL is shown in Fig. 5.5. The first trace shows FM input signal x_f, the second trace C_1 is the in-phase component of the MWDFT output, and the third trace $f_c \pm \Delta f_c$ is the demodulated signal. In Fig. 5.5, it could be observed that the initial conversion time is 0.176 ms and then perfect locking is achieved.

(ii) Step change: For $f_m = 0$, at 0.4 ms, the f_c is changed from 40 to 24 kHz and A_1 is

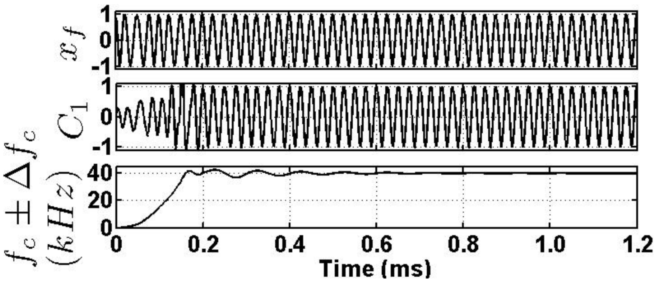

Fig. 5.5: Demodulation of exponentially decaying f_m (Simulation).

changed from 1 to 0.5 simultaneously in the x_f as shown in Fig. 5.6. Similarly, at 0.8

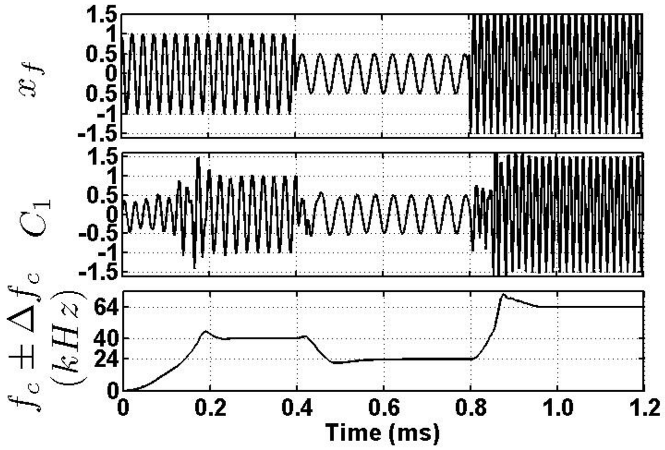

Fig. 5.6: Demodulation for step changes in f_c and amplitude (Simulation).

ms, a step change in f_c of 24 to 64 kHz and in amplitude A_1 of 0.5 to 1 are applied in x_f simultaneously. The initial conversion time is 0.176 ms to reach $f_c = 40$ kHz whereas for a deviation of 40 kHz (24 to 64 kHz) the FLL converges within 0.067 ms at 0.8 ms. Thus, FLL could adapt to the subsequent changes in carrier quickly. Furthermore, the FLL is capable of achieving perfect locking regardless of the changes in amplitude (range of 0.5 to 1.5) and wide range of Δf_c.

(iii) Input bias: FLL performance is tested for $f_m = 0$, the x_f of $f_c = 40$ kHz with input bias and shown in Fig. 5.7. At 0.4 ms, a step change in bias input is applied to x_f from 1 to 0.6 (20% change) and then, next step change is applied at 1 ms from 0.6 to 1.4 (40% change) in trace 1 Fig. 5.7. In trace 2, the in-phase signal C_1 takes 0.2 ms to lock with 40% biased shift. The change in carrier could be observed from trace 3 and the overshoot can be reduced further by adjusting K_1. Furthermore, a step change of 50% in amplitude can be achieved with $K_1 = 2$ but the decrease in frequency range is observed.

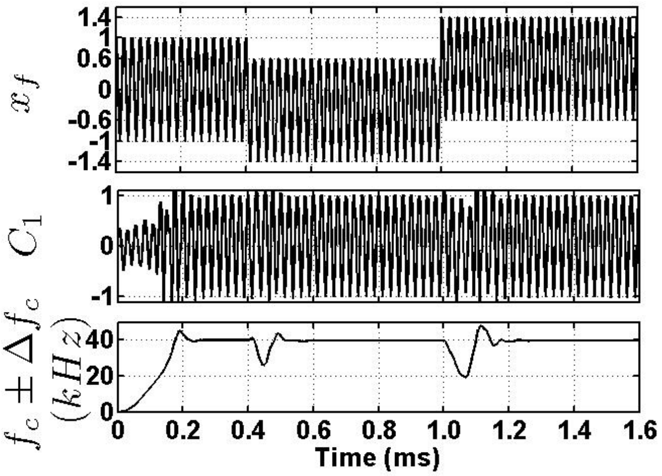

Fig. 5.7: Demodulation for biased sinusoidal carrier (Simulation).

(iv) Noise tolerance: To test the noise performance of the FLL, additive white Gaussian noise is added with x_f. Fig. 5.8 shows the noisy x_f, MWDFT output C_1, and extracted f_m. For a FM signal with $f_m = 500\ Hz$, $\Delta f_c = 10\ kHz$, and SNR 1.93 dB and 6.94 dB are shown in Fig. 5.8. The f_m could be extracted successfully in the presence of noise. The mean square error of estimated f_c is determined for different SNR and the trend is shown in Fig. 5.9. The proposed FLL technique offers better results than least squares differential ratio technique in [150]. Since MWDFT is a tuned filter, the proposed FLL possesses the advantage of removing all harmonics of the carrier.

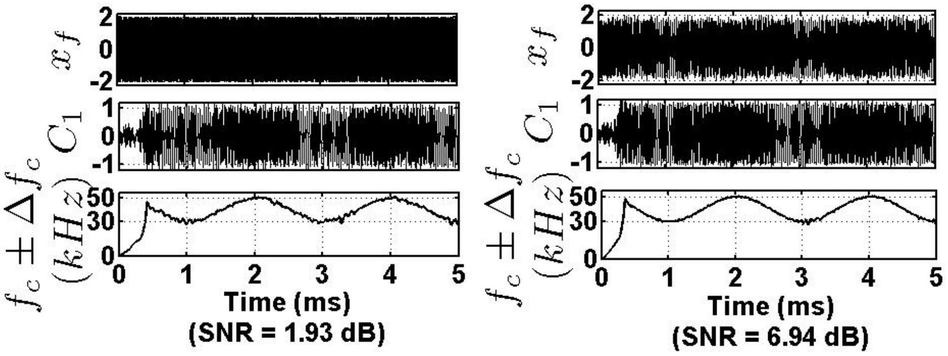

Fig. 5.8: Demodulation of a carrier signal with $f_m = 500\ Hz$ and $\Delta f_{c(p-p)} = 10\ kHz$ at different SNR (Simulation).

(v) Effects of additive noise, carrier deviation, and phase noise: Without f_s correction, the additive noise is removed by MWDFT filter in closed-loop structure, so $\overline{f}_e(n)$ is not affected by noise much; the carrier deviation shows a step change in $\overline{f}_e(n)$, and the phase

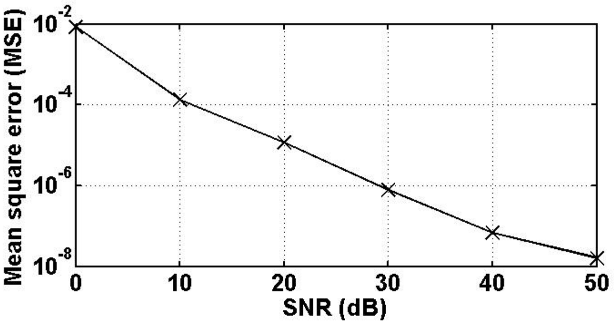

Fig. 5.9: Mean square error (MSE) at different SNR (dB)

noise is reflected as a phase change in $\overline{f}_e(n)$. Therefore, with f_s control, these effects are negligible in the demodulated signal.

5.3.1 Perfomance comparison

The estimated vibration amplitudes using MWDFT-PLL and FLL algorithm are provided in Table 5.1. Both methods perform well with less error in the frequency range of 10 Hz to 6 kHz. In PLL method, the maximum frequency of 6 kHz for $\beta = 0.5$ is estimated with error of 2.08 %, whereas the FLL method could estimate upto 10 kHz for same $\beta = 0.5$ with the error of 0.01 %.

Table 5.1: Estimated vibration amplitudes by MWDFT-PLL and FLL (Simulation)

f_m (Hz)	β range	K_I	Estimated $A_m(mm)$ (PLL)	% error	K_1	K_f	K_2	Δf_c (kHz)	Estimated $A_m(mm)$ (FLL)	% error
100	300.0	0.003	209.63	0.02	50	0.981	43	60.239	210.52	0.42
200	150.0	0.010	104.87	0.08	50	0.981	85	30.235	105.66	0.78
500	60.0	0.010	42.09	0.36	50	0.981	195	30.090	42.06	0.29
1000	10.0	0.010	7.01	0.32	3	0.663	303	9.990	6.98	0.10
2000	5.0	0.010	3.52	0.70	3	0.663	303	9.992	3.49	0.08
3000	2.0	0.011	1.41	1.12	3	0.663	303	6.010	1.40	0.16
4000	1.0	0.011	0.70	0.53	3	0.663	303	4.023	0.70	0.56
5000	1.0	0.012	0.70	0.34	3	0.663	303	5.060	0.71	1.20
6000	0.5	0.012	0.34	2.08	3	0.663	303	3.000	0.35	0.01
7000	0.5	-	-	-	3	0.663	303	3.495	0.35	0.17
8000	0.5	-	-	-	3	0.663	303	3.980	0.35	0.52
9000	0.5	-	-	-	3	0.663	303	4.450	0.35	1.30
10000	0.5	-	-	-	3	0.663	303	4.993	0.35	0.00

5.4 Experimental Validation

The proposed FLL demodulator is validated through experimental investigation. Block diagram representation of MWDFT-FLL algorithm implementation is shown in Fig. 5.10. The developed MATLAB simulink/DSP builder model is shown in Fig. 5.11 and Fig. 5.12. A high speed mezzanine card (HSMC) comprises of 14-bit ADC (AD9254) and DAC (DAC5672), is interfaced with Stratix III FPGA (EP3SL150F1152C2N) board through connectors. A FM signal is generated and fed to ADC channel at the sampling rate of 150 MHz. The DSP builder models are then converted to VHDL code with the help of Quartus-II synthesizer. After compilation, the VHDL code is downloaded to the FPGA through USB-Blaster JTAG connection. For experimental validation, the gain parameters are chosen as $K_1 = 3$, $K_f = 0.645$ and $K_2 = 380$. For a 40 kHz carrier, the carrier deviation $\Delta f_{c(p-p)}$ for theoretical, simulation and experiments are calculated with f_m variation from 0 to 10 kHz and plotted in Fig. 5.13 trace 1. The $\Delta f_{c(p-p)}$ adapted by FLL is more for low frequency region, and it reduces for the high frequency region. The trace 2 depicts the percentage deviation error with respect to the theoretical $\Delta f_{c(p-p)}$. For $f_m < 3$ kHz, the simulation and experiments produce the $\Delta f_{c(p-p)}$ of 28 kHz to 33 kHz with error less than 1%. For $f_m > 5$ kHz, the $\Delta f_{c(p-p)}$ is less than 10 kHz with error up to 2.16%. Furthermore, a FM signal with $f_c = 40$ kHz, $f_m = 10$ kHz, $\pm\Delta f_c = 2$ kHz is fed to the algorithm for demodulation. When the algorithm is programmed in FPGA, the various intermediate signals are tapped using signal tap analyzer with 8192 samples. Fig. 5.14 shows the tapped intermediate signals x_f, C_1, S_1, $\overline{f}_e$, f_m, α, and f_s in trace 1- trace 7 respectively. It could be observed that x_f, and in-phase component C_1 are perfectly locked, and S_1 is in quadrature with C_1. The trace 4, the moving average output shows

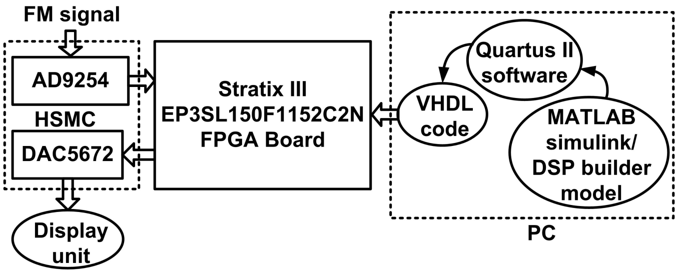

Fig. 5.10: Block diagram representation of MWDFT-FLL implementation

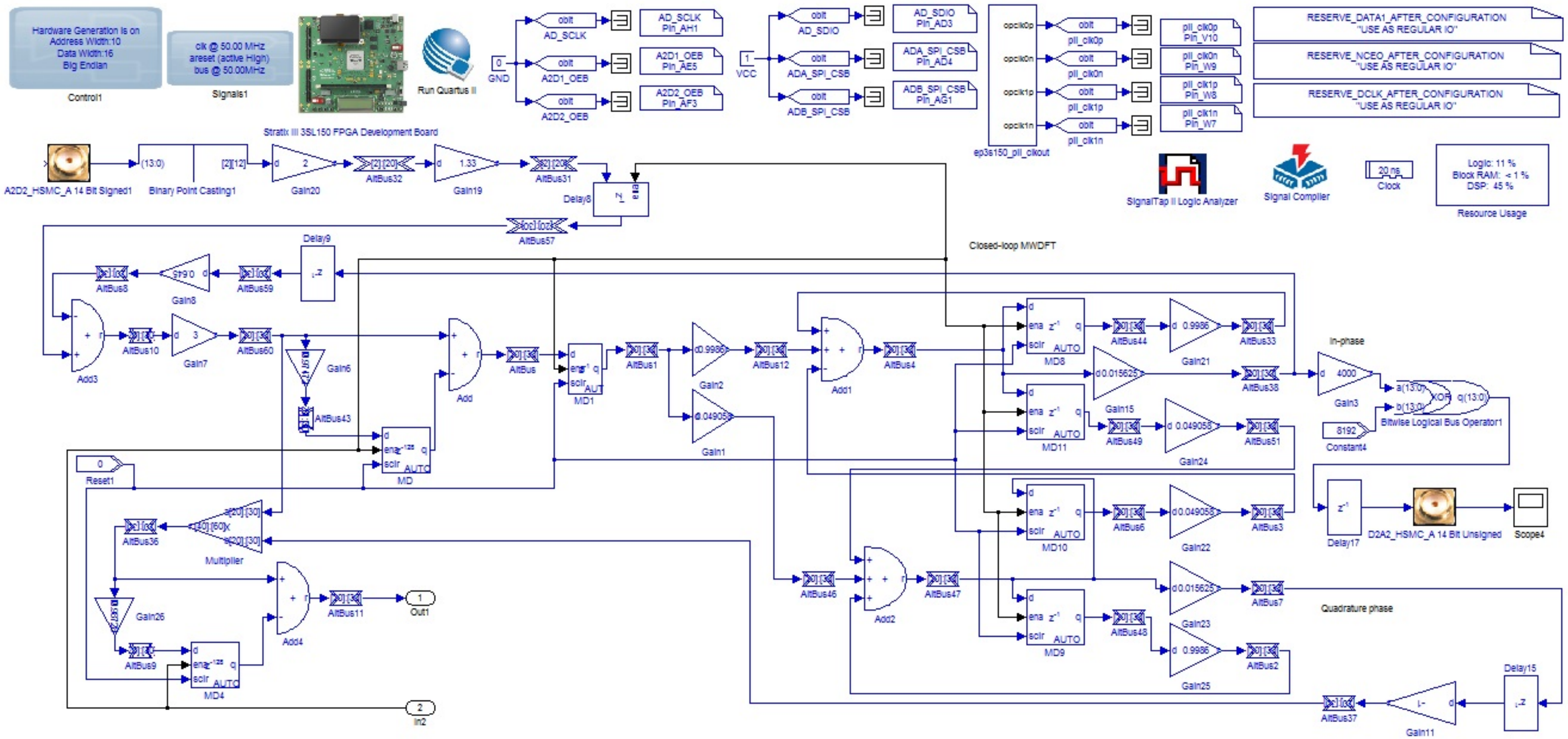

Fig. 5.11: Implementation of MWDFT-FLL (Closed-loop MWDFT)

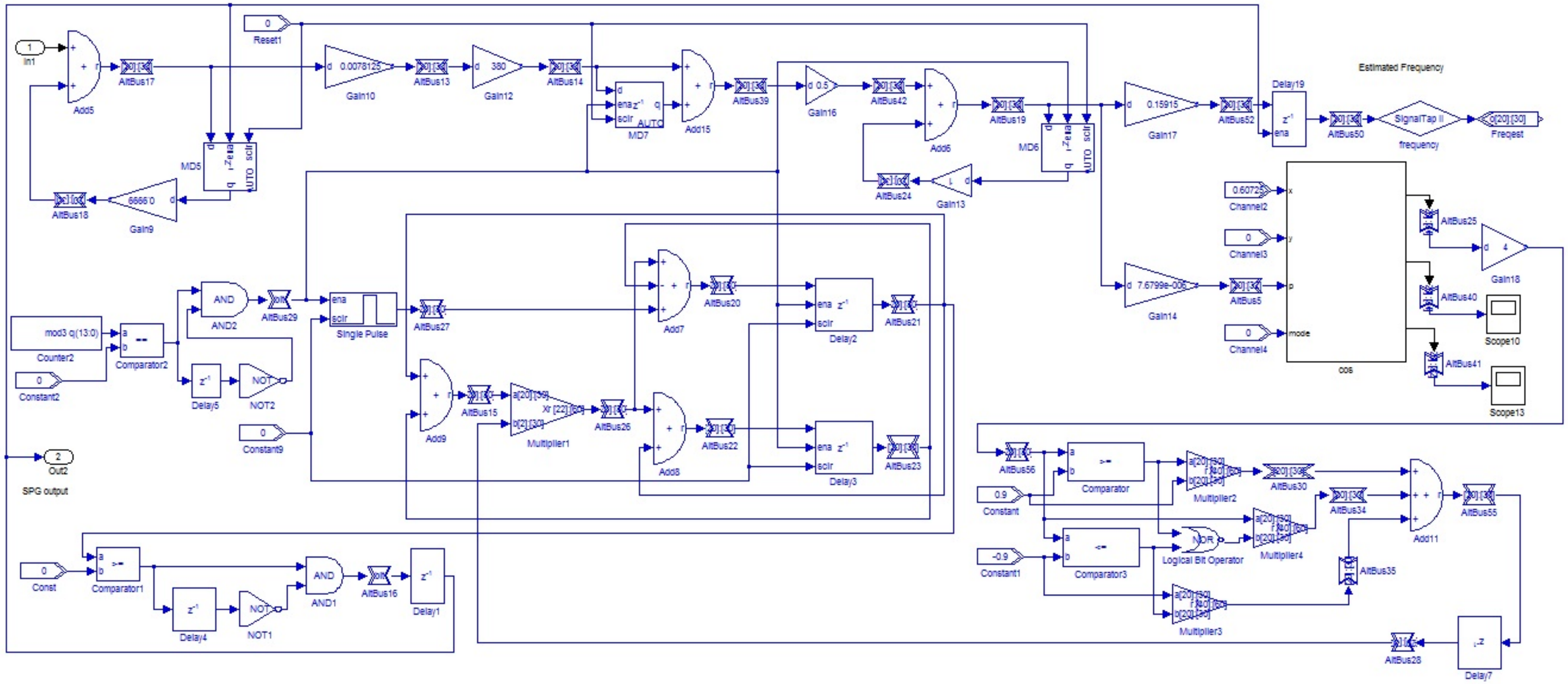

Fig. 5.12: Implementation of MWDFT-FLL (Sampling frequency correction)

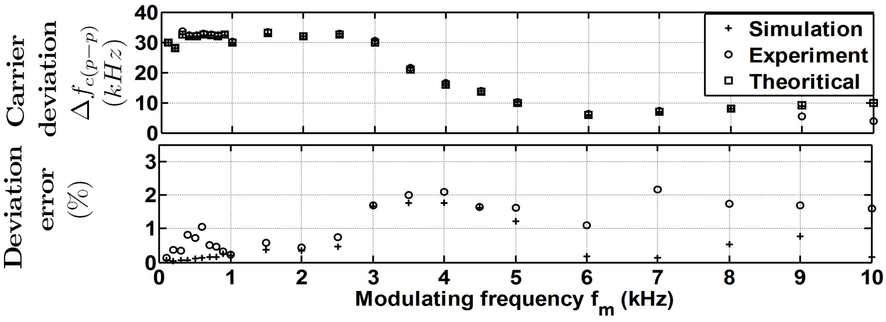

Fig. 5.13: The $\Delta f_{c(p-p)}$ and deviation error for the range of f_m.

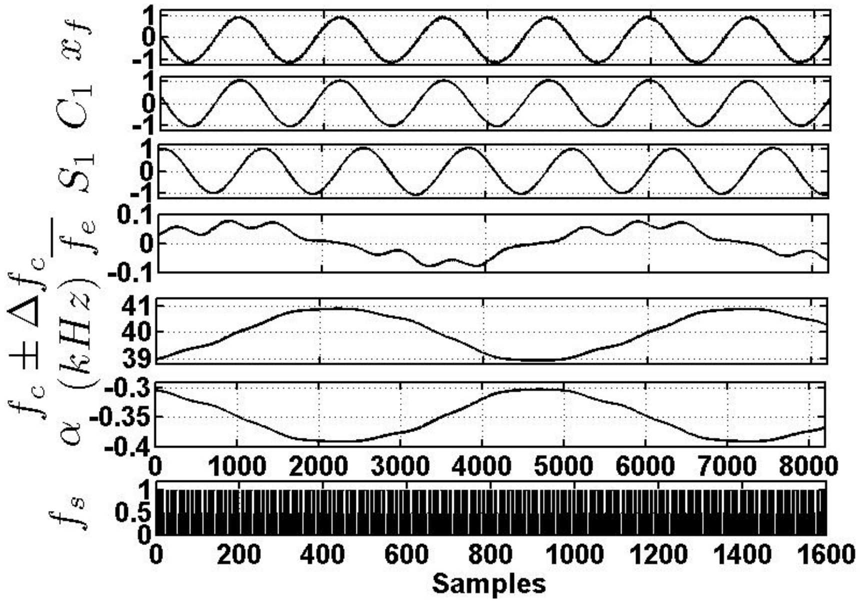

Fig. 5.14: Intermediate signals for $f_m = 10\ kHz$ and $\Delta f_{c(p-p)} = 2\ \ kHz$ (Experiment).

$\overline{f}_e = 0$. In trace 5, the extracted f_m shows deviation $\Delta f_{c(p-p)} = 2\ kHz$. The control signal α is positive for f_c less than center frequency 40 kHz, and its negative for $f_c > 40\ kHz$. The trace 7 shows the variable sampling pulses used for adaptive f_s control.

5.4.1 Performance comparison

The performance comparison of MWDFT PLL and FLL is carried out with the received signal (input) from function generator (F. G.) and Test equipment (T. E.). The vibration amplitude measurement for different f_m are listed in Table 5.2. these methods have been tested for the frequency range of 10 Hz to 6 kHz with different β. The MWDFT-PLL method could estimate upto 2 kHz with error the amplitude error of 2.14 %, whereas MWDFT-FLL could estimate upto 6 kHz with the error of 0.79 %. Therefore, FLL could measure wider vibration frequency. For a frequency range of 30 Hz to 100 Hz, both the methods offer almost same vibration amplitude measurement with the test equipment. This performance comparison is provided in Table 5.3.

Table 5.2: Vibration amplitude measurement performance comparison of MWDFT-FLL and PLL with F.G.

f_m (Hz)	β	α_{p-p}	A_m (mm) PLL	% error	A_m (mm) FLL	% error
10	1000	0.7585	692.35	0.95	691.97	1.00
100	150	1.0890	102.48	2.25	103.45	1.33
200	60	0.8980	41.40	1.19	41.33	1.46
500	10	0.3850	6.90	1.34	6.85	2.00
1000	10	0.7530	6.87	1.70	7.02	0.40
2000	7	1.0650	5.00	2.14	4.83	1.37
5000	1	-	-	-	0.695	0.57
6000	1	-	-	-	0.70	0.79

Table 5.3: Performance comparison of MWDFT-PLL and PLL with Test equipment

f_m (Hz)	S_i from T. E. (PLL)		S_i from T. E. (FLL)	
	α_{p-p}	A_m (mm)	Δf_c (Hz)	A_m (mm)
30	0.0134	4.00	323	3.76
40	0.0130	2.90	302	2.63
50	0.0108	1.90	253	1.77
60	0.0090	1.30	220	1.27
70	0.0086	1.10	218	1.09
80	0.0070	0.78	187	0.81
90	0.0054	0.53	136	0.53
100	0.0054	0.48	100	0.35

The MWDFT-FLL is compared with existing methods presented in [146], [148], [149] and their parameters comparison is provided in Table 5.4. The proposed method incorporates adaptation through f_s correction which is more accurate, whereas [149] employs FM signal as aperiodic sampling to improve the harmonic distortion. In the presence of input noise, the proposed method can extract FM at $SNR = 1.93$ dB. The MWDFT-FLL can estimate the input frequency in the presence of harmonics and bias as well. In [148], β reducing technique is employed that normally decreases the recovery signal strength. The frequency range is restricted with large Δf_c and particular f_m in [148] and f_m range is

Table 5.4: Comparison with existing techniques

Parameters	[146]	[148]	[149]	MWDFT-FLL
Range(f_m)	0 - 10 kHz	large Δf_c	$f_m < f_c/5$	0 - 10 kHz
SNR (dB)	8	>10	NA	1.93
Acquisition time	484 μs	NA	NA	67 μs
Input bias	capable	NA	NA	capable
Reduced β	no	yes	no	no
Adaptivity	f_s	no	FM	f_s
Harmonics	removed	NA	1%	removed

limited to $f_c/5$ in [149], whereas for the proposed method, the maximum demodulation frequency was found to be 10 kHz for f_c of 40 kHz. In [146], the initial response time for 40 kHz takes 104 μs but it does not reduce its response time for subsequent step chances whereas the MWDFT-FLL shows large reduced at subsequent step changes from 176 μs to 67 μs for same 40 kHz. The frequency estimation of the proposed FLL technique consumes 11.7% of the resources available whereas the previous technique [147] consumed 23.33% of the resources that is almost twice the size.

5.5 Velocity measurement

An acoustic method of velocity measurement based on the Doppler phase shift has many applications such as surface acoustic wave (SAW) measurement [19], fluid flow [20], [21], blood flow measurements [42], [63] surface velocity in a liquid [72], pipe-flow velocity [152], radar application [153]. Most of these velocity measurement techniques employed pulse echo or continuous ultrasonic waves. A sinusoid signal $S_i(t)$ of carrier frequency f_0 and amplitude A_m is transmitted towards a moving object having constant velocity V_i as shown in Fig. 5.15, where Tx is the ultrasonic transmitter and Rx is the ultrasonic receiver. The transmitted signal is

$$S_i(t) \quad = \quad A_m cos(2\pi f_0 t) \tag{5.7}$$

The received signal $S_o(t)$ undergoes Doppler shift (f_D) due to the constant velocity V_i of the moving object. Therefore, the received signal is

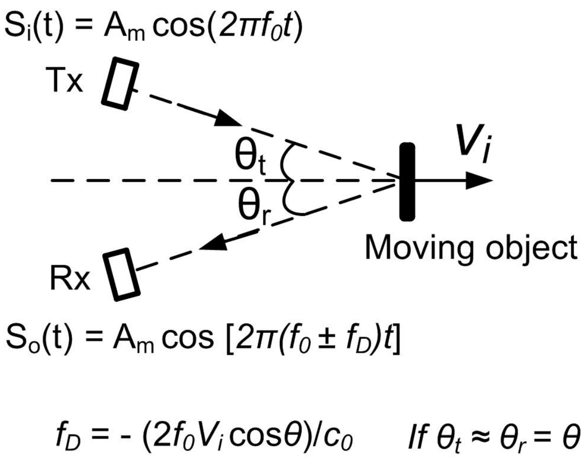

Fig. 5.15: Doppler shift due to constant velocity of a moving object

$$S_o(t) = A'_m cos(2\pi(f_0 \pm f_D)t) \tag{5.8}$$

where A'_m is the amplitude of received signal and f_D is the Doppler shift. The Doppler shift due to constant velocity V_i is defined as

$$f_D = \frac{2V_i cos(\theta) f_0}{c_0} \tag{5.9}$$

where θ is the angle between transmitted/reflected waves and the normal line of moving object, f_0 is the carrier frequency and c_0 is the speed of sound in air medium as shown in Fig. 5.15. From (5.9), the velocity (V_i) can be expressed as

$$V_i = \frac{f_D c_0}{2cos(\theta) f_0} \tag{5.10}$$

The velocity (V_i) can be measured by MWDFT based synchronization technique. The Doppler phase shift ($\beta_v t$) due to velocity term in (3.23) is proportional to the dc shift at output control signal (α). Corresponding velocity can be calculated from (α) (3.15) and frequency deviation (5.9) relation. With closed-loop MWDFT-FLL algorithm, the velocity (V_i) can be measured directly from the change in carrier f_0 as $f_D = \Delta f_0$.

5.5.1 Results and discussion

In Table 5.5, a range of input velocity V_i (0.5 to 30 m/s) is measured using MWDFT-FLL algorithm. The f_D is the theoretical Doppler shift due to velocity V_i, whereas f_m is the measured carrier shift with same velocity V_i. The measured velocity V_m is closed to V_i. In experimental verification, the input velocity of 0.46 cm/sec is estimated as 0.42 cm/sec.

Table 5.5: Velocity measured based on MWDFT-FLL algorithm for $\theta \approx 0^o$, $c_0 = 346$, and $f_c = 40\ kHz$ (Simulation)

$V_i\ (m/s)$	$f_D(Hz)$	$f_m(Hz)$	$V_m\ (m/s)$
0.5	116	105	0.45
1	231	225	0.97
5	1156	1146	4.96
10	2312	2320	10.03
30	6936	6930	29.97

5.6 Summary

The performance of the FLL designed with MWDFT is validated through experiments. The increase in bandwidth of the FLL is achieved through the closed-loop mechanism. In simulation, maximum modulating frequency of 10 kHz with $\beta = 0.5$ has been extracted using closed-loop MWDFT-FLL algorithm. A maximum f_m of 6 kHz with $\beta = 1$ has been tested in experiment. Therefore, the proposed FLL offers wider demodulation with closed-loop structure of MWDFT and f_s correction. The simulation results confirm that the proposed method can perform well in the presence of noise upto of $SNR = 1.93\ dB$, bias and harmonics. The MWDFT-FLL consumes less resources 11.7% of the resources available in FPGA implementation and therefore, less computational complexity. The velocity of moving object can be measured by MWDFT-PLL and FLL methods. The moving object velocity can be estimated from α in PLL, whereas FLL could estimate the velocity as direct shift in carrier. Theoretically, the proposed method MWDFT- FLL can estimate the velocity upto 30 m/s with less error. The moving object velocity of 0.46 cm/s was estimated in experiment.

Chapter 6

Conclusion

The acoustic based ultrasonic vibration measurement involves three types of phase shift at the received signal; phase shift due to path length between transmitter-object-receiver, phase shift introduced by Doppler effect due to vibrating object, and the parametric phase shift caused by interaction of high frequency ultrasonic wave and low pressure developed by vibrating object. Among the three phase shifts, Doppler phase shift contains the vibration informations such as amplitude, frequency and phase. The literature review focused on Doppler signal extraction and classified the different methods based on the β estimation techniques such as conventional, phase operation, ratio, correlation, standard deviation, Kalman, least-square, phase locking, and zero crossing. The classified methods are analyzed in terms of range of the vibration amplitude, frequency, and the preferable carrier frequency for transmission. Further, the analysis also presents various applications in which ultrasonic vibration measurements system are employed successfully.

The theoretical background of sounds interaction and its effect on vibration measurement has been analyzed. Moreover, the vibration measurement techniques such as CPPM, DACM, VSA, photoelectric and RF polarization methods did not involve Doppler effect.

The synchronization technique based on the MWDFT filter has been proposed for Doppler signal extraction in an ultrasonic vibration measurement systems. The proposed vibration measurement technique utilized a pair of ultrasonic transducers in which one transducer emits the continuous ultrasonic wave of 40 kHz towards the vibrating disc and another transducer receives the phase modulated ultrasonic signal. The MWDFT filter acts as quadrature detector and converts the FM input signal into AM-FM signal. The MWDFT filter output is applied to the carrier suppressor which is mainly consists of simple multiplier followed by moving-averager filter. The moving-averager filter allows to pass low frequencies near DC level but removed the higher frequency carrier terms present in the multiplier output. Then, the PI controller is applied to make the signal more smooth by removing other higher frequencies present in the moving-averager output. After removing the carrier and other higher frequencies, the information contained signal is termed as Doppler signal. The extracted Doppler signal is further processed to extract the phase modulating signal by sampling period adjustment of the MWDFT. The extracted modulated signal contains the vibration amplitude and frequency information. These parameters had been obtained for an electrodynamic vibration system by implementing the synchronization technique in FPGA. For a 40 kHz carrier, the carrier deviation of ± 34 kHz in terms of vibration amplitude and frequency can be measured. The proposed technique is validated up to 2 kHz vibration frequency using the test equipment.

When ultrasonic transducer received the FM signal with large modulation frequency or large modulation amplitude, the received signal appears AM-FM signal instead of phase or frequency modulated signal. Since, the input is AM-FM signal, the output of the MWDFT filter has two amplitude modulated signals and one frequency modulated signal. However, the information of vibration signal is contained only in frequency modulating signal. Thus, the proposed MWDFT-PLL algorithm has been modified to separate the AM and FM signals. In the modified algorithm, the sampling pulse generator produces sampling pulses suitable for MWDFT bin-1 and MWDFT bin-0 for the retrieval of frequency and amplitude modulation signals, respectively. Hence, this new algorithm falls under the category of combining the feed-forward and feedback demodulation techniques. The proposed scheme is capable of extracting IF and IA for the signals comprising of large variation in frequency and amplitude. In addition, the MWDFT incorporated in the PLL would extract the message signals in presence of noise. The proposed scheme is implemented in FPGA to validate the performance of MWDFT-PLL in decomposition of the mono-component AM-FM signal.

Closed-loop MWDFT filter has been introduced in FLL algorithm to improve its bandwidth for FM demodulation technique. When bandwidth of MWDFT filter is increased at the center frequency, the spectra of MWDFT exhibits almost flat response at amplitude. The characteristic of input frequency variation is utilized for tracking frequency modulated carrier. The small leakage observed in terms of magnitude and phase errors of MWDFT is further corrected by adaptive sampling frequency control. With increase in bandwidth in bandwidth, the range of frequency estimation extends up to 10 kHz.

The closed-loop MWDFT algorithm also increases the noise immunity up to SNR = 1.9 dB. Thus, the proposed algorithm offers frequency estimation under following conditions (i) biased input, (ii) large frequency deviation, (iii) frequency modulation of decaying sinusoid, and (iv) noise and harmonics.

Further, closed-loop MWDFT filter has been applied for velocity measurement of a moving object. When an ultrasonic transducer transmits a sinusoidal signal of 40 kHz toward the moving object having constant velocity, the reflected signal at the receiver appears as phase modulated signal due the Doppler effect. Then, the closed-loop MWDFT based FLL algorithm is applied on the phase modulated signal to give linear change in carrier phase. The linear change in phase shift is reflected as step change in estimated frequency. Thus, the constant velocity of the moving object is measured in terms of step change in carrier frequency. The simulation result shows that the proposed algorithm can measure the velocity upto 30 m/s.

6.1 Scope and future work

The proposed research work can be applied for vibration measurement such as characterization of structural vibration, vibration motor, displacement measurement, liquid flow measurement, and electric network frequency (ENF) estimation as forensic tool.

Further, the proposed research work can be carried out for advance medical application such as heart wall vibration measurement, tissue motion detection and blood velocity measurement. The parametric effects or interaction of sounds that produces phase modulation at the received signal can be included in the Doppler signal extraction for certain conditions. Furthermore, the research work can be extended for measurement of the vibration parameters (amplitude, frequency and phase) along with velocity of a moving object simultaneously.

Appendix A

Parameters and symbols:

A_m	Amplitude of vibration signal
A_c	Amplitude of carrier signal
A'_c	Amplitude of received signal
β:	Doppler modulation index due to vibration or frequency modulation index
β_v	Doppler modulation index due to velocity
c_0	Speed of sound in a medium
D	Distance between transmitter/receiver and vibration surface
d	Distance between transducers (transmitter and receiver)
E_{max}	Maximum values of the envelope in-phase component
E_{min}	Minimum values of the envelope in-phase component
f_c or f_0	Carrier frequency
f_{ena}	Enabling frequency
f_s	Sampling frequency
K_d	Phase error slope
K_P	Proportional gain
K_I	Integral gain
K_V	SPG gain
k_0	Wave number
L	Path length between transducers and moving surface
m	Amplitude modulation index
M_1	Amplitude modulation index
N	DFT window length
ω_c or ω_0	Carrier angular frequency
ω_m	Angular frequency of vibration signal
ω_{m1}	Angular frequency of AM message signal
ω_{m2}	Angular frequency of FM message signal

ϕ_D	Phase shift due to Doppler shift
ϕ_0	Phase shift due to path length
ϕ_P	Phase shift due to parametric effect
λ_c	Wavelength of carrier beam
α	Control signal or output signal of PI controller
r	Damping factor
T_s	Sampling period
θ	Angle between transmitter/receiver and normal line of vibration surface

Bibliography

[1] J. N. Juang and L. G. Horta, "A slewing Control Experiment for Flexible Structures," *Journal of Guidance and Control, and Dynamics,* vol. 9, no. 5, pp. 599-607, Sept.-Oct. 1986.

[2] M. S. Young and Y. C. Li, "A High Precision Ultrasonic System for Vibration Measurements," *Review of Scientific Instruments,* vol. 63, no. 11, pp. 5435-5441, Nov. 1992.

[3] B. George, H. Zangl, T. Bretterklieber, and G. Brasseur, "Seat Occupancy Detection System Based on Capacitive Sensing," *IEEE Trans. Instrum. Meas.,* vol. 58, no. 5, pp. 1487-1494, May 2009.

[4] K. A. Reddy, J. R. Bai, B. George, N. M. Mohan and V. J. Kumar, "Virtual Instrument for the Measurement of Haemo-dynamic Parameters Using Photoplethysmograph," *Proc. IEEE Instrumentation and Measurement Technology Conference,* pp. 1167-1171, April 2006.

[5] K. A. Reddy, B. George, and V. J. Kumar, "Use of Fourier Series Analysis for Motion Artifact Reduction and Data Compression of Photoplethysmographic Signals," *IEEE Trans. Instrum. Meas.,* vol. 58, no. 5, pp. 1706-1711, May 2009.

[6] R. Linbo, T. Geng, W. Jing, L. Haitao, and H. Hongfa, "Development of High-Speed Non-Contact Vibration Measurement System," *Proc. IEEE International Conference on Electronic Measurement and Instruments,* vol. 2, pp. 244-247, Aug. 2011.

[7] D. Tosi, M. Olivero, A. Vallan, and G. Perrone, "Signal Processing Enhanced Fiber Vibration Sensors,"*Key Engineering Materials,* vol. 543, pp. 302-305, Mar. 2013.

[8] E. O. Wygant, M. Kupnik, J. C. Windsor, W. M. Wright, M. S. Wochner, G. G. Yaralioglu, M. F. Hamilton, and B. T. K. Yakub, "50 kHz Capacitive Micromachined

Ultrasonic Transducers for Generation of Highly Directional Sound with Parametric Arrays," *IEEE Trans. Ultrason., Ferroelect., Freq. Contr.,* vol. 56, No. 1, pp. 193-202, Jan. 2009.

[9] M. Toda, "Phase-Matched Air Ultrasonic Transducers Using Corrugated PVDF Film with Half Wavelength Depth," *IEEE Trans. Ultrason., Ferroelect., Freq. Contr.,* vol. 48, No. 6, pp. 1568-1574, Nov. 2001.

[10] H. Carr and C. Wykes, "Diagnostic Measurements in Capacitive Transducers," *Ultrason.,* vol. 31, No. 1, pp. 13-20, 1993.

[11] G. Percin and B. T. K. Yakub,"Piezoelectrically Actuated Flextensional Micromachined Ultrasound Transducers-I: Theory," *IEEE Trans. Ultrason., Ferroelect., Freq. Contr.,* vol. 49, No. 5, pp. 573-584, May 2002.

[12] G. Percin and B. T. K. Yakub,"Piezoelectrically Actuated Flextensional Micromachined Ultrasound Transducers-II: Fabrication and Experiments," *IEEE Trans. Ultrason., Ferroelect., Freq. Contr.,* vol. 49, No. 5, pp. 585-595, May 2002.

[13] S. Zhao and Y. Zheng, "High Sensitivity Vibration Estimation using Pulse Echo Doppler Ultrasound," *Proc. IEEE Ultrason. Symp.,* vol. 2, pp. 1923-1926, Oct. 2003.

[14] O. B. Matar, J. P. Remenieras, C. Bruneel, A. Roncin, and F. Patat, "Noncontact Measurement of Vibration Using Airborne Ultrasound," *IEEE Trans. Ultrason. Ferroelect. Freq. Control,* vol. 45, no. 3, pp. 626-632, May 1998.

[15] R. J. Przybyla, S. E. Shelton, A. Guedes, I. I. Izyumin, M. H. Kline, D. A. Horsley, and B. E. Boser, "In-Air Rangefinding With an AlN Piezoelectric Micromachined Ultrasound Transducer," *IEEE Sensors J.,* vol. 11, No. 11, pp. 2690-2697, Nov. 2011.

[16] P. N. T. Wells, "Range-Gated Ultrasonic Doppler System," *Med. & Biol. Eng.,* vol. 7, pp. 641-652, Nov. 1969.

[17] J. E. Wilhjelm and P. C. Pedersen, "Target Velocity Estimation with FM and PW Echo Ranging Doppler Systems Part II: Systems Analysis," *IEEE Trans. Ultrason., Ferroelect., Freq. Contr.,* vol. 40, No. 4, pp. 373-380, July 1993.

[18] G. Harvey, A. Gachagan, and T. Mutasa, “Review of High-Power Ultrasound-Industrial Applications and Measurement Methods,” *IEEE Trans. Ultrason, Ferroelect., Freq. Control,* vol. 61, no. 3, pp. 481-495, Mar. 2014.

[19] N. Ramakrishnan, A. K. Namdeo, H. B. Nemade, and R. P. Palathinkal, “Simplified Model for FEM Simulation of SAW Delay Line Sensor,” *Proc. International Symposium on Robotics and Intelligent Sensors,* vol. 41, pp. 1022-1027, 2012.

[20] H. B. Nemade, T. Anjaneyulu, and P. C. Pandey, “Sensing Turbulence Transit Time by Pulsed Ultrasound for Single-Phase Fluid Flow Measurement,” *IEEE Trans. Instrum. Meas.,* vol. 47, no. 1, pp. 265-269, Feb. 1998.

[21] H. B. Nemade, T. Anjaneyulu, and, P. C. Pandey, “Single-Phase Fluid Flow Measurement by Pulsed Ultrasound Using Cross Correlation Technique,” *Proc. Symposium on Advances in Nuclear and Allied Instrumentation,* pp. 175-179, 1997.

[22] B. Zhuang, V. Shamdasani, S. Sikdar, R. Managuli, and Y. Kim, “Real-Time 3-D Ultrasound Scan Conversion Using a Multicore Processor,” *IEEE Trans. Inf. Technol. Biomed.,* vol. 13, no.4, pp. 571-574, July 2009.

[23] S. Sikdar, R. Managuli, V. Shamdasani, L. Gong, T. Hayashi, T. Mitake and Y. Kim, “A Single Mediaprocessor-Based Programmable Uultrasound System,” *IEEE Trans. Inf. Technol. Biomed.,* vol. 7, pp. 64-70, 2003.

[24] V. Shamdasani, R. Managuli, S. Sikdar, and Y. Kim, “Ultrasound Color-Flow Imaging on a Programmable System,” *IEEE Trans. Inf. Technol. Biomed.,* vol. 8, no.2, pp. 191-199, June 2004.

[25] F. Bejarano, A. Feeney, and M. Lucas, “Vibration Characterisation of Cymbal Transducers for Power Ultrasonic Applications,” *Journal of Physics: Conference Series*, vol. 382, pp. 1-6, 2012.

[26] A. Cardoni, P. Harkness, and M. Lucas, “Ultrasonic Rock Sampling Using Longitudinal-Torsional Vibrations,” *Ultrasonics,* vol. 50, pp. 447-452, 2010.

[27] P. Harkness, A. Cardoni, and M. Lucas, “Ultrasonic Rock Drilling Devices Using Longitudinal-Torsional Compound Vibration,” *Proc. IEEE International Ultrasonics Symposium,* pp. 2088-2091, Sep. 2009.

[28] V. Cevher, R. Velmurugan and J. H. McClellan, “Acoustic Multitarget Tracking using Direction-of-Arrival Batches,” *IEEE Trans. Signal Process.,* vol. 55, no. 6, pp. 2810-2825, Jun. 2007.

[29] V. Cevher, F. Shah, R. Velmurugan, and J. H. McClellan, “A Multi Target Bearing Tracking System using Random Sampling Consensus,” *Proc. IEEE Aerospace,* pp. 1-15, Mar. 2007.

[30] V. P. Panakkal and R. Velmurugan, “Effective Data Association Scheme for Tracking Closely Moving Targets Using Factor Graphs,” *Proc. IEEE Communications,* pp. 1-5, Jan. 2011.

[31] G. Harvey and A. Gachagan, “Noninvasive Field Measurement of Low-Frequency Ultrasonic Transducers Operating in Sealed Vessels,” *IEEE Trans. Ultrason, Ferroelect., Freq. Control,* vol. 53, no. 10, pp. 1749-1758, Oct. 2006.

[32] J. E. Wilhjelm and P. C. Pedersen, “Target Velocity Estimation with FM and PW Echo Ranging Doppler Systems Part I: Systems Analysis,” *IEEE Trans. Ultrason., Ferroelect., Freq. Contr.,* vol. 40, No. 4, pp. 366-372, July 1993.

[33] S. R. Huang, R. M. Lerner, and K. J. Parker, “Time Domain Doppler Estimators of the Amplitude of Vibrating Targets,” *J. Acoust. Soc. Am.,* vol. 91, no. 2, pp. 965-974, Feb. 1992.

[34] F. Figueroa and E. Barbieri, “An Ultrasonic Ranging System for Structural Vibration Measurements,” *IEEE Trans. Instrum. Meas.,* vol. 40, no. 4, pp. 764-769, Aug. 1991.

[35] J. Wang, X. Wang, L. Chen, J. Huangfu, C. Li, and L. Ran, “Noncontact Distance and Amplitude-Independent Vibration Measurement Based on an Extended DACM Algorithm,” *IEEE Trans. Instrum. Meas.,* vol. 63, no. 1, pp. 145-153, Jan. 2014.

[36] B. K. Park, O. B. Lubecke, and V. M. Lubecke, "Arctangent Demodulation With DC Offset Compensation in Quadrature Doppler Radar Receiver Systems," *IEEE Trans. Microw. Theory Techn.,* vol. 55, no. 5, pp. 1073-1079, May 2007.

[37] S. Sikdar, Y. Kim, D. F. Leotta, J. F. Primozich, and K. W. Beach, "Ultrasonic Techniques for Assessing Wall Vibrations in Stenosed Arteries," *Proc. IEEE Engineering in Medicine and Biology Society,* vol. 1, pp. 1325-1328, Sep. 2004.

[38] Y. Yamakoshi, J. Sato, and T. Sato, "Ultrasonic Imaging of Internal Vibration of Soft Tissue under Forced Vibration," *IEEE Trans. Ultrason., Ferroelect., Freq. Control,* vol. 37, no. 2, pp. 45-53, Mar. 1990.

[39] K. Kawabe, H. Kanai, and N. Chubachi, "Accuracy Evaluation in Ultrasonic-Doppler-Based Measurement of Small Vibrations for Acoustical Diagnosis of the Aortic Wall," *Electron. lett.,* vol. 29, no. 10, pp. 915-916, May 1993.

[40] J. Li and Y. Wang, "Doppler Shift Mitigating Algorithm for Quadrature Phase Delay Estimator," *IEEE Trans. Instrum. Meas.,* vol. 58, no. 8, pp. 2743-2746, Aug. 2009.

[41] F. Schadt, F. Mohr, and M. Holzer, "Application of Kalman Filters as a Tool for Phase and Frequency Demodulation of IQ Signals," *Proc. IEEE Region 8 Sibircon,* pp. 421-424, July 2008.

[42] C. Kasai, K. Namekawa, A. Koyano, and R. Omoto, "Real-Time Two-Dimensional Blood Flow Imaging Using an Autocorrelation Technique," *IEEE Trans. Sonics Ultrason.,* vol. 32, no. 3, pp. 458-464, May 1985.

[43] W. D. Barber, J. W. Eberhard, and S. G. Karr, "A New Time Domain Technique for Velocity Measurements using Doppler Ultrasound," *IEEE Trans. Biomed. Eng.,* vol. 32, no. 3, pp. 213-229, Mar. 1985.

[44] Y. Zheng, S. Chen, W. Tan, and J. F. Greenleaf, "Kalman filter motion detection for vibro-acoustography using pulse echo ultrasound," *Proc. IEEE Ultrason. Symp.,* vol. 2, pp. 1812-1815, Oct. 2003.

[45] Y. Zheng, S. Chen, W. Tan, X. Zhang, and J. F. Greenleaf, “Detection of shear wave propagation in an artery using pulse echo ultrasound and Kalman filtering,” *Proc. IEEE Ultrason. Symp.,* vol. 2, pp. 1251-1253, Aug. 2004.

[46] Y. Zheng, S. Chen, W. Tan, R. Kinnick, and J. F. Greenleaf, “Detection of Tissue Harmonic Motion Induced by Ultrasonic Radiation Force Using Pulse-Echo Ultrasound and Kalman Filter,” *IEEE Trans. Ultrason., Ferroelect., Freq. Control,* vol. 54, no. 2, pp. 290-300, Feb. 2007.

[47] C. F. Olsen, “Doppler Ultrasound: A Technique for Obtaining Arterial Wall Motion Parameters,” *IEEE Trans. Sonics Ultrason.,* vol. 24, no. 6, pp. 354-358, Nov. 1977.

[48] C. M. Orallo, I. Carugati, S. Maestri, P. G. Donato, D. Carrica, and M. Benedetti, “Harmonics Measurement With a Modulated Sliding Discrete Fourier Transform Algorithm,” *IEEE Trans. Instrum. Meas.,* vol. 63, no. 4, pp. 781-793, Apr. 2014.

[49] G. C. Hsieh and J. C. Hung, “Phase-Locked Loop Techniques-A Survey,” *IEEE Trans. Ind. Electron.,* vol. 43, no. 6, pp. 609-615, Dec. 1996.

[50] W. C. Lindsey and C. M. Chie, “A Survey of Digital Phase-Locked Loops,” *Proc. IEEE,* vol. 69, no. 4, pp. 410-431, April 1981.

[51] K. Sunagawa, H. Kanai, and M. Tanaka, “Simultaneous Measurement of Blood Flow and Arterial Wall Vibrations in Radial and Axial Directions,” *Proc. IEEE Ultrason. Symp.,* vol. 2, pp. 1541-1544, Oct. 2000.

[52] H. Kanai, M. Sato, Y. Koiwa, and N. Chubachi, “Transcutaneous Measurement and Spectrum Analysis of Heart Wall Vibration,” *IEEE Trans. Ultrason, Ferroelect., Freq. Control,* vol. 43, no. 5, pp. 791-810, Sep. 1996.

[53] T. Addabbo, R. Biondi, S. Cioncolini, A. Fort, F. Rossetti, and V. Vignoli, “A Zero-Crossing Detection System Based on FPGA to Measure the Angular Vibrations of Rotating Shafts,” *IEEE Trans. Instrum. Meas.,* vol. 63, no. 12, pp. 3002-3010, Nov. 2014.

[54] G. H. Raz, "Modeling and Simulation of FM Detection by Zero-Crossing in the Presence of Noise and DS Interference," *Proc. IEEE International Conference on Vehicular Technology,* vol. 2, pp. 1409-1413, May 1996.

[55] R. G. Wiley, "Approximate FM Demodulation using Zero Crossings," *IEEE Trans. Commun.,* vol. 29, no. 7, pp. 1061-1065, July 1981.

[56] G. S. Gill and S. C. Gupta, "First -Order Discrete Phase Locked Loop with Applications to Demodulation of Angle-Modulated Carrier," *IEEE Trans. Commun.,* vol. 20, no. 3, pp. 454-462, June 1972.

[57] C. Spiegel, S. Rickers, G. H. Bruck, and P. Jung, "Impact of Frequency offsets on Zero-Crossing Demodulation based Receivers," *Proc. IEEE International Conference on Applied Sciences in Biomedical and Communication Technologies,* pp. 1-5, Nov. 2010.

[58] O. B. Matar, J. P. Remenieras, L. Pizarro, A. Roncin, and F. Patat, "Performances of the Parametric Acoustic Vibrometer for Vibration Sensing," *Proc. IEEE Ultrason. Symp.,* vol. 1, pp. 605-607, Oct. 1997.

[59] O. B. Matar, J. P. Remenieras, C. Bruneel, A. Roncin, and F. Patat, "Ultrasonic Sensing of Vibrations," *Ultrason.,* vol. 36, pp. 391-396, Feb. 1998.

[60] R. E. Best, "Phase-Locked Loops: Design, Simulation, and Applications," *New York: McGraw-Hill,* 1999.

[61] D. R. Stephens, "Phase-Locked Loops for Wireless Communications: Digital, Analog and Optical Implementations," *New York: Kluwer Academic Publishers,* 2002.

[62] H. C. Hardy, "Apparatus for Measuring Vibrations," *Unitate State Patent 2733597*, pp. 1-6, Feb. 1956.

[63] B. A. J. Angelsen and K. Kristoffersen, "On Ultrasonic MTI Measurement of Velocity Profiles in Blood Flow," *IEEE Trans. Biomed. Eng.,* vol. 26, no. 12, pp. 665-671, Dec. 1979.

[64] B. A. J. Angelsen, “A Theoretical Study of the Scattering of Ultrasound from Blood,” *IEEE Trans. Biomed. Eng.,* vol. 27, no. 2, pp. 61-67, Feb. 1980.

[65] B. A. J. Angelsen, “Instantaneous Frequency, Mean Frequency, and Variance of Mean Frequency Estimators for Ultrasonic Blood Velocity Doppler Signals,” *IEEE Trans. Biomed. Eng.,* vol. 28, no. 11, pp. 733-741, Nov. 1981.

[66] B. A. J. Angelsen and K. Kristoffersen, “Discrete Time Estimation of the Mean Doppler Frequency in Ultrasonic Blood Velocity Measurements,” *IEEE Trans. Biomed. Engg.,* vol. 30, no. 4, pp. 207-214, April 1983.

[67] D. E. Hokanson, D. E. Strandness, JR., and C. W. Miller, “An Echo-Tracking System for Recording Arterial-Wall Motion,” *IEEE Trans. Sonics Ultrason.,* vol. 17, no. 3, pp. 130-132, July 1970.

[68] H. Kanai, H. Satoh, K. Hirose, and N. Chubachi, “A New Method for Measuring Small Local Vibrations in the Heart Using Ultrasound,” *IEEE Trans. Biomed. Eng.,* vol. 40, no. 12, pp. 1233-1242, Dec. 1993.

[69] S. Sikdar, B. Zhuang, M. Zaccardi, D. Leotta, K. W. Beach, and Y. Kim, “Ultrasonic Doppler Measurement of Tissue Vibrations: Opportunities and Limitations,” *Proc. IEEE Ultrason. Symp.,* pp. 1341-1344, Oct. 2006.

[70] G. Carson, A. J. Mulholland, A. Nordon, and A. Gachagan, “Theoritical Analysis of Ultrasonic Vibration Spectra from Multiple Particle-plate Impacts,” *IEEE Trans. Ultrason. Ferroelect., Freq., Control,* vol. 56, no. 5, pp. 1034-1041, May 2009.

[71] H. W. Persson and H. Hakansson, “Remote Vibration Measurements using Airborne Ultrasound,” *Proc. IEEE Ultrason. Symp.,* vol. 1, pp. 689-692, Nov. 1996.

[72] D. Royer, O. Casula, O. B. Matar, and F. Patat, “An Ultrasonic Phase Sensitive Method for Surface Velocity Measurements in a Liquid,” *Proc. IEEE Ultrason. Symp.,* vol. 1, pp. 635-638, Nov. 1996.

[73] R. Gupta, A. Kumar, R. Bahl, “Motion Parameter Estimation of A Radiating Point Source with Multiple Tonals Using Acoustic Doppler Analysis,” *Proc. IEEE Underwater Technology,* pp. 1-6, Mar. 2013.

[74] H. Sugimatsu, T. Ura, K. Mizuno, A. Asada,J. Kojima, R. Bahl, S. Behera, H. Singh, V. S. Sagar, "Study of Acoustic Characteristics of Ganges River Dolphin Calf using Ehcolocation Clicks Recorded During Long-Term In-Situ Observation," *Proc. IEEE Oceans,* pp. 1-7, Oct. 2012.

[75] A. G. Petculescu and J. M. Sabatier, "Air-Coupled Ultrasonic Sensing of Grass-Covered Vibrating Surfaces; Qualitative Comparisons with Laser Doppler Vibrometry," *J. Acoust. Soc. Am.,* vol. 115, no. 4, pp. 1557-1564, April 2004.

[76] X. Li, K. Nakamura, and S. Ueha, "Cancellation of Parametric-Effect-Induced Error in Airborne Ultrasound Doppler Velocimetry," *Acoust. Sci. and Tech.,* vol. 26, no. 4, pp. 338-344, 2005.

[77] J. J. Wen and M. A. Breazeale, "A Diffraction Beam Field Expressed As The Superposition of Gaussian Beams," *J. Acoust. Soc. Am.,* vol. 83, no. 5, pp. 1752-1756, May 1988.

[78] U. Ingard and D. C. P. Brown, "Scattering of Sound by Sound," *J. Acoust. Soc. Am.,* vol. 28, no. 3, pp. 367-369, May 1956.

[79] P. J. Westervelt, "Scattering of Sound by Sound," *J. Acoust. Soc. Am.,* vol. 29, no. 2, pp. 199-203, Feb. 1957.

[80] J. L. S. Bellin and R. T. Beyer, "Scattering of Sound by Sound," *J. Acoust. Soc. Am.,* vol. 32, no. 3, pp. 339-341, March 1960.

[81] L. W. Dean, "Interactions between Sound Waves," *J. Acoust. Soc. Am.,* vol. 34, no. 8, pp. 1039-1044, Jan. 1962.

[82] P. J Westervelt, "Parametric Acoustic Array," *J. Acoust. Soc. Am.,* vol. 35, no. 4, pp. 535-537, April 1963.

[83] J. J. Truchard, "Parametric Receiving Array and The Scattering of Sound by Sound," *J. Acoust. Soc. Am.,* vol. 64, no. 1, pp. 280-285, July 1978.

[84] M. J. Lighthill, "On Sound Generated Aerodynamically I. General Theory," *Royal Society of London,* vol. 211, no. 1107, pp. 564-587, Mar. 1952.

[85] M. J. Lighthill and F. R. S., "On Sound Generated Aerodynamically II. Turbulence as a Source of Sound," *Royal society of London,* vol. 222, no. 1148, pp. 1-32, Feb. 1954.

[86] E. A. Zabolotskaya, R.V. Khokhlov, "Quasi-Planes Waves in Nonlinear Acoustics of Confined Sound Beams," *Sov. Phys. Acoust.,* vol. 15, no. 1, pp. 40-47, Dec. 1969.

[87] V. P. Kuznetsov, "Equations of Nonlinear Acoustics," *Sov. Phys. Acoust.,* vol. 16, pp. 467-470, 1971.

[88] J. P. Remenieras, S. Calle, O. B. Matar, and F. Patat, "Nonlinear Interactions of Sound Fields Generated by a Focused Annular Array: Application to Vibro-Acoustography," *Proc. IEEE Ultrason. Symp.,* vol. 2, pp. 1573-1576, Oct. 2000.

[89] A. Hein and W. D. OBrien, "Current Time-Domain Methods for Assessing Tissue Motion by Analysis from Reflected Ultrasound Echoes-A Review," *IEEE Trans. Ultrason., Ferroelect., Freq. Control,* vol. 40, no. 2, pp. 84-102, Mar. 1993.

[90] F. A. Everest, "Master Handbook of Acoustics," *Fourth Edition, McGraw-Hill,* 2001.

[91] D. Censor, "Theory of Doppler Effect: Fact, Fiction and Approximation," *Radio Science,* vol. 19, no. 4, pp. 1027-1040, July 1984.

[92] Jean, "Censor's Acoustical Doppler Effect analysis - Is It a Valid Method?," *J. Acoust. Soc. Am.,* vol. 83 , no. 4, pp. 1681-1682, April 1988.

[93] N. Aydin, L. Fan, and D. H. Evans, "Quadrature-to-Directional Format Conversion of Doppler Signals using Digital Methods," *Physiol. Meas.,* vol. 15, no. 2, pp. 181-199, 1994.

[94] M. Kunita, M. Sudo, S. Inoue, and M. Akahane, "A New Method for Blood Velocity Measurements Using Ultrasound FMCW Signals," *IEEE Trans. Ultrason., Ferroelect., Freq. Control,* vol. 57, no. 5, pp. 1064-1076, May 2010.

[95] X. J. Tao, I. Claesson, and N. Grbic, "Narrowband Acoustic Doppler Volume Backscattering Signal - Part I: Evolutionary Spectral Analysis," *IEEE Trans. Signal Process.,* vol. 50, no. 11, pp. 2644 - 2655, Nov. 2002.

[96] M. W. Urban, S. Chen, and J. F. Greenleaf, “Harmonic Motion Detection in a Vibrating Scattering Medium,” *IEEE Trans. Ultrason., Ferroelect., Freq. Control,* vol. 55, no. 9, pp. 1956-1974, Sep. 2008.

[97] W. Kiranon and P. Wardkein, “A Novel FM Demodulation Scheme,” *IEEE Trans. Consum. Electron.,* vol. 41, no. 4, pp. 1103-1107, Nov. 1995.

[98] R. Gupta, A. Kumar, R. Bahl, “Estimation of Instantaneous Frequencies using iterative Empirical Mode Decomposition,” *J. Signal, Image and Video Processing,* vol. 8, pp. 799-812, July 2014.

[99] S. R. Huang, R. M. Lerner and K. J. Parker, “On Estimating the Amplitude of Harmonic Vibration from the Doppler Spectrum of Reflected Signals,” *J. Acoust. Soc. Am.,* vol. 88, no. 6, pp. 2702-2712, Dec. 1990.

[100] J. M. B. Dias and J. M. N. Leitao, “Nonparametric Estimation of Mean Doppler and Spectral Width,” *IEEE Trans. Geosci. Remote Sens.,* vol. 38, no. 1, pp. 217-282, Jan. 2000.

[101] P. J. Vaitkus and R. S. C. Cobbold, “A New Time-Domain Narrow band Velocity Estimation Technique for Doppler Ultrasound Flow Imaging. Part I: Theory,” *IEEE Trans. Ultrason., Ferroelect., Freq. Control,* vol. 45, no. 4, pp. 939-954, July 1998.

[102] P. Sumathi and P. A. Janakiraman, “Integrated Phase-Locking Scheme for SDFT-Based Harmonic Analysis of Periodic Signals,” *IEEE Trans. Circuits Syst. II, Exp. Briefs,* vol. 55, no. 1, pp. 51-55, Jan. 2008.

[103] P. Sumathi, “A Frequency Demodulation Technique Based on Sliding DFT Phase Locking Scheme for Large Variation FM Signals,” *IEEE Commun. Lett.,* vol. 16, no. 11, pp. 1864-1867, Nov. 2012.

[104] C. M. Darvennes and M. F. Hamilton, “Scattering of Sound by Sound from two Gaussian Beams,” *J. Acoust. Soc. Am.,* vol. 87, no. 5, pp. 1955-1964, May 1990.

[105] D. W. Baker, “Pulsee Ultrasonic Doppler Blood-Flow Sensing,” *IEEE Trans. Sonics Ultrason.,* vol. 17, no. 3, pp. 170-185, July 1970.

[106] B. Cherek, "Contactless Measurement of Mechanical Vibrations Based on the Doppler Effect," *IEE Proceeding A,* vol. 134, no. 4, pp. 339-342, April 1987.

[107] H. Hasegawa and H. Kanai, "Improving Accuracy in Estimation of Artery-Wall Displacement by Referring to Center Frequency of RF Echo," *IEEE Trans. Ultrason., Ferroelect., Freq. Control,* vol. 53, no. 1, pp. 52-63, Jan. 2006.

[108] M. Nakamura, T. Ishikawa, S. Kobashi, K. Kuramoto, and Y. Hata, "Blood Flow Detection under Skull by Doppler Effect," *Proc. IEEE International Conference on Systems, Man, and Cybernatics,* pp. 758-763, Oct. 2011.

[109] M. I. Plett, K. W. Beach, B. Dunmire, K. G. Brown, J. F. Primozich, and E. Strandness, "In Vivo Ultrasonic Measurement of Tissue Vibration at a Stenosis A Case Study," *Ultrasound in Med. and Biol.,* vol. 27, no. 8, pp. 1049-1058, Aug. 2001.

[110] Ch. Papageorgiou, C. Kosmatopoulos, and Th. Laopoulos, "A Method for Remote Measurements of Velocity for Vibration Analysis," *Proc. IEEE International Conference on Electronics, Circuits and Systems,* vol. 3, pp. 1491-1494, Feb. 1999.

[111] A. Rowlands, F. A. Duck, and J. L. Cunningham, "Bone Vibration Measurement using Ultrasound: Application to Detection of Hip Prosthesis Loosening," *Medical Engineering and Physics,* vol. 30, no. 3, pp. 278-284, April 2008.

[112] A. Nabavizadeh, M. W. Urban, R. R. Kinnick, and M. Fatemi, "Velocity Measurement by Vibro-Acoustic Doppler," *IEEE Trans. Ultrason., Ferroelect., Freq. Control,* vol. 59, no. 4, pp. 752-765, April 2012.

[113] G. Perrone and A. Vallan, "A Low-Cost Optical Sensor for Noncontact Vibration Measurements," *IEEE Trans. Instrum. Meas.,* vol. 58, no. 5, pp. 1650-1656, May 2009.

[114] A. Vallan, M. L. Casalicchio, and G. Perrone, "Displacement and Acceleration Measurements in Vibration Tests Using a Fiber Optic Sensor," *IEEE Trans. Instrum. Meas.,* vol. 59, no. 5, pp. 1389-1396, May 2010.

[115] J. G. Mueller and T. G. Pratt, "Feasibility Study on a Noncontact Remote-Sensing Vibration Transducer Using RF Polarimetry," *IEEE Trans. Instrum. Meas.,* vol. 62, no. 11, pp. 3073-3086, Nov. 2013.

[116] F. Alonge, M. Branciforte, and F. Motta, “A Novel Method of Distance Measurement Based on Pulse Position Modulation and Synchronization of Chaotic Signals Using Ultrasonic Radar Systems,” *IEEE Trans. Instrum. Meas.,* vol. 58, no. 2, pp. 318-329, Feb. 2009.

[117] X. Li, R. Wu, S. Rasmi, J. Li, L. N. Cattafesta, and M. Sheplak, “Acoustic Proximity Ranging in the Presence of Secondary Echoes,” *IEEE Trans. Instrum. Meas.,* vol. 52, no. 5, pp. 1593-1605, Oct. 2003.

[118] S. G. Kambalimath, P. C. Pandey, P. N. Kulkarni, and S. S. Mahant-Shetti, “FPGA-Based Implementation of Comb Filters Using Sequential Multiply-Accumulate Operations for Use in Binaural Hearing Aids,” *Proc. IEEE India Conference,* pp. 1-6, Dec. 2014.

[119] J. Kranjec, S. Begus, J. Drnovsek, and G. Gersak, “Novel Methods for Noncontact Heart Rate Measurement: A Feasibility Study,” *IEEE Trans. Instrum. Meas.,* vol. 63, no. 4, pp. 838-847, Apr. 2014.

[120] P. Liu, X. Diao, J. Li, K. Zhan, X. He, and Z. Qin, “Orthogonal Frequency Ultrasound Vibration Pulses for SDUV,” *Proc. IEEE International Conference on Signal Processing, Communication and Computing,* pp. 1-4, Aug. 2013.

[121] B. Santhanam, and P. Maragos, “Multicomponent AM-FM Demodulation via Periodicity-Based Algebraic Separation and Energy-Based Demodulation,” *IEEE Trans. Commun.,* vol. 48, no. 3, pp. 473-489, Mar. 2000.

[122] A. Potamianos and P. Maragos, “A Comparison of the Energy Operator and Hilbert Transform Approaches for Signal and Speech Demodulation,” *Signal process.,* vol. 37, no. 1, pp. 95-120, May 1994.

[123] P. Maragos, J. F. Kaiser, and T. F. Quatieri, “On Amplitude and Frequency Demodulation using Energy Operators,” *IEEE Trans. Signal Process.,* vol. 41, no. 4, pp. 1532-1550, April 1993.

[124] P. Maragos, and A. Potamianos, “Higher Order Differential Energy Operators,” *IEEE Signal Process. Lett.,* vol. 2, no. 8, pp. 152-154, Aug. 1995.

[125] B. Santhanam, and P. Maragos, "Energy Demodulation of Two-component AM-FM signal Mixtures," *IEEE Signal Process. Lett.,* vol. 3, no. 11, pp. 294-298, Nov. 1996.

[126] B. Santhanam, "Generalized Energy Demodulation for Large Frequency Deviations and Wideband Signals," *IEEE Signal Process. Lett.,* vol. 11, no. 3, pp. 341-344, Mar. 2004.

[127] A. C. Bovik, P. Maragos, and T. F. Quatieri, "AM-FM Energy Detection and Separation in Noise using Multiband Energy Operators," *IEEE Trans. Signal Process.,* vol. 41, no. 12, pp. 3245-3265, Dec. 1993.

[128] Alan C. Bovik, Joseph P. Havlicek, Mita D. Desai, David S. Harding, "Limits on Discrete Modulated Signals," *IEEE Trans. Signal Process.,* vol. 45, no. 4, pp. 867-879, April 1997.

[129] B. Friedlander, and J. M. Francos, "Estimation of Amplitude and Phase Parameters of Multicomponent Signals," *IEEE Trans. Signal Process.,* vol. 43, no. 4, pp. 917-926, April 1995.

[130] D. Wei, and A. C. Bovik, "On the Instantaneous Frequencies of Multi-Component AM-FM Signals," *IEEE Trans. Signal Process. Lett.,* vol. 5, no. 4, pp. 84-86, April 1998.

[131] F. Gianfelici, G. Biagetti, P. Crippa, and C. Turchetti, "Multicomponent AM-FM Representations: An Asymptotically Exact Approach," *IEEE Trans. Audio, Speech, and Language Process.,* vol. 15, no. 3, pp. 823-837, Mar. 2007.

[132] X. Hu, S. Peng, and W. L. Hwang, "EMD Revisited: A New Understanding of the Envelope and Resolving the Mode-Mixing Problem in AM-FM Signals," *IEEE Trans. Signal Process.,* vol. 60, no. 3, pp. 1075-1086, Dec. 2012.

[133] P. Flandrin, G. Rilling, and P. Goncalves, "Emprical Mode Decomposition as a Filter bank," *IEEE Signal Process. Lett.,* vol. 11, no. 2, pp. 112-114, Feb. 2004.

[134] G. Rilling, P. Goncalves, and J. M. Lilly, "Bivariate Empirical Mode Decomposition," *IEEE Signal Process. Lett.,* vol. 14, no. 12, pp. 936-939, Dec. 2007.

[135] A. B. Grebene, “An Integrated Frequency-Selective AM/FM Demodulator,” *IEEE Trans. Broadcast. Telev. Receiv.,* vol. 17, no. 2, pp. 71-80, May 1971.

[136] R. M. Bernstein, and A. G. Vacroux, “Frequency Response of Phase Locked Loops,” *IEEE Trans. on Broadcast. Telev. Receiv.,* vol. 17, no. 4, pp. 239-244, Nov. 1971.

[137] P. W. Osborne, and D. L. Schilling, “Threshold Analysis of Phase-Locked-Loop Demodulators using Most Likely Noise,” *IEEE Trans. Commun. Technol.,* vol. 19, no. 1, pp. 31-41, Feb. 1971.

[138] F. A. Cassara, H. Schachter, and G. H. Simowitz, “Acquisition Behavior of the Cross-Coupled Phase-Locked Loop FM Demodulator,” *IEEE Trans. Commun.,* vol. 28, no.6, pp. 897-904, Jun.1980.

[139] H. J. Blinchikoff and G. R. Vaughan, “All-Pole Phase-Locked Tracking Filters,” *IEEE Trans. Commun.,* vol. 30, no.10, pp. 2312-2318, Oct. 1982.

[140] P. Hasan, “PLL FM Demodulator Performance Under Gaussian Modulation,” *IEEE Trans. Commun.,* vol. 46, no. 4, pp. 437-440, April 1998.

[141] R. Lyons and Amy Bell, “The Swiss Army Knife of Digital Networks,” *IEEE Signal Process. Mag.,* vol. 21, no.3, pp. 90-100, May 2004.

[142] C. S. Turner, “Recursive Discrete-Time Sinusoidal Oscillators,” *IEEE Signal Process. Mag.,* vol. 20, no. 3, pp. 103 -111, May 2003.

[143] P. Sumathi, P. A. Janakiraman, “Phase Locking Scheme based on Look-up-Table-Assisted Sliding Discrete Fourier Transform for Low-Frequency Power and Acoustic Signals,” *IET Circuits Devices and Systems,* vol. 5, no. 6, pp. 494-504, Nov. 2011.

[144] M. Abramowitz and I. A. Stegun, “Handbook of Mathematical Functions with Formulas, Graphs, and Mathematical Tables,” *Dover,* 1964.

[145] G. Fedele and A. Ferrise, “A Frequency-Locked-Loop Filter for Biased Multi-Sinusoidal Estimation,” *IEEE Trans. Signal Process.,* vol. 62, no. 5, pp. 1125-1134, Mar. 2014.

[146] P. Sumathi, “A Frequency Demodulation Technique Based on Sliding DFT Phase Locking Scheme for Large Variation FM Signals,” *IEEE Commun. Lett.,* vol. 16, no. 11, pp. 1864-1867, Nov. 2012.

[147] J. Hazarika and P. Sumathi, “Moving Window Filter Based Frequency-Locked Loop for Capacitance Measurement,” *IEEE Trans. Industrial Electronics,* vol. 62, no. 12, pp. 7821-7823, Dec. 2015.

[148] A. J. Noga and T. K. Sarkar, “A Discrete-Time Method of Demodulating Large Deviation FM Signals,” *IEEE Trans. Commun.,* vol. 47, no. 8, pp. 1194-1200, Aug. 1999.

[149] G. Divakaran and R. M. Howard, “Reduction in Harmonic Distortion Through Use of Aperiodic Timing in Frequency Demodulation,” *IEEE Commu. Lett.,* vol. 8, no. 9, pp. 549-551, Sep 2004.

[150] J. Epps, E. Ambikairajah and T. Thiruvaran, “Robust FM demodulation of discrete-time signals using least squares differential ratio,” *IET Electron. Lett.,* vol. 43, no. 13, pp.727-729, June 2007.

[151] J. A. Rosendo Macias and A. Gomez Exposito, “Efficient Moving-Window DFT Algorithms,” *IEEE Trans. Circuits Syst. II, Analog Digit. Signal Process.,* vol. 45, no. 2, pp. 256-260, Feb. 1998.

[152] D. Kouame, J. M. Girault, J. P. Remenieras, J. P. Chemla, and M. Lethiecq, “High Resolution Processing Techniques for Ultrasound Doppler Velocimetry in the Presence of Colored Noise. Part II: Multiplephase Pipe-Flow Velocity Measurement,” *IEEE Trans. Ultrason., Ferroelect., Freq. Control,* vol. 50, no. 3, pp. 267-278, Mar. 2003.

[153] K. Isoda and T. Hara, “Doppler Velocity Measurement Method with a Second-Time-Around Echoes Suppression for Synthetic Bandwidth Radars,” *European Radar Conference,* pp. 134-137, Oct. 2011.

Publications

1. Ksh. Milan Singh and P. Sumathi, “Moving-Window DFT based Frequency-Locked Loop for FM demodulation,” *IEEE Commun. Lett.* (Accepted).
2. Ksh. Milan Singh and P. Sumathi, “Synchronization Technique for Doppler Signal Extraction in Ultrasonic Vibration Measurement Systems,” *IEEE Trans. Instrum. Meas.,* vol. 64, no. 12, pp. 3162-3172, Dec. 2015.
3. Ksh. Milan Singh and P. Sumathi, “Vibration Parameter Estimation Methods for Ultrasonic Measurement Systems- A Review,” *IET Sci. Meas. Technol.,* vol. 9, no. 4, pp. 492-504, July 2015.
4. P. Sumathi and Ksh. Milan Singh, “Sliding discrete Fourier transform-based mono-component amplitude modulation frequency modulation signal decomposition,” *IET Commun.,* vol. 9, no. 9, pp. 1221-1229, June 2015.